QUANTIFYING PERMAFROST PROCESSES AND SOIL MOISTURE WITH INTERFEROMETRIC PHASE AND CLOSURE PHASE

A DISSERTATION
SUBMITTED TO THE DEPARTMENT OF GEOPHYSICS
AND THE COMMITTEE ON GRADUATE STUDIES
OF STANFORD UNIVERSITY
IN PARTIAL FULFILLMENT OF THE REQUIREMENTS
FOR THE DEGREE OF
DOCTOR OF PHILOSOPHY

Roger John Michaelides
June 2020

I certify that I have read this dissertation and that, in my opinion, it is fully adequate in scope and quality as a dissertation for the degree of Doctor of Philosophy.

(Howard Zebker) Principal Adviser

I certify that I have read this dissertation and that, in my opinion, it is fully adequate in scope and quality as a dissertation for the degree of Doctor of Philosophy.

(Dustin Schroeder)

I certify that I have read this dissertation and that, in my opinion, it is fully adequate in scope and quality as a dissertation for the degree of Doctor of Philosophy.

(Alex Konings)

I certify that I have read this dissertation and that, in my opinion, it is fully adequate in scope and quality as a dissertation for the degree of Doctor of Philosophy.

(Rosemary Knight)

Approved for the Stanford University Committee on Graduate Studies

Abstract

Air temperatures in the Arctic are increasing at twice the global rate, making permafrost regions one of the most vulnerable ecosystems in a changing climate [Jorgenson et al., 2001]. Permafrost, or ground that remains frozen for two or more consecutive years, covers 24% of the Northern Hemisphere and contains 60% of the world's soil carbon [Turetsky et al., 2019a]. Large stores of soil carbon are bound in permafrost, predominantly as carbon dioxide (CO_2) and methane (CH_4); this bound soil carbon is susceptible to rapid decomposition and release into the atmosphere after thaw [Natali et al., 2019]. As air temperatures rise, permafrost regions experience i) seasonal thawing and freezing, and ii) permanent thaw and loss of frozen ground. These processes modify ecosystems, change land cover and surface hydrologic regimes, and release vast amounts of greenhouse gases into the atmosphere. Due to the amount of permafrost soil carbon susceptible to release into the atmosphere, there is a critical need to monitor permafrost status and vulnerability to change, as well as project future behavior of the permafrost system. The vast spatial extent of permafrost regions and their inaccessibility provides challenges to monitoring efforts. In situ methods of characterizing permafrost processes are spatially sparse, restricting regional studies of permafrost thaw status, and introducing uncertainties into climate models.

Remote-sensing techniques are an attractive method for characterizing and monitoring permafrost systems on large scales. Interferometric Synthetic Aperture Radar (InSAR) is a geodetic technique for measuring temporal variations of the surface of the Earth, in which repeated synthetic aperture radar (SAR) images are acquired over a region of interest. These images are then interferometrically combined, and the resulting phase difference between SAR images quantifies surface topography and deformation of the surface of the Earth. InSAR, with its fine spatial resolution and broad coverage, presents an attractive method for regional characterization of permafrost thaw status and active layer thickness at fine resolution. However, in permafrost regions, variations in soil moisture, vegetation, snow cover, and phase changes of pore-bound water and ice all affect the observed deformation and can amplify signal decorrelation. This decorrelation can complicate, and in severe cases preclude, the estimation of surface deformation from InSAR phase observations.

In this dissertation, we use the InSAR technique to observe permafrost processes in the discontinuous permafrost zone, with a case study in the Izaviknek Highlands region of the Yukon-Kuskokwim

delta in Southwestern Alaska. We measure both centimetric seasonal deformation of permafrost associated with seasonal freeze/thaw processes, as well as long-term, interannual deformation associated with permafrost thaw and degradation. We find significant long-term deformation on the order of centimeters per year associated with a complex of wildfire burns in this region, which we relate to the age of wildfire events, and demonstrate that InSAR successfully captures permafrost dynamics induced by wildfire decades after the original burn.

We also introduce a method of quantifying and removing decorrelation phase artifacts from InSAR observations by exploiting closure phase relations within a subset of SAR scenes. We show that decorrelation phase biases on the order of tens of degrees can be successfully characterized and removed from the original InSAR signal. Further, we investigate the impact of variable soil moisture on closure phase observations using a new SAR interferometric imaging model that explicitly accounts for signal decorrelation treating scattering surfaces as realizations of stochastic processes. Finally, we construct an algorithm that combines the SAR interferometric imaging model introduced above with direct closure phase observations to estimate changes in surface soil moisture state directly from InSAR phase measurements.

Acknowledgments

There are many people I would like to thank, without whom this thesis would not have been possible. First and foremost Howard Zebker, my advisor, who has been a source of mentorship throughout my time at Stanford. Through his guidance and his commitment to giving me academic freedom, Howard has taught me how to develop and cultivate my own research interests. He is a role model teacher, advisor, scientist, and engineer.

Dustin Schroeder, my second project advisor, has been a role model professor, educator, researcher, and mentor. He taught by example how to develop a course curriculum, engage a class, and build a research group from the ground up. Most importantly, he taught me how to bridge porous distinctions like engineering and science, or sidelooking vs. nadir radars.

I would like to thank Rosemary Knight for her insights as a member of my thesis committee, and for teaching me that hydrology is not just a surface phenomenon. Alex Konings for serving on my committee, providing me the opportunity to guest lecture, and her invaluable perspective as an early career scientist. George Papanicolaou for kindly agreeing to serve as the outside chair of my thesis committee. Eva Prionas and John Ioannidis for engaging my academic interest in topics that are not geophysical or mathematical in nature.

My research was possible only through the help of current and former members of the Stanford Radar Remote Sensing group: Lin Liu, Ann Chen, Clara Yoon, Yujie Zheng, Stacey Huang, Karissa Pepin, Ettore Biondi, Marko Jakovljevic, Matt Lees, and Emma Velterop. They all provided a great deal of support, encouragement, insight, and friendship throughout my time at Stanford. In particular, Ann Chen took me under her wing when I first joined Howard's group, and has remained a role model and source of invaluable insight to this day. My other friends in the Geophysics department, Jackson MacFarlane, Alex Kendrick, Cansu Culha, Ian Gottschalk, Brent Lunghino, Leighton Watson, and many more, helped keep me sane with their friendship, and many hikes, camping trips, and concerts.

Alex Hayes, for teaching me what it means to be a scientific researcher through his passion for undergraduate research. Marco Mastrogiuseppe, Matt Pritchard, Rowena Lohman, and David Hysell for first stoking my interest in the subtleties of geophysical radar remote sensing. Rick Allmendinger, Mike Malaska, and Tom Farr for introducing me to the joy of field work. Kevin Schaefer,

Andy Parsekian, Sue Natali, Taylor Sullivan, Sarah Ludwig, Sean Schaefer, Richard Chen, and everyone else I have had the joy to work with in the Arctic as part of the Arctic-Boreal Vulnerability Experiment (ABoVE).

I thank all those who helped edit this thesis – in particular Howard, my mom, Andrew Miller, and Nelson Conover. My childhood friends Alex Garabedian, Sam Littlefield, and Simon Jensen for their friendship and gumption, and Ian Kinsella for many valuable chats about grad school while we were home for the holidays.

Most importantly, my family, who have been a constant and unconditional source of support my entire life. I have the two best parents in the world; my loving mom Barbara, who has always been my #1 cheerleader and encouraged me in everything that I do, and my baba Michael, who first sparked my love of science and has been a role model scientist ever since. All of our family pets – Myrtle, Roscoe, Felix, Margaux, and Wolfie, to name a few. Most importantly, my twin sister Maddy, who has been my partner in crime in life from the start.

My loving and kindhearted yiayia Rena and my pappou and namesake Roger Sr., the original radar engineer of the family (working on over-the-horizon radar during the Cold War is much cooler than what I do). My aunt Louiza and godfather Lakis, and my cousins Irena, Natalie, and Areti, for all of the happy holidays we have spent together. My entire family in Cyprus which is much too large to include every name here. My extended family and friends in America, Cyprus, Greece, the UK, Italy, and Lebanon.

The work in this thesis was funded by an NSF Graduate Research Fellowship and the NASA Arctic-Boreal Vulnerability Experiment (ABoVE).

Σας ευχαριστώ όλους με όλη μου την καρδιά

Contents

List of Tables

List of Figures

Chapter 1

Introduction

1.1 Problem Definition

Permafrost, which is ground that remains frozen for two or more consecutive years, covers $\sim 24\%$ of the landmass in the Northern Hemisphere. Despite amounting to only 15% of the global land surface, permafrost soils contain $\sim 60\%$ of the world's soil carbon, with the majority of this carbon within the first few meters of soil [Turetsky et al., 2019a]. Air temperatures in the Arctic are increasing at twice the global rate; permafrost regions are thus both one of the fastest changing global ecosystems, and one of the most affected by climate change [Jorgenson et al., 2001]. Furthermore, the vast stores of bound soil carbon in permafrost soils, predominantly in the form of carbon dioxide (CO_2) and methane (CH_4), are susceptible to rapid decomposition and release into the atmosphere as permafrost soils thaw [Natali et al., 2019]. Permafrost regions have been referred to as the 'sleeping giant' of the global climate and carbon systems by virtue of being one of the most at-risk regions to changing climate, and having the potential to initiate a positive feedback loop in the global carbon cycle [Turetsky et al., 2019b]. Despite their disproportionate sensitivity to warming temperatures and their potential to accelerate climate change, the need for fine spatial resolution coupled with the vast, inaccessible nature of most permafrost regions has caused them to be poorly monitored in comparison to other fast-changing regions in the cryosphere (such as the Antarctic and Greenland ice sheets). It is therefore important to monitor permafrost systems, characterize permafrost status, processes, and vulnerability to change, and understand future behavior and state. Increasingly, remote-sensing techniques are being successfully applied to study permafrost systems.

A key descriptor of permafrost soils is the thickness of the active layer – the region of the soil that seasonally freezes and thaws. Active Layer thickness (ALT) varies considerably across permafrost regions. InSAR's fine spatial and temporal resolutions and sensitivity to cm-scale deformation signals makes it an attractive technique for characterizing permafrost dynamics both locally and over broad regions of interest. For example, Liu et al. [2012] and Schaefer et al. [2015] have successfully used

InSAR to measure ground deformation due to seasonal freeze/thaw cycles in continuous permafrost regions. Despite these successes, InSAR applications to date have been restricted to the continuous permafrost zone. In this thesis, we extend the work first presented in [Liu et al., 2012] and use InSAR to characterize and measure seasonal and interannual permafrost physical processes in the Yukon-Kuskokwim river delta, within the discontinuous permafrost zone of Southwest Alaska. We observe seasonal deformations on the order of $1-5$ centimeters, corresponding to active layer thicknesses ranging from $20-100$ centimeters. Additionally, we present a novel estimate of the time-dependent behavior of permafrost that has been previously affected by wildfire. We observe recovery rates on the order of several millimeters a year of wildfire-affected permafrost soils, and estimate a recovery time of ~ 65 years required to return to pre-fire thermal equilibrium for both the seasonally freezing and thawing active layer, as well as the permafrost column as a whole.

Estimating ALT requires assumptions or independent measurements of soil porosity, water saturation fraction, and organic layer properties, all of which are variable across permafrost regions and vary with surface geomorphology. These parameters dictate the amount of deformation that a specific region of permafrost will experience due to the change in density of water associated with freezing and thawing, and therefore must accurately reflect a region if a plausible value of ALT is desired. Lack of knowledge of surface soil moisture and soil column saturation can be dominant sources of error during estimation of ALT, complicating ALT retrieval in areas where soil moisture properties are heterogeneous or not known. Microwave radar remote sensing is highly sensitive to variations in dielectric permittivity (which is in turn related to water content and freeze/thaw state), as well as physical surface scattering properties, such as vegetation type and extent, surface roughness, surface water saturation, and snow cover. Consequently, the fidelity of InSAR measurements over permafrost regions, as well as InSAR-derived estimates of ALT, is highly dependent upon the soil moisture state of the surface, as well as the temporal stability of surface scattering phenomena (i.e. the correlation of the surface) [Liu et al., 2012; Schaefer et al., 2015].

It is thus important to characterize the extent to which the effects of soil moisture state and the phase component of surface decorrelation can be estimated directly from InSAR observations without independent observations or ancillary data. We develop and present an algorithm that utilizes multiple observations of interferometric phase triplets to estimate the decorrelation phase component of the measured interferometric phase. This decorrelation phase term can then be removed to increase the accuracy of the deformation estimate, and potentially be exploited to estimate surface soil moisture state. After introducing this algorithm and providing a demonstration of its use, we develop an interferometric SAR imaging model that explicitly incorporates the statistics of signal decorrelation due to variable soil moisture state and stochastically rough scattering surfaces. Using this model, we investigate the sensitivity of closure phase measurements to changes in soil moisture state, and comment on the implications for both conventional InSAR applications in decorrelating regions, as well as the potential for soil moisture estimation from InSAR measurements. Finally, we

demonstrate a simple retrieval algorithm of soil moisture state from closure phase and decorrelation phase observations, and comment on its implications for future monitoring efforts of permafrost regions, as well as other regions subject to significant surface decorrelation.

1.2 Contributions

The contributions of this thesis are two-fold. The first focus of this thesis is to develop new methods and identify applications for InSAR-based characterization of permafrost processes. Analysis of InSAR data over discontinuous permafrost regions makes apparent that the largest sources of error in ALT estimation from measured surface deformation were associated with uncertainties in soil moisture. To that end, the second major focus of this thesis is to identify methods of reducing this uncertainty. By exploiting multiple, overlapping combinations of InSAR closure phase triplets – which are sensitive to soil moisture state and other sources of signal decorrelation – we develop an algorithm to estimate and remove the component of interferometric phase associated with signal decorrelation. Directly relating decorrelation phase and closure phase measurements to soil moisture requires an interferometric SAR model that explicitly incorporates soil moisture. We develop a modified version of the interferometric model described in De Zan et al. [2014] that explicitly incorporates the statistics of stochastic scattering surfaces. Finally, we explore the potential of directly estimating soil moisture from decorrelation phase and closure phase observations.

The main contributions of this thesis are summarized below:

1. We present an InSAR-based method of estimating active layer thickness and apply it over a region of discontinuous permafrost in the Yukon-Kuskokwim delta in Southwest Alaska. We quantify active layer thickness and compare InSAR-derived estimates of active layer thickness to independent in-situ field measurements.

2. We demonstrate that long-term trends in permafrost seasonal deformation are related to time since burn in wildfire burns scars in the YK delta. Using a 'space for time' analysis, we estimate the long-term recovery behavior of wildfire-affected permafrost. We observe permafrost degradation and active layer recovery rates on the order of a centimeter per year, corresponding to a recovery time of ~ 65 years to return to a pre-fire thermal equilibrium state.

3. We derive the relationship between decorrelation phase and closure phase, and propose an algorithm for estimating decorrelation phase from a redundant network of closure phase observations. We apply this algorithm to a set of ALOS data, measuring decorrelation phases as large as 45°, corresponding to errors in stacked InSAR deformation rates on the order of millimeters per year. In many applications, these errors are comparable to observed uncertainties. By separating this error

component from the signal of interest, it can be successfully removed. Further, if this error term is associated with a systematic process, such as changing soil moisture, these error estimates can be further studied as a secondary signal of interest.

4. We develop a A SAR interferometric model that explicitly considers both variable soil moisture and the statistics of stochastically rough and time-varying surfaces. We compare several interferometric models and scattering distributions for soil moisture estimation from closure phase and decorrelation phase. We demonstrate that the model developed in this thesis yields more physically realistic changes in soil moisture than previously published interferometric models.

1.3 Thesis Roadmap

The following chapters in this dissertation are briefly summarized below:

Chapter 2 provides a brief scientific background on permafrost regions and processes, and contextualizes their importance within both regional and global climate models and studies. A brief discussion of soil moisture, its importance as a hydrological and climatological variable, and methods of its estimation via remote sensing techniques is also provided.

Chapter 3 provides a brief overview of radar imaging, Synthetic aperture radar (SAR), and InSAR, as well as the most salient features of InSAR time series analysis pertinent to this dissertation. We define signal decorrelation, from which closure phase (and the physical reasons for phase nonclosure) are also defined. Finally, we briefly discuss previous applications of InSAR to study permafrost processes, and give a brief overview.

Chapter 4 is a case study in the Izaviknek Highlands of the Yukon-Kuskokwim (YK) Delta in Southwestern Alaska. A region of subarctic discontinuous permafrost, the YK delta is characterized by a variety of permafrost processes and thaw regimes. Further, it has experienced a series of large wildfires since 1972, making it a natural laboratory to study the interaction between tundra wildfire and permafrost thaw processes [Michaelides et al., 2019a]. We introduce a modification to the conventional SBAS method of InSAR time series analysis, and then apply this to an ALOS-PALSAR dataset to estimate the seasonal subsidence and active layer thickness over a region of the Izaviknek Highlands. In addition, we quantify the interannual effects of wildfire on permafrost, and the long-term recovery behavior of permafrost to wildfire. We compare remote sensing results with in-situ ground-penetrating radar (GPR) and mechanical probing measurements. Finally, the implications of this regional study for the arctic domain as a whole are briefly discussed.

In Chapter 5, we introduce an algorithm for estimating decorrelation phase from a network of closure phase observations. This algorithm is motivated by a brief discussion of closure phase and decorrelation phase, and the mathematical relationship between the two is derived. The algorithm is described in detail, applied to a case study, and the results are interpreted.

We continue to address closure phase in Chapter 6, where we develop an interferometric SAR imaging model which explicitly incorporates both the statistics of stochastically rough surfaces, and volume scattering. This imaging model is shown to be consistent with the relationships between signal decorrelation and closure phase introduced in Chapter 5. The impact of variable soil moisture on this model, and in turn closure phase, is then discussed, and the potential for estimating soil moisture from closure phase measurements is proposed. We then synthesize Chapters 5 and 6 by proposing a simple algorithm for estimating variations in surface soil moisture. A series of InSAR data over Kilauea is processed, and decorrelation phase is estimated from closure phase observations using the algorithm introduced in Chapter 5. A simple inversion method for estimating soil moisture from decorrelation phase using the imaging model proposed in Chapter 6 is introduced, and then applied on the decorrelation phase estimates. The results are analyzed, and decorrelation due to both variable soil moisture, and other time-dependent surface scattering properties, are discussed within the context of conventional geodetic techniques.

Finally, we provide concluding remarks in Chapter 7, and briefly discuss potential areas of future work.

Chapter 2

Scientific Background

This chapter provides a brief scientific background to the major contributions of this thesis. We first define permafrost, contextualize its role within the context of a warming arctic, and briefly review several techniques for quantifying permafrost physical processes and properties. As will be discussed, soil moisture is a critical environmental parameter that can both influence permafrost processes and complicate permafrost monitoring via radar remote sensing techniques. We provide a brief overview of soil moisture, discuss its importance in the global water cycle and permafrost regions, and mention several conventional radiometric methods of soil moisture estimation.

2.1 Permafrost

Permafrost is ground that remains at or below 0°C for two or more consecutive years. Permafrost was first defined in the English language in 1943 by Stanford University professor of Geology S.W. Muller while advising the U.S. Army Corps of Engineers on the construction of the Alaskan Highway during World War II ([Muller, 1943]; for a general overview of permafrost and periglacial environments, see [French, 2007]). Occurring over 24% of the northern hemisphere, permafrost regions are characterized by frozen ground and the seasonal freezing and thawing of the uppermost soil column [Jorgenson et al., 2001]. The spatial distribution of permafrost is predominantly controlled by climate, and to a lesser degree site-specific thermal conductivity of the soil, vegetation and snow cover, topography, surface and near-surface hydrology, and wildfire activity [French, 2007]. As climate and temperature are the leading controls on permafrost distribution, there is a pronounced latitudinal dependence on permafrost distribution. Continuous permafrost (underlying 90-100% of the landscape) is ubiquitous throughout the Arctic Circle. With decreasing latitude, continuous permafrost transitions into discontinuous permafrost (50-90% of the landscape), and finally sporadic permafrost (0-50% of the landscape, see 2.1).

During the spring thaw period, rising surface temperatures cause pore space water to gradually

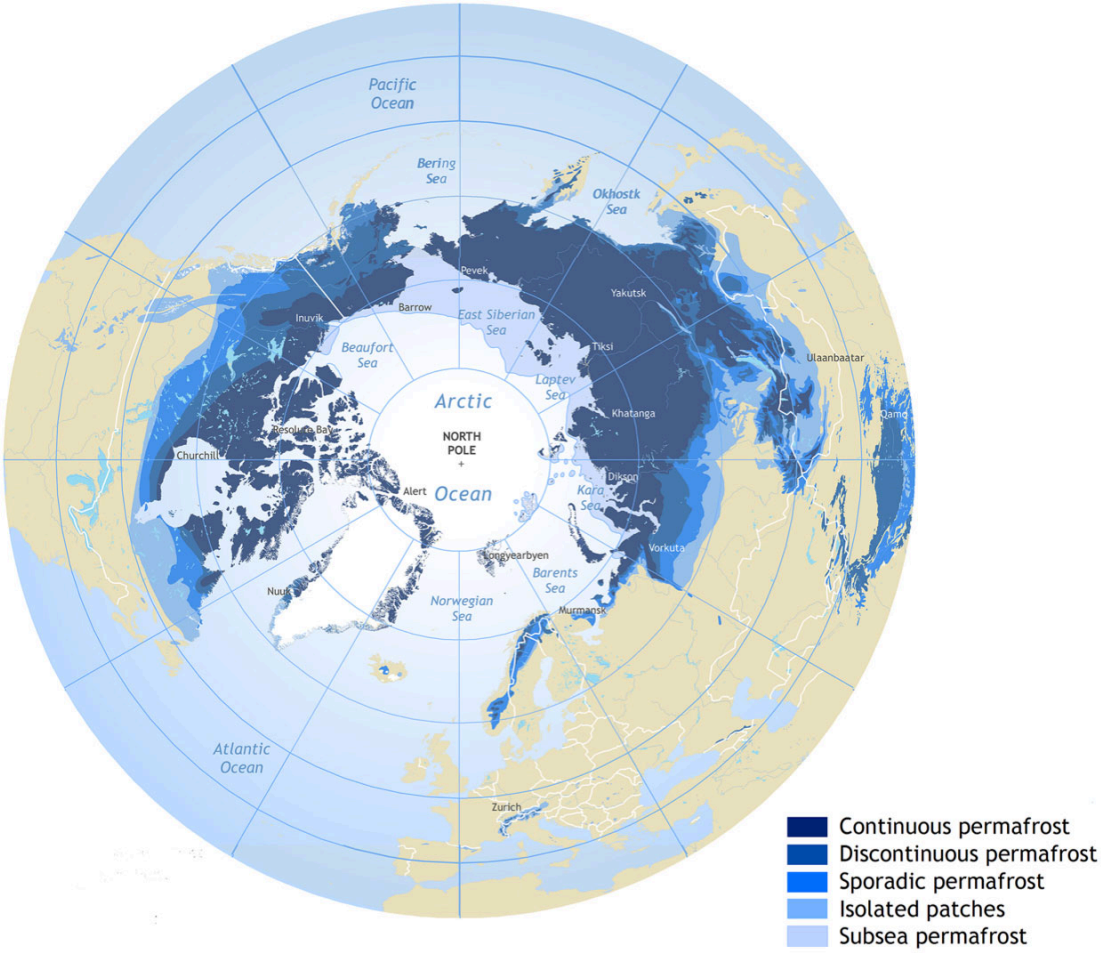

Figure 2.1: Spatial distribution of permafrost extent in the Northern Hemisphere. (credit: Brown et al. [1997]; International Permafrost Association).

thaw from solid to liquid. Due to the ∼9% decrease in volume that pore water occupies between its frozen and unfrozen state, this phase change of water causes the ground to subside due to the effective decrease in pore water volume in a column of soil during thaw [Liu et al., 2012]. As the spring season progresses through summer, extended periods of above-zero surface temperature cause more and more of the subsurface pore water to thaw, thereby causing a greater amount of subsidence. Eventually, a given region of permafrost will experience its maximum thaw during the thaw season; this maximum thaw depth is the active layer thickness (ALT). In autumn and winter, this liquid water freezes again, and the ground experiences uplift as the effective volume of the pore space in a soil column increases. Thus, over a seasonal cycle, permafrost environments experience freeze/thaw-associated cycles of subsidence and uplift. Variability of soil physical properties (porosity, water saturation fraction, organic layer content) and surface physical properties (thermal insulation, snow cover, vegetation cover, surface water cover, hillslope, shading, topography) all affect the seasonal freezing and thawing of pore water, as well as any long-term changes in water content, excess ground ice, soil compaction and subsidence, and surface cover [French, 2007; Jorgenson et al., 2001].

Figure 2.2: Cross-section depicting a massive ice wedge embedded within a typical stratigraphic section of a mineral layer divided into ice-rich permafrost and ice-poor permafrost, and an active layer characterized by high organic matter content (credit: Wayne Pollard).

Permafrost seasonal thaw and secular degradation – particularly of ice-rich permafrost – can have significant impacts on surface hydrology. Because the pore space is occupied by frozen water, permafrost acts as an effective aquiclude, modifying surface drainage patterns and impeding hydrological connectivity between surface water and subsurface aquifers. Lowlands and areas of increased relative subsidence can experience surface water impoundment, while uplands and areas experiencing relatively little subsidence (due perhaps to ecologically-driven thermal insulation) can experience enhanced drainage [Woo, 1990]. Changes in surface hydrology can, in turn, further induce changes in permafrost susceptibility to thaw, rates of degradation and accumulation of soil carbon [Schuur et al., 2008], ecological regimes and wildfire susceptibility [Jorgenson and Osterkamp, 2005], and emission rates of greenhouse gases such as carbon dioxide and methane [Turetsky et al., 2007]. The complex interaction of these ecological and physical processes is further complicated by the spatially heterogeneous warming that the arctic and subarctic regions are undergoing [Shepherd, 2016; Callaghan et al., 2010]. Permafrost regions can consequently be divided into a variety of zonal categories, such as climate-driven, ecosystem-driven, and ecosystem-protected permafrost regions [Jorgenson et al., 2010].

Air temperatures in high-latitude permafrost regions are increasing at twice the global rate, which threatens the distribution and stability of permafrost regions worldwide [Jorgenson et al., 2001; Osterkamp et al., 2009]. Large-scale thawing of permafrost can impact both local ecosystems and hydrology, as well as the global climate system through the release of bound carbon dioxide and methane, both of which can become volatile after the frozen ground it is contained within thaws [Schuur et al., 2008; Turetsky et al., 2007]. Despite covering less than 9% of the world's land surface, permafrost soils contain between 25-50% of the world's soil organic carbon content, making permafrost regions simultaneously one of the largest, and most vulnerable, sources of carbon in the global carbon cycle [Bockheim and Hinke, 2007]. There is necessarily great interest in characterizing and monitoring permafrost status across the arctic and subarctic regions.

ALT is designated by the World Meteorological Organization (WMO) as an essential climate variable for monitoring the status of permafrost. The standard way to measure ALT is to use a metal probe or buried temperature sensors, resulting in an extremely sparse global in situ network, with large, in some cases regional, spatial gaps. The current sparsity of global permafrost monitoring activities – as well as the poorly understood interactions between climate, permafrost degradation, surface hydrology, and CO2/methane release – generates uncertainty concerning the role and importance of permafrost in the global climate system, carbon cycle, and water cycle, necessitating a more complete understanding. A reliable remote sensing technique to measure ALT should allow for effective global characterization and monitoring of permafrost status, which in turn could lead to a more complete understanding of the interactions between the global climate system and permafrost in the Arctic. Statistical regressions of in-situ field data with Hyperspectral NDVI, optical imagery, and SAR imagery have been previously employed via upscaling techniques to generate extrapolated

Figure 2.3: Depiction of different permafrost regimes. The transition from continuous through discontinuous to sporadic permafrost occurs spatially, but can also occur temporally as permafrost regimes evolve gradually through a warming climate (credit: National Geographic).

maps of ALT [Gangodagamage et al., 2014; Widhalm et al., 2017]. Geophysical remote-sensing techniques such as airborne electromagnetic imaging (AEM) and P-band airborne radar (AIRMOSS) have been employed to map permafrost distribution at depth, near-surface moisture saturation, and thermal state [Minsley et al., 2012; Tabatabaeenejad et al., 2015]. Finally, InSAR has been used to directly measure surface deformation associated with permafrost freeze-thaw cycles and thermokarst processes, from which ALT, as well as long-term variations in ALT, can be derived [Liu et al., 2012; Schaefer et al., 2015].

2.2 Soil Moisture

Soil moisture is a critically important climatic, hydrological, and ecological variable [*Decadal Survey*, 2018]. Water stored in the soil and vegetation canopies accounts for less than 1% of the global water volume [Bras, 1990]. Nonetheless, this small volume of water plays a disproportionate role in the global water cycle, influencing groundwater recharge rates [*National Research Council*, 2004], determining transpiration and evaporation rates of bare soil, and influencing the partitioning of radiative heat fluxes between the atmosphere and ground surface [Brutsaert, 1982; Konings, 2015]. Soil moisture state can influence, and in turn is influenced by, local atmospheric weather patterns and precipitation rates [Brutsaert, 1982; McColl et al., 2017; McColl et al., 2019]. The long memory of soil moisture state can induce seasonal and interannual fluctuations on surface water, evapotranspiration and plant health, precipitation, and radiative transfer [Konings, 2015; Konings et al., 2016; McColl et al., 2017]. In permafrost environments, soil moisture state can play a dominant role in soil thermal state, influencing permafrost thaw rates, methane and carbon dioxide emission rates, and initiating land cover changes [Natali et al., 2015; Lawrence et al., 2015; Walvoord and Kurylyk, 2016].

Despite the importance of soil moisture and vegetation canopy water in an array of physical processes, it remains difficult to obtain accurate, routine, and cost-effective estimates of soil moisture over significant spatial scales and at necessary spatial resolution. This difficulty hinders the widespread use of soil moisture products in hydrological, biogeochemical, and ecosystem modeling efforts [Van Zyl and Kim, 2011]. Significant advances have been made to retrieve soil moisture products using both passive and active radar remote sensing instruments [Ochsner et al., 2013]. The majority of soil moisture retrievals rely on passive radiometric measurements, which depend directly on the conductivity of the soil. However, passive radiometry suffers from a coarse spatial resolution in comparison to active radar imaging techniques such as InSAR. The development of robust soil moisture retrieval algorithms using active synthetic aperture radar (SAR) data is motivated in large part by the coarse spatial resolution of passive radiometric observations and the high degree of lateral spatial variability of soil moisture [Famiglietti et al., 2008]. NASA's Soil Moisture Active Passive (SMAP) mission was a major effort in this direction, combining passive radiometry and an active radar system to interpolate within the larger radiometer's resolution cell to a finer

resolution [Entekhabi et al., 2010]. Unfortunately, a failure in the active radar system limited the resolution of the SMAP mission to the basic passive radiometric footprint.

Soil moisture retrievals from active radar measurements commonly rely upon the dependence of the backscatter coefficient σ^0 upon the dielectric permittivity (and thus soil moisture) of the soil. However, backscatter is also dependent upon surface roughness, the correlation length of the surface, vegetation, and the viewing geometry of the satellite, complicating the separation of these various components from a single backscatter observation [Van Zyl and Kim, 2011]. Soil moisture measurement from single frequency single polarimetric observations have historically relied upon simple empirical relationships [Dobson and Ulaby, 1986; Schneider and Oppelt, 1998]. The use of dual and quadruple polarimetric SAR datasets allows for the separation of surface roughness and soil moisture contributions to SAR backscatter [Dubois et al., 1995; Shi et al., 1997; Oh et al., 1992]. Similarly, the use of overlapping, contemporaneous multifrequency, SAR datasets has shown promise in isolating the soil moisture component of the SAR backscatter [Entekhabi et al., 1994; Bindlish and Barros, 2000].

It is well documented that soil moisture impacts the amplitude of active radar data, and while its impact on phase measurements has been noted [Nolan and Fatland, 2003; Nolan et al., 2003; Barrett et al., 2013], few studies have addressed developing soil moisture retrieval algorithms exploiting phase measurements. Most previous phase-based studies were either laboratory measurements under controlled conditions, or observations of InSAR phase fluctuations that coincided with terrains known or suspected to be of time-variable soil moisture. Still lacking is a complete imaging model that relates soil moisture to SAR amplitude and phase; such a model could allow for widespread retrieval of soil moisture from InSAR measurements.

In 2014 De Zan et al. formulated an interferometric model that explicitly accounts for variations in surface dielectric permittivity associated with changes in soil moisture (see Figure 2.4). This model provided a physically rigorous model that reproduced many of the observations from previous investigations of soil moisture and interferometric phase. Interestingly, this model further predicts nonzero phase closure when soil moisture variations are considered [De Zan et al., 2014; Zwieback et al., 2015b; De Zan and Gomba, 2018].

Conventionally, phase and amplitude information have often been considered separately (and singularly) in most SAR-based environmental parameter retrievals. Phase closure has only been experimentally observed in recent years; a complete statistical and physical understanding of its nature is lacking, and its potential for novel soil moisture and vegetation retrieval algorithms has not been fully explored.

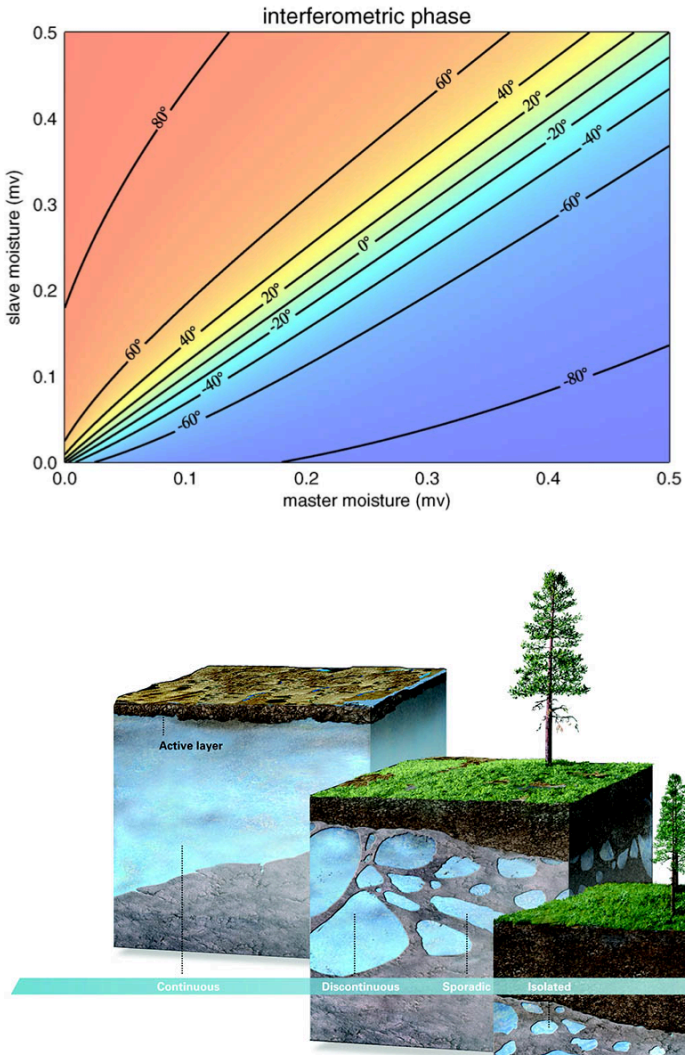

Figure 2.4: Top: Interferometric phase as a function of soil moisture according to the De Zan model. Bottom: Real (solid line) and imaginary (dotted line) components of the dielectric permittivity of soil as a function of the soil moisture state, according to the Hallikainen mixing model (adapted from De Zan et al. [2014]).

Chapter 3

InSAR Background

3.1 Radar

Radar, which is an acronym for 'radio detection and ranging', is a remote sensing technique reliant on the transmission, reflection, and detection of radio frequency (RF) electromagnetic energy. Canonically, a radar measures the two-way travel time of a transmitted pulse between the radar antenna and the reflecting target of interest. Since the launch of SEASAT in 1978, a variety of radar instruments have been employed on satellite missions for imaging and remote sensing of the Earth and other planetary bodies. Because radar is an active-source technique, radar imaging does not require daytime operating conditions like conventional optical sensors. Furthermore, because the atmosphere exhibits little attenuation at RF frequencies, radar imaging can penetrate cloud cover, precipitation, and other atmospheric phenomena which can severely impact other remote sensing methods.

3.2 Radar Imaging

Most satellite imaging radars are coherent and operate with a pulsed transmission architecture, with center frequencies typically in the range of MHz (10^6) to THz (10^{12}), yielding a sensitivity to scatterers on the order of centimeters to meters. Figure 3.1 illustrates the viewing geometry of a typical spaceborne radar imager. The radar is mounted on an orbiting satellite with an altitude h and an along-track (or azimuthal) velocity v. A sidelooking radar antenna emits a sequence of pulses which propagate along the line of sight (LOS) direction, ultimately illuminating a region of the Earth's surface referred to as the swath or radar footprint. The radar antenna receives reflections (echoes) from scatterers illuminated within the radar swath. The arrival time of each echo depends upon the position of the scatterer within the footprint in the along-track (azimuth) direction and the across-track (range) direction. The arrival time is therefore proportional to the total distance

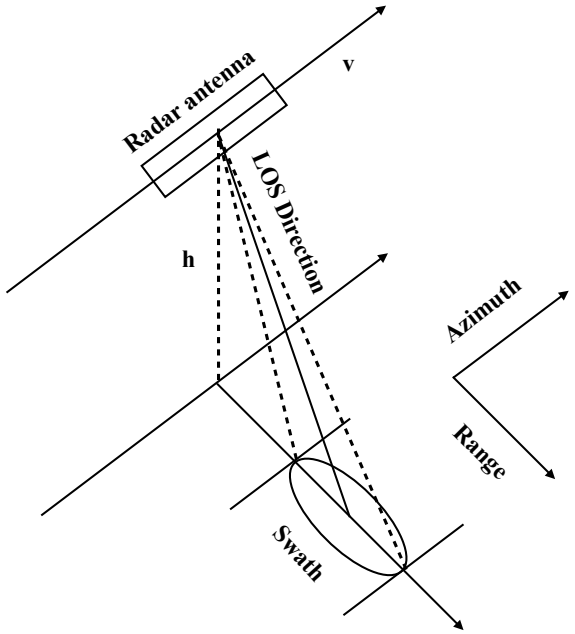

Figure 3.1: Geometry of a typical spaceborne radar imaging system. The radar instrument (represented by the antenna) is mounted on a satellite with an altitude h orbiting the Earth with a velocity v. The line of sight (LOS) direction is defined as the vector between the radar antenna and the illuminated ground swath. The azimuth direction is defined parallel to the along-track direction of the satellite motion, while the range direction is defined to be perpendicular to the azimuth direction.

from the scatterer to the radar antenna.

The received power P_r of a sidelooking radar imager can be expressed, using the radar equation, as:

$$P_r = \frac{P_t G_t A_r A_{scat} \sigma}{(4\pi R^2)^2} \tag{3.1}$$

where P_t is the transmitted power, G_t is the antenna gain, A_r is the area of the antenna, A_{scat} is the effective scattering area of the reflecting target, σ is the normalized radar cross-section of the target, and R is the range from the transmitting antenna to the target. For the remainder of this thesis we shall implicitly assume a monostatic imaging geometry, whereby the same physical antenna is used for both transmission and reception.

The total received signal is a summation of all of the reflected transmitted echoes from individual scatterers within the illuminated ground swath, each time-delayed accordingly. The particular scattering properties of each scatterer – such as physical size, shape, material composition, and surface roughness – can in turn modulate the amplitude and phase of its associated reflection. Signal

processing methods are used to discriminate between different scatterers and form radar images.

The two most common figures of merit used to characterize radars and their associated images are the signal-to-noise ratio (SNR) and resolution of the radar. Beyond merely increasing the peak power transmitted by a radar, the SNR can also be increased by lengthening the pulse length of the radar. The range resolution of the radar, however, is linearly proportional to the pulse length. This fundamental, and seemingly unavoidable trade-off between SNR and resolution, can be remedied by optimally discriminating between the radar echo and the background noise source. This process, called matched filtering, correlates the received signal with the transmitted signal, and compresses the radar energy into an effectively shorter pulse. In this way, a fine range resolution can be achieved alongside a high SNR. After matched filtering, the range resolution δ_r of the radar is:

$$\delta_r = \frac{c\tau}{2} = \frac{c}{2BW} \tag{3.2}$$

where c is the speed of light, τ is the transmitted pulse length, and BW is the bandwidth of the transmitted signal. A finite signal bandwidth is achieved through pulse modulation, most commonly frequency modulation (chirping).

For a real aperture radar (RAR), the azimuth resolution δ_{az} is determined by the angular beamwidth Θ_{az} of the antenna:

$$\Theta_{az} = \frac{\lambda}{L} \tag{3.3}$$

which is in turn determined by the size of the antenna L, and the center-frequency wavelength λ (typical imaging radars have fractional bandwidths of a few percent at most, making the monochromatic assumption valid). A typical L-band ($\lambda = 24$ cm) or C-band ($\lambda = 5$ cm) spaceborne imaging radar with a 10 m antenna and an operational altitude of 800 km would have an angular beamwidth of 19 km (L-band) or 8 km (C-band), which is much too coarse for practical applications.

3.3 Synthetic Aperture Radar

The coarse azimuth resolution limitation of RAR can be overcome through synthetic aperture radar (SAR) processing. The key principle behind SAR processing is the coherent exploitation of the Doppler phenomenon. Because of the motion of the SAR platform in the range direction, the range $r(t)$, and hence the phase $\phi(t)$, from the SAR antenna to any point on the ground at time t is given by:

$$\phi(t) = -\frac{4\pi}{\lambda} r(t) = -\frac{4\pi}{\lambda}\sqrt{r_0^2 + (vt)^2} \tag{3.4}$$

where r_0 is the range from the antenna to the target at closest approach, and v is the velocity of the SAR platform. The factor of 4 in the numerator of Equation 3.4 is due to the two-way travel of the radar pulse. This phase history has an associated Doppler frequency f_D:

$$f_D = \frac{1}{2\pi}\frac{\partial\phi}{\partial t} = \frac{2v \cdot u}{\lambda} \tag{3.5}$$

where $v \cdot u$ is the dot product of the SAR platform's velocity vector and the line of sight (LOS) vector from the platform to the scatterer. Defining an xyz coordinate system with x parallel to the azimuth direction, Equation 3.5 can be simplified to:

$$f_D = \frac{2vx}{\lambda R} \tag{3.6}$$

where x is the position in the $\hat{x}$ (i.e. azimuth) direction, and R is the range from the SAR platform to the scatterer (i.e. $R = \sqrt{x^2 + y^2 + z^2}$). From Equation 3.6, it is evident that SAR processing can resolve position in azimuth as a function of the Doppler frequency:

$$x = \frac{f_D \lambda R}{2v} \tag{3.7}$$

The phase history of the ground scatterer in azimuth produces a chirp function analogous to the chirp used in range compression. By applying an azimuth matched filter, SAR data can be compressed in azimuth. Conceptually, the responses from any given ground scatterer can be coherently integrated together over multiple radar pulses (within which the returns from the scatterer of interest occur at different positions and therefore Doppler frequencies). This yields an effective synthetic aperture size much larger than the physical size of the array, and a correspondingly narrow synthetic beamwidth. Azimuth matched filtering can improve the azimuth resolution to:

$$\delta_{az} = \frac{L}{2} \tag{3.8}$$

Surprisingly, the azimuth resolution is not limited by the physical dimensions of the antenna; in fact, smaller antennas correspond to finer azimuth resolutions. Conceptually, a smaller physical antenna will result in a larger physical beamwidth; any given ground scatterer will therefore be

illuminated by more radar pulses, allowing the azimuth matched filter to coherently integrate more observations of any given scatterer.

After range and azimuth compression, each pixel in a radar image is a complex-valued scalar which represents the convolution of the radar's impulse response with the distribution function of scatterers contained within the corresponding ground resolution element.

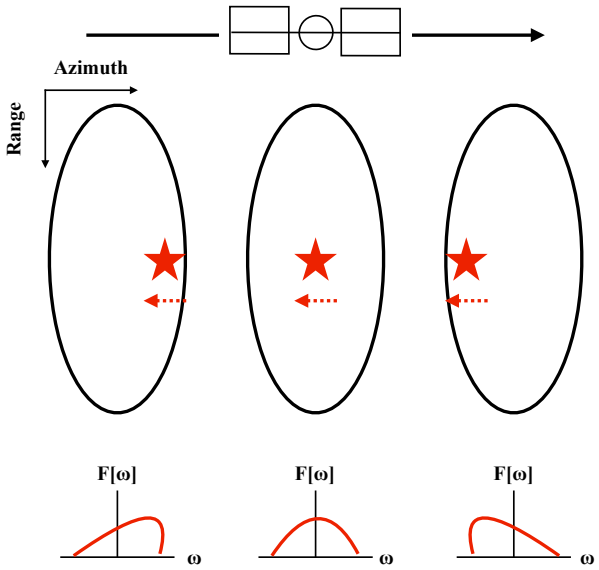

Figure 3.2: SAR processing utilizes the Doppler effect to achieve finer resolution in the azimuth direction. Motion of the SAR system in the positive azimuth direction results in an apparent motion of illuminated ground targets (red star) in the negative azimuth direction. A given scatterer will have an associated Doppler frequency (spectrally represented at bottom) that depends upon the position of the scatterer within the SAR swath. This unique mapping of Doppler frequency to azimuth position can be exploited to achieve finer azimuth resolution.

3.4 Interferometric Synthetic Aperture Radar

Repeat-pass Interferometric synthetic aperture radar (InSAR) is a technique used for determining the phase difference between spatially overlapping (coregistered) SAR images acquired at different times [Goldstein and Zebker, 1987; Goldstein et al., 1988; Massonnet et al., 1993; Rosen et al., 2000]. InSAR phase differences are more commonly used to characterize surface topography and/or deformation of the ground surface, although in principle, differences in phase can be attributed to a range of physical processes and phenomena.

The primary interferometric observable is the complex correlation:

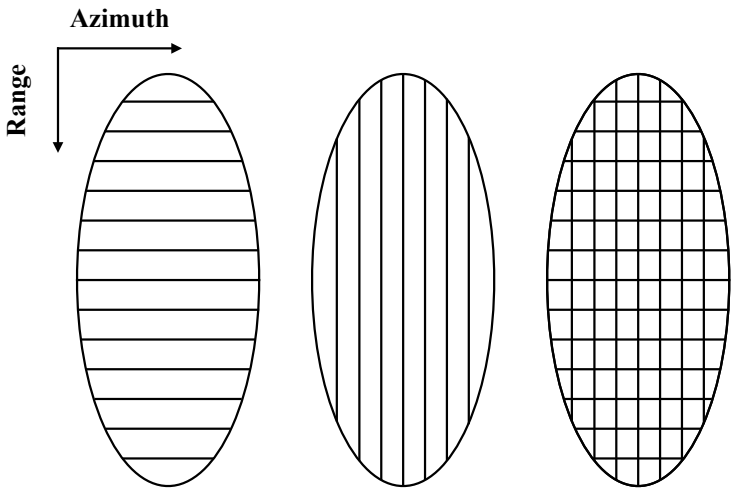

Figure 3.3: Illustration of the improvement in resolution provided by SAR processing within the radar swath. Left: Range compression results in a finer resolution in range. Center: Azimuth compression results in a finer resolution in azimuth. Right: The combination of range and azimuth compression in SAR processing yields finer resolution in both azimuth and range within the radar swath.

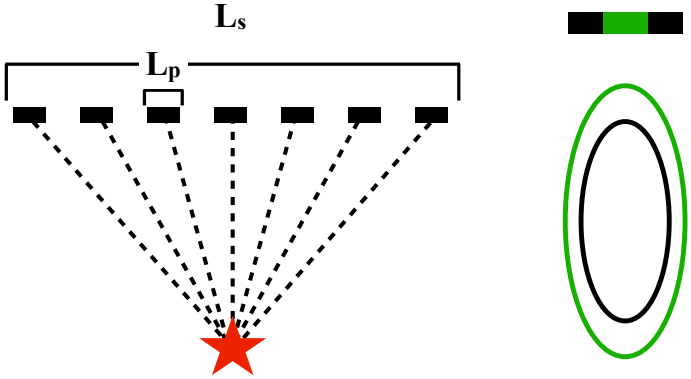

Figure 3.4: Left: Formation of a synthetic aperture of length L_s yields a finer azimuth resolution than is achievable by the physical antenna length L_p. Right: The smaller green physical antenna yields a larger radar beamwidth (and therefore swath size) than the larger antenna (black).

$$\hat{\gamma} = \frac{\langle s_1 s_2^* \rangle}{\sqrt{\langle s_1 s_1^* \rangle}\sqrt{\langle s_2 s_2^* \rangle}} \tag{3.9}$$

where $\hat{\gamma}$ is the estimated complex-valued correlation, s_1 and s_2 are two SAR images acquired at different times, $\langle \cdot \rangle$ is an ensemble averaging operator, and q^* is the complex conjugate of q. The complex correlation must be statistically estimated, hence SAR images are usually assumed spatially ergodic over a local neighborhood, and locally neighboring pixels are averaged together (in InSAR parlance, the image is 'multilooked') to estimate the complex correlation (at the expense of spatial resolution). The interferometric phase $\phi = \angle\hat{\gamma}$ and the correlation $\gamma = |\hat{\gamma}|$ are, in turn, determined by the complex correlation.

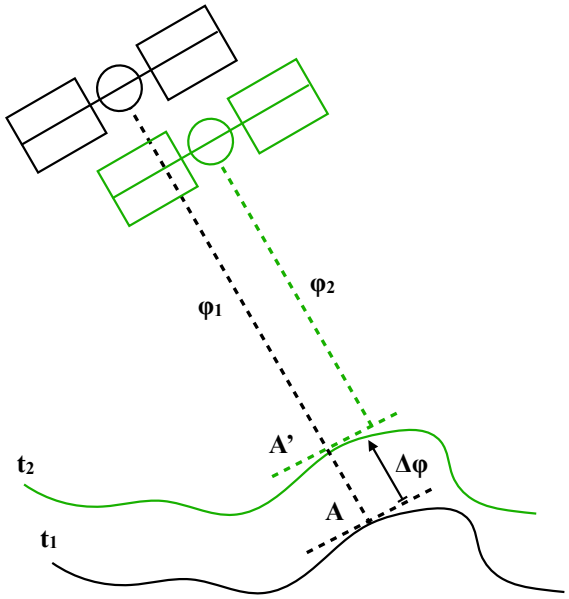

Figure 3.5: Illustration of the InSAR geometry. At time t_1 the SAR antenna illuminates a ground resolution element A on the ground surface (black). The range from the SAR antenna to the ground resolution element is contained within the phase of the measurement ϕ_1. At time t_2 the ground surface has deformed, experiencing a translation in the LOS direction. The SAR antenna illuminates the same ground resolution element A' on the ground surface (green). The range from the SAR antenna to the ground resolution element is contained within the phase of the measurement ϕ_2. The difference in phase between the two measurements, $\Delta\phi$, is proportional to the LOS deformation that occurs between times t_1 and t_2.

Assuming that both: 1) the topography of a region of interest is known, such as through a digital elevation model (DEM), and 2): the orbital and viewing geometry of the satellite is known, such that the relative position of the SAR platform between both image acquisitions is determined, then a pixel-wise difference in phase between two image acquisitions can be related to a LOS motion

Symbol	Name	Structure
ϕ_{defo}	Deformation Phase	Spatially/Temporally Correlated
ϕ_{topo}	Topographic Phase	Deterministic
ϕ_{atmo}	Atmospheric Phase	Spatially Correlated
ϕ_{sys}	Orbital/DEM Errors	Systematic
ϕ_n	Thermal Noise	Random
ϕ_{decor}	Decorrelation Phase	Can be Spatially/Temporally Correlated

Table 3.1: Interferometric Phase Terms

of the associated ground resolution element between image acquisitions (see Figure 3.5). At time t_1 a SAR system measures the phase ϕ_1 to a ground resolution element A, corresponding to the LOS range between the SAR antenna and the ground resolution element. At time t_2 the SAR platform makes another measurement of the phase ϕ_2 to the same ground resolution element A', which has now experienced a translation Δr in the LOS direction. If the surface topography and the orbital viewing geometry are both known, then the components of interferometric phase due to the surface topography and the viewing geometry can be removed, and the resulting unwrapped differential interferometric phase $\Delta\phi$ will be proportional to the LOS translation of the ground resolution element:

$$\Delta\phi = \phi_2 - \phi_1 = -\frac{4\pi}{\lambda}\Delta r \tag{3.10}$$

As we shall see below, Equation 3.10 implicitly assumes both a lack of error in the InSAR phase measurement, and neglects other sources of phase (i.e. other phase terms).

3.5 Interferometric Phase Terms

The presence of additional phase terms, which can be due to an array of physical processes, can complicate the retrieval of precise deformation-related phase terms from InSAR observations. Here we briefly describe the major sources of interferometric phase (see Table 3.1). Equation 3.10 can be more generally expressed as:

$$\Delta\phi = \phi_{defo} + \phi_{topo} + \phi_{atmo} + \phi_{sys} + \phi_{decor} + \phi_n \tag{3.11}$$

where $\Delta\phi$ is the measured interferometric phase, ϕ_{defo} is the interferometric phase change associated with surface of interest (commonly the signal of interest), and all other phase terms are errors, briefly described below.

3.5.1 Deformation Phase ϕ_{defo}

This is most often the phase signal of interest, and corresponds to a scalar translation of the resolution element in the radar line of sight direction. Deformation phase tends to be both spatially and temporally correlated, although this is highly dependent upon the specific signal of interest. The magnitude of the deformation signal in comparison to other error terms is also highly variable; in the case of coseismic deformation, it is often the largest phase term, while in slow slip applications, it can be dwarfed by atmospheric noise [Chen et al., 2017a].

3.5.2 Topographic Phase ϕ_{topo}

Traditional Range-Doppler SAR processing nominally assumes a planar surface, so any topographic variation over a region of interest will generate phase errors proportional to the topography. Because this is a deterministic process, prior topographic information, such as a DEM, can be used to characterize and remove topographic phase.

3.5.3 Atmospheric Phase ϕ_{atmo}

Temporal variations in the signal propagation delay of the atmosphere – usually due to changes in the tropospheric water content between image acquisitions – can induce phase terms in the order of fractional wavelengths. Tropospheric delay is non-dispersive, making it difficult to estimate and mitigate from InSAR measurements. Atmospheric phase is spatially correlated, and often correlated with topography, though is usually temporally uncorrelated. Atmospheric noise can be removed with global atmospheric reanalysis datasets [Jolivet et al., 2014], or spatial filtering [Hanssen, 2001; Lohman and Simons, 2005]. The most common filtering techniques include averaging redundant observations ('stacking') [Chen et al., 2017b], empirically estimating the statistics of atmospheric noise under a power law assumption [Lohman and Simons, 2005], and empirically removing atmospheric delay under a purely horizontally stratified assumption [Taylor and Peltzer, 2006].

Variations in total electron count (TEC) of the upper ionosphere can also generate phase terms that superficially resemble atmospheric noise. However, the two-way integrated phase shift is proportional to TEC and the square of the frequency. Because ionospheric phase is dispersive, it can be empirically estimated and removed, most commonly using range split-spectrum processing methods [Fattahi and Amelung, 2015].

3.5.4 Orbital/DEM Errors ϕ_{sys}

Imperfect knowledge of a SAR platform's orbital geometry can generate phase terms that are unrelated to geophysical properties of interest. Orbital phase errors often manifest as long-wavelength

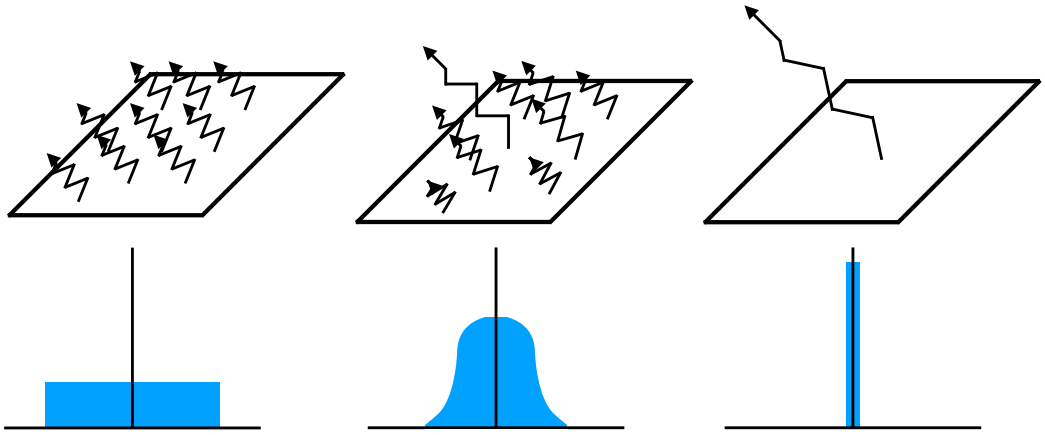

Figure 3.6: Scattering mechanism model, with scattering mechanisms (Top) and their associated phase PDFs (Bottom): Left, distributed scatterer: no dominant scatterer results in a uniform-like phase distribution. Center, dominant scatterer: a dominant scatterer results in a normal-like phase distribution. Right, single scatterer: a single scatterer results in a Dirac-like phase distribution.

phase ramps, and are therefore highly spatially correlated. These phase ramps can often be empirically removed, although if the deformation signal is of the same spatial scale, they can often be aliased together. The tight orbital tube control of modern SAR satellites like the Sentinel-1A satellite greatly minimizes the severity of orbital errors. Residual errors in the DEM used to remove topographic phase can result in residual DEM errors. DEM errors tend to be small features, and are often separable from broad geophysical signals.

3.5.5 Thermal Noise ϕ_n

Thermal noise is usually modeled as a white Gaussian noise process that contributes a random phase term.

3.5.6 Decorrelation Phase ϕ_{decor}

Interferometry requires coherence between two radar signals. Signal decorrelation, however, is common, and can limit the precision and accuracy of interferometric measurements. Signal decorrelation is caused by temporal variations in the dielectric properties and/or statistical scattering characteristics of a resolved surface between radar signal acquisitions [Zebker and Villasenor, 1992]. Variations in soil moisture, bound moisture in the vegetation canopy, vegetation growth, and relative movements of sub-resolution scatterers can all cause signal decorrelation, and generate a decorrelation phase term independent of the deformation phase term.

As shown in Equation 3.9, the complex correlation, and therefore the interferometric phase, must be statistically estimated. Signal decorrelation can be due to both stochastic, random fluctuations,

and systematic temporal variations [Zebker and Villasenor, 1992]. Stochastic decorrelation can most commonly arise from a lack of spatial ergodicity of the SAR signal, and from distributed scattering [Shanker et al., 2011; Agram, 2010; Agram and Simons, 2015].

Signal decorrelation due to distributed scattering is conceptually illustrated in Figure 3.6. In a perfectly distributed scattering regime, SAR backscatter is comprised of the coherent summation of scatter from many random sub-resolution scattering elements (graphically represented by bent arrows). The interferometric phase of a collection of random scatterers will be uniformly distributed between $-\pi$ and π (the PDF of phase is graphically represented by the blue rectangle). In a dominant scattering regime, a single scattering element will dominate the backscatter return; the PDF of phase will be centered around a mean value, and will be increasingly peaked as the dominant scatterer becomes more and more dominant [Just and Bamler, 1994; Shanker and Zebker, 2007]. In the limit where backscatter arises from a single scatterer, the phase PDF will be a deterministic, Dirac delta function. The degree to which scattering is distributed rather than dominated by a single scatterer (such as a corner reflector) will dictate the degree to which stochastic decorrelation may degrade the interferometric signal. Similarly, spatial averaging of a non-ergodic signal can introduce stochastic decorrelation, as the pixels averaged together will exhibit different phase statistics.

In contrast to stochastic decorrelation phase, systematic decorrelation phase can arise from systematic temporal changes in the surface scattering properties of a resolution element. A change in the dielectric permittivity of the surface or vegetation canopy can introduce a systematic phase signal which leads to signal decorrelation [De Zan et al., 2014]. Similarly, correlated motions of sub-resolution scattering elements,such as the growth of crops between image acquisitions, can introduce a systematic phase signal that is unrelated to the bulk ensemble deformation of the resolution element [De Zan et al., 2015].

Systematic decorrelation signals are commonly neglected in InSAR studies, and decorrelation is assumed to be purely stochastic. As a result, it is often treated jointly with thermal noise as a single error term. However, stochastic and systematic decorrelation can be considered independently, as will be discussed in Chapters 5, 6, and 7.

3.6 Time Series Analysis

The Small BAseline Subset (SBAS) algorithm is a method for characterizing the temporal evolution of the ground deformation of a surface of interest using a network of InSAR observations [Berardino et al., 2002]. The SBAS algorithm utilizes multiple combinations (i.e. subsets) of the total population of interferograms over an area of interest; these subsets are usually chosen such that the interferogram pairs in each subset have small orbital and temporal baselines, such that spatial and temporal decorrelation are minimized. A singular value decomposition (SVD) is then applied to solve for the best-fitting time series of deformation from the various subsets of interferograms.

Consider a collection of N coregistered SAR images over a region of interest, where the i^{th} image is acquired at time t_i. The total number of interferograms M that can be formed from this collection of N scenes will satisfy the following inequality:

$$\frac{N}{2} \leq M \leq \frac{N(N-1)}{2} \tag{3.12}$$

where M will ultimately be determined based upon the thresholds of spatial and temporal baseline chosen for forming the subsets used during the inversion. Now consider a particular pixel within the collection of interferograms, noting that the following equations apply to the image at-large. Assuming that all interferograms have been unwrapped, the topographic phase component removed, and all other error terms are negligible, this pixel has a corresponding M x 1 vector of unwrapped interferometric phase values corresponding to the M interferograms:

$$\Delta\phi^T = [\Delta\phi_1, \Delta\phi_2, ..., \Delta\phi_M] \tag{3.13}$$

where the m^{th} interferometric phase is related to the LOS change in deformation between the i^{th} and j^{th} SAR images used to form the interferogram:

$$\Delta\phi_m = \phi_j - \phi_i \approx -\frac{4\pi}{\lambda}(d_j - d_i) \tag{3.14}$$

where λ is the radar wavelength, and d_i is the LOS deformation from the SAR platform to the pixel of interest in the i^{th} SAR scene, referenced relative to time t_0. We can construct a linear system of M equations with *N-1* unknowns of the form of 3.14:

$$A\phi = \Delta\phi \tag{3.15}$$

where A is an incidence-like M x *N-1* matrix, ϕ^T is an *N-1* x 1 vector of unknown phase values referenced to the t_0 scene, and $\Delta\phi^T$ is an M x 1 vector of known interferometric phase values.

The vector of unknown phase values ϕ^T can be approximated as:

$$\phi = A^{-g}\Delta\phi \tag{3.16}$$

where A^{-g} is the generalized inverse of the matrix $\mathbf{A}$. The matrix A can be decomposed using the singular value decomposition as follows:

$$A = U\Sigma W^T \tag{3.17}$$

where if $rank(A) = r$, U is a collection of the r left singular vectors of A, W are the r right singular vectors of A, and $\Sigma = diag(\sigma_1, ..., \sigma_r)$ is a diagonal matrix of the r singular values of A. The Moore-Penrose pseudo-inverse $A^\dagger$ can then be chosen for A^{-g}, where:

$$A^\dagger = W\Sigma^{-1}U^T \tag{3.18}$$

The minimum norm constraint of the SVD method can often lead to large, physically unrealistic discontinuities in deformation time series; for this reason Equation 3.14 is often modified by changing the vector of unknown phase values to the mean phase velocities between time-adjacent SAR scenes:

$$Bv = \Delta\phi \tag{3.19}$$

where the vector of phase velocities is:

$$v^T = [v_1 = \frac{\phi_1}{t_1 - t_0}, ..., v_N = \frac{\phi_N - \phi_{N-1}}{t_N - t_{N-1}}] \tag{3.20}$$

Based upon the application, signal of interest, and assumed deformation model, Equations 3.15 and 3.19 can be modified accordingly. The modifications made for applications in permafrost areas are described below.

3.6.1 ReSALT Model

The ReSALT (Remotely Sensed Active Layer Thickness) algorithm measures ground deformation due to seasonal freeze/thaw cycles, and then inverts this deformation signature for an estimate of the seasonal active layer thickness [Liu et al., 2012; Schaefer et al., 2015]. Using the ReSALT method, an analytical expression for seasonal subsidence is derived from a model of frozen soil expansion. As the active layer thaws, ice in the soil undergoes a phase change to liquid water, decreasing in volume and causing the ground to subside. Conversely, when the soil freezes in autumn and early winter, water in the soil changes to ice and the ground heaves. When the active layer freezes completely in mid-winter, the heave stops. This subsidence model assumes that the entire active layer is frozen at the beginning of the thaw season, and the active layer thaws continuously from the top downward as the thaw season progresses. As the active layer thaws, pore-bound frozen water undergoes a phase

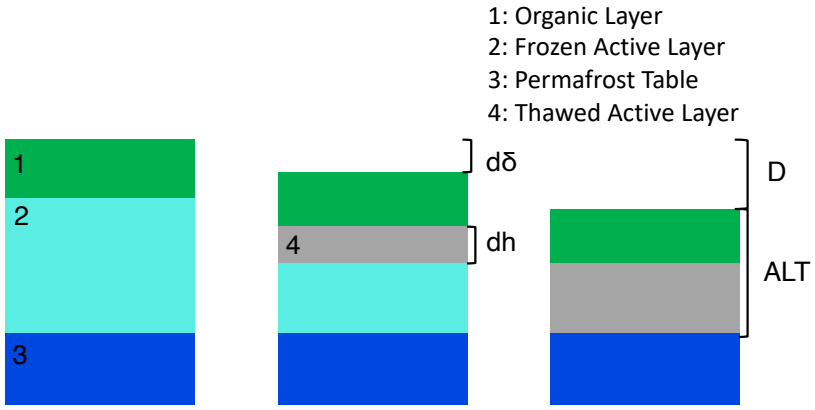

Figure 3.7: Depiction of the seasonal deformation model first developed in Liu et al. [2012]. At the onset of thaw (left), above-freezing conditions (represented by ADDT) induce a phase change of pore-bound water from solid to liquid. The 9% difference in density between solid and liquid water results in a reduction of the pore space occupied by water, and a subsidence of the soil column. A given change dh in the thaw depth of the soil column results in a corresponding subsidence $d\delta$ (middle). The maximum seasonal subsidence D corresponds to the maximum seasonal thaw depth, or active layer thickness ALT (right).

change to liquid, decreasing its total effective volume by approximately 9%, and causing the ground to subside as a result. Assuming that surface subsidence is solely due to the phase change of solid to liquid water, we can express the incremental thawing of the active layer as:

$$d\delta = PS\frac{(\rho_w - \rho_i)}{\rho_i}dh \tag{3.21}$$

where $d\delta$ is the incremental change in surface subsidence [m], P is soil porosity [$m^3\ m^{-3}$], S is soil moisture fraction of saturation [-], ρ_w is the density of water [kg m^{-3}], ρ_i is the density of ice [kg m^{-3}] and dh is the incremental thickness of thawed soil column [m]. Integrating Equation 3.21 over the definite interval of the active layer will yield the total ground subsidence E expected for an active layer of a given thickness ALT:

$$E = \int_0^{\delta} d\delta = \int_0^{ALT} PS\frac{(\rho_w - \rho_i)}{\rho_i}dh \tag{3.22}$$

where porosity and saturation can be implicit functions of depth.

The ReSALT technique models total measured deformation as a linear combination of elastic subsidence/uplift due to the seasonal thawing and freezing of pore space water, and inelastic subsidence caused by interannual, long-term changes in ALT and thermokarst subsidence [Liu et al.,

2012], (see (Figure 3.8)). Total seasonal deformation is modeled as a function of the square root of the normalized annual degree days of thaw (ADDT). The square root of ADDT has been previously shown to be related to the amount of permafrost subsidence as a consequence of the thermal diffusion equation (as in Stefan's equation; [Harlan and Nixon, 1978]).

$$D_{seasonal} = E\sqrt{ADDT} \tag{3.23}$$

where $D_{seasonal}$ is the seasonal deformation [m], ADDT is the normalized accumulated degree days of thaw [$^{\circ}C^{-\frac{1}{2}}days^{-\frac{1}{2}}$], and E is the seasonal coefficient [$m\ ^{\circ}C^{-\frac{1}{2}}days^{-\frac{1}{2}}$].

The long-term, interannual deformation is modeled as linear with time, i.e.:

$$D_{long-term} = R(t_2 - t_1) \tag{3.24}$$

where $(t_2 - t_1)$ is the temporal separation of the two SAR scenes used to generate an interferogram, and R is the long-term subsidence rate [$\frac{m}{years}$]. The total deformation D therefore is a linear combination of the seasonal and long-term deformation signatures:

$$D = D_{seasonal} + D_{long-term} = E(\sqrt{ADDT_2} - \sqrt{ADDT_1}) + R(t_2 - t_1) \tag{3.25}$$

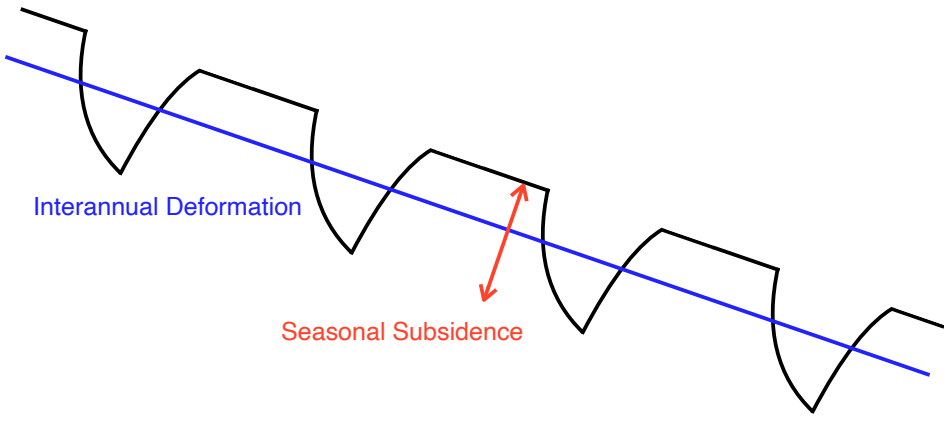

Figure 3.8: Deformation is decomposed into seasonal subsidence (E; Equation 3.22) due to seasonal freezing/thawing of the active layer, and long-term trends in subsidence (R; Equation 3.24) due to thinning of permafrost or thermokarst.

Using the ReSALT algorithm results in a modified form of Equation 3.19. Through a system of linear equations, interferometric phase $d\phi$ is proportional to seasonal subsidence E, long-term

subsidence rate R and ϵ_{topo}, a topographic error term that accounts for errors in the digital elevation model [Liu et al., 2014]. This equation can be expressed in matrix form as:

$$\begin{bmatrix} \delta\phi_1 \\ . \\ . \\ . \\ \delta\phi_N \end{bmatrix} = \begin{bmatrix} t_{2,1} - t_{1,1} & \sqrt{ADDT_{2,1}} - \sqrt{ADDT_{1,1}} & B_{perp,1} \\ ... & ... & ... \\ ... & ... & ... \\ ... & ... & ... \\ t_{2,N} - t_{1,N} & \sqrt{ADDT_{2,N}} - \sqrt{ADDT_{1,N}} & B_{perp,N} \end{bmatrix} \begin{bmatrix} R \\ E \\ \epsilon_{topo} \end{bmatrix} \tag{3.26}$$

where $\delta\phi_i$ terms are InSAR measurements of surface deformation [m] for the i^{th} interferogram, $t_{2,i} - t_{1,i}$ are the differences in time between any two scenes used to generate the i^{th} interferogram, $\sqrt{ADDT_{2,i}} - \sqrt{ADDT_{1,i}}$ are the differences in the square root of the accumulated degree days of thaw between the two scenes used to generate the i^{th} interferogram, and B_{perp} is the spatial baseline of the i^{th} interferogram. These deformation components represent, respectively, long-term trends in subsidence (R [m yr^{-1}], deformation associated with the seasonal freezing/thawing of the active layer (E [m]), and an error term associated with errors in the digital elevation model used (ϵ_{topo}).

3.6.2 ReSALT Model Sensitivity to Soil Moisture

Gaussian error propagation of the ReSALT model demonstrates that total uncertainties in retrieved active layer thickness are dominated by uncertainties in three input parameters: 1) the measured subsidence; 2) the total soil carbon content (which partially determines the vertical porosity distribution); and 3) the soil moisture saturation fraction. Deformation uncertainty accounts for $\sim 80\%$ of total ALT uncertainty. Consequently, the fidelity of retrieved ALT depends heavily on the deformation estimate. However, soil carbon content and saturation account for $\sim 19\%$ of ALT uncertainties, which represents a large sensitivity to assumed model parameters (i.e. not uncertainties of direct observables) [Liu et al., 2012].

We can approximate the adjoint of the model (i.e. its sensitivity with respect to saturation) by re-expressing Equation 3.21:

$$dh = \frac{\rho_i}{(\rho_w - \rho_i)} \frac{1}{PS} d\delta \tag{3.27}$$

where an incremental deformation $d\delta$ is proportional to an incremental thawing of the active layer dh by $\frac{1}{S}$. The adjoint, $\frac{\partial H}{\partial S}$, is therefore proportional to the square of the saturation fraction:

$$\frac{\partial H}{\partial S} \propto S^{-2} \tag{3.28}$$

As the saturation fraction itself decreases, the ReSALT retrieval algorithm increasingly becomes more sensitive to uncertainties in saturation fraction. In highly saturated environments ($S \approx 1$) such as the Alaskan North Slope or the Yukon-Kuskokwim river delta, ALT uncertainties due to incorrectly assumed saturation fraction are relatively modest, and dwarfed by observational uncertainty (InSAR deformation uncertainties). However, even with a saturation fraction as high as $S = 0.84$, algorithm uncertainty due to soil moisture becomes comparable to observational uncertainty. Applying the ReSALT algorithm in regions where low saturation fractions can be common – such as sporadic permafrost regions or inland, non-river delta discontinuous permafrost regions – would benefit greatly from independent estimates of saturation fraction or soil moisture state. Importantly, radar remote sensing measurements are always sensitive to an average value over the radar resolution cell; in regions that exhibit high spatial variability of seasonal subsidence, soil moisture content, or soil porosity over the radar resolution cell, the inferred subsidence or soil moisture will be a bulk average of all values within the resolution cell, which can further contribute to measurement uncertainty.

3.7 Closure Phase

As in Equation 3.9, the interferometric complex correlation is defined as:

$$\tilde{\gamma} = \frac{\langle s_1 s_2^* \rangle}{\sqrt{\langle s_1 s_1^* \rangle \langle s_2 s_2^* \rangle}} \tag{3.28}$$

where s_1 and s_2 are complex-valued signals, and $\langle \cdot \rangle$ is an ensemble averaging operator, which, in practice, is usually approximated by a local spatial average [Zebker and Villasenor, 1992]. The complex correlation is a measure of signal similarity; in the case of InSAR, it represents the similarity in the surface scattering properties of a given pixel in a pair of radar SLCs as a function of time. The analogous quantity for a triplet of three unique radar SLCs is the complex bicoherence, a quantity frequently used in astrophysical interferometry [Jennison, 1958; Chael et al., 2018; Blackburn et al., 2019]. For any triplet of three SAR images, the bicoherence $\tilde{\Xi}$ is defined as the product of two complex coherences multiplied by the complex conjugate of the third [Zwieback et al., 2015b]:

$$\hat{\tilde{\Xi}}_{123} = \hat{\gamma}_{12} \hat{\gamma}_{23} \hat{\gamma}_{13}^* \tag{3.29}$$

Like the complex correlation, the bicoherence has an associated phasor term. The closure phase ξ_{123} is simply the argument of the bicoherence $\xi_{123} = \angle \hat{\tilde{\Xi}}_{123}$, and is therefore a linear combination of the three interferometric phases of the three possible scene pairs of the triplet:

$$\xi_{123} = \angle\hat{\Xi}_{123} = \phi_{12} + \phi_{23} - \phi_{13} \tag{3.30}$$

The closure phase is invariant to any purely propagational phase terms – such as surface deformation, atmospheric delay, or topographic errors – that contribute to the interferometric phase of the individual SAR pairs [De Zan et al., 2014; Zwieback et al., 2015b; Michaelides et al., 2019b]. This point is illustrated in Figure 3.9. Under idealized surface deformation, the entire resolution element of a surface deforms together coherently, such that the physical arrangement of sub-resolution scattering elements which contribute to the backscattered signal is unchanged with time. This is analogous to stating that the deformation is on a spatial scale much broader than the resolution of the radar system. Under this assumption (which is implicitly made for most InSAR applications), any deformation that occurs between times t_1 and t_3 should be exactly equal to the sum of the deformation contained between times t_1 and t_2 and t_2 and t_3. That is, the interferometric phases should form a 'closed loop', with no excess or deficit interferometric phase.

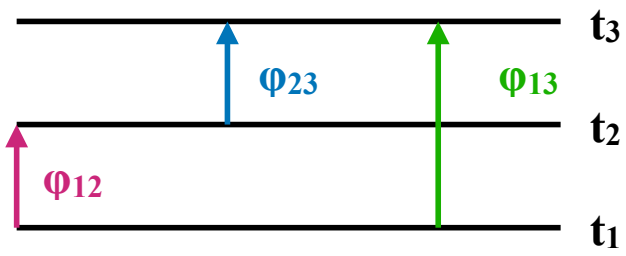

Figure 3.9: Closure phase is invariant to simple, piston-like deformation (i.e. the entire resolution element moves coherently). For a surface experiencing uplift and imaged at times t_1, t_2, and t_3, 3 possible interferograms, ϕ_{12}, ϕ_{23}, and ϕ_{13} can be formed. The sum of the deformations measured by ϕ_{12} and ϕ_{23} is equal to the deformation measured by ϕ_{13}, so the closure phase should evaluate to zero.

For an idealized, perfectly coherent scattering element, the closure phase should always be identically zero. However, a combination of stochastic signal decorrelation and systematically variable attenuation rates and transmission wavenumbers during volume scattering can generate nonzero closure phase [De Zan et al., 2015; Michaelides et al., 2019b]. The stochastic component of closure phase is graphically illustrated in 3.10. In the absence of systematic decorrelation phenomena, such as variable dielectric permittivity, interferometric phases are purely propagative. Stochastic fluctuations in phase noise (represented by dotted lines) result in a closure phase signal that is zero mean and independent of the complexity of the interferometric phase. The standard deviation of the closure phase is linearly proportional to the interferometric phase standard deviation. In the limit where the interferometric phase noise term vanishes – the interferometric noise becomes

deterministic – the closure phase identically evaluates to zero.

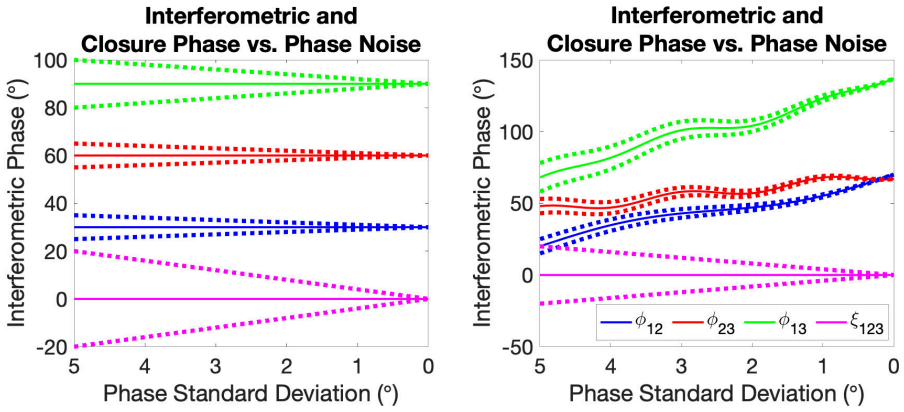

Figure 3.10: Stochastic component of closure phase as a function of the phase noise standard deviation. When systematic decorrelation due to changes in dielectric permittivity are neglected, stochastic fluctuations in phase noise are the only cause of nonzero closure phase. A triplet of three interferometric phases (green, red, and blue) are plotted as a function of the standard deviation of the phase noise; dotted lines represent error envelopes. The resulting closure phase is displayed in magenta. Regardless of the complexity of the interferometric phasor, closure phase arising from stochastic decorrelation fluctuations are zero mean, and approach zero as the phase noise term approaches zero.

Closure phase arising from both stochastic and systematic decorrelation effects is illustrated in Figure 3.11. The closure phase associated with a triplet of SLCs from the Sentinel-1A satellite taken over Death Valley, California is formed with different numbers of looks taken in both range and azimuth. For the 1-look case, closure phase is identically zero across the image; there is no phase deficit or excess. However, as looks are taken, phase excess and deficit occurs, and nonzero closure phase can be observed across the scene. As the number of looks is increased, a strong correlation between phase closure and surface geomorphology (and therefore surface scattering properties) is observed. The central 'yellow' feature with consistently positive closure phase corresponds to Cottonball and Badwater basins, two playa lakes occupying the lowest elevation of Death Valley. In contrast, alluvial fans, arroyos, and ephemeral streams that discharge into the playas display closure phase values near zero, as does the broad alluvial plan to the east of Badwater Basin, the Amargosa Range, and the Funeral Mountains. These closure phase signals contain both stochastic and systematic terms, with the systematic components due to changes in the surface scattering properties and/or dielectric permittivity of the surface.

We multilook SAR images under the assumption of signal ergodicity. Due to the lack of multiple realizations of each SLC, we average several adjacent pixels together under the assumption of spatial ergodicity; i.e. surface scattering properties are identical, and each pixel corresponds to a different realization from the same distribution of scattering elements. When perfect spatial ergodicity is not

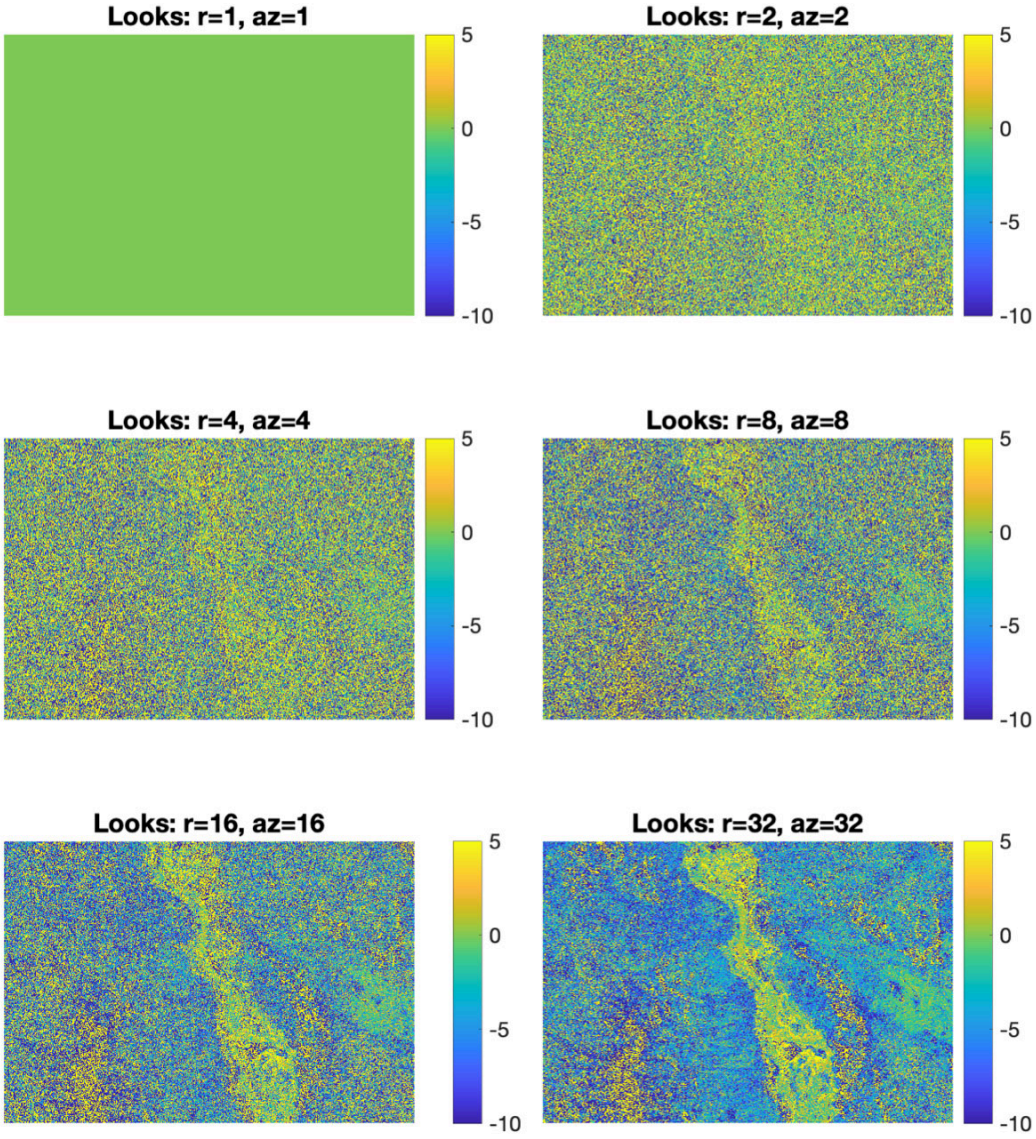

Figure 3.11: Nonzero closure phase (phase excess or deficit) as a function of the number of looks taken in range (r) and azimuth (az) during phase estimation for a triplet of Sentinel-1A SLCs over Death Valley, California.

preserved (which it rarely is in natural terrain types), stochastic decorrelation of the signal occurs. This corresponds to the 'white-noise-like' component of the closure phase, and is particularly evident over the Panamint and Amargosa ranges, which are very rough surfaces and thus highly non-ergodic.

Nonzero closure phase signals which are highly correlated with surface geomorphology may be due instead to systematic signal decorrelation, such as changes in the dielectric permittivity of the scattering surface between image acquisitions. Increasing the number of looks during phase estimation over areas with a moderate to high degree of ergodicity results in a decrease in the standard deviation of the closure phase, and an increasingly more accurate estimate of the closure phase. This is demonstrated in Figure 3.12 calculated over a highly-coherent portion of Badwater Basin. The standard deviation of the closure phase monotonically decreases as the number of looks used during phase estimation; at 16 looks in range and azimuth (corresponding to a pixel size of $\sim$ 80 x 240 m), the standard deviation of the closure phase is smaller than the mean of the closure phase estimate.

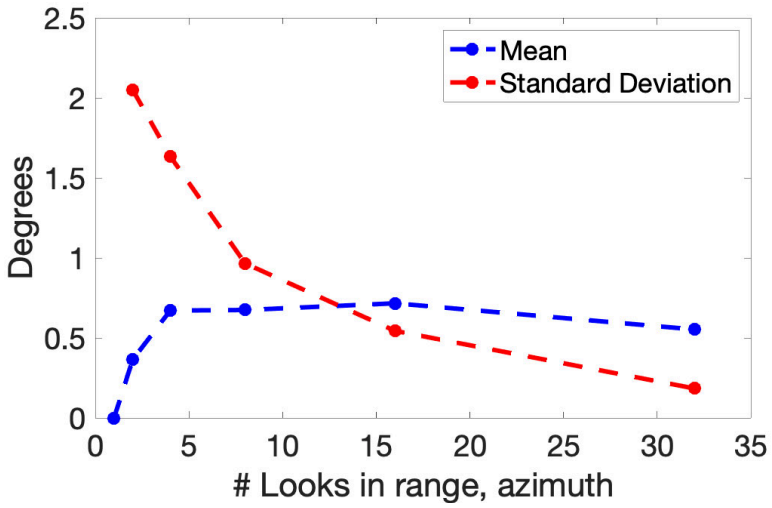

Figure 3.12: Mean (blue) and standard deviation (red) of estimated closure phase over Badwater Basin as a function of the number of looks during phase estimation.

Chapter 4

Resolving Permafrost-Wildfire Interactions with InSAR

The Yukon-Kuskokwim (YK) Delta is a region of discontinuous permafrost in the subarctic of southwestern Alaska. Many wildfires have occurred in the YK Delta between 1971 and 2015, impacting vegetation cover, surface soil moisture, and the active layer. Herein, we demonstrate that the Remotely Sensed Active Layer Thickness (ReSALT) algorithm can resolve the post-fire active layer dynamics of tundra permafrost. We generate a stack of Advanced Land Observing Satellite Phased Array type L-band Synthetic Aperture Radar (ALOS PALSAR) interferograms over a study region in the YK Delta spanning 2007-2010. We apply ReSALT to this stack of interferograms to measure seasonal subsidence associated with the freezing and thawing of the active layer and subsidence trends associated with wildfire. We isolate two wildfire-induced subsidence signatures, associated with the active layer and the permafrost layer. Fire increases the active layer thickness, which recovers to pre-fire values after approximately 25 years. Simultaneously, fire gradually thins the permafrost layer by 4 meters, which recovers to pre-fire thickness after 70 years.

4.1 Introduction

Air temperatures in high-latitude regions are increasing at twice the global rate, which threatens the distribution and stability of permafrost regions [Jorgenson et al., 2001; Osterkamp et al., 2009]. Among terrestrial biomes, tundra and boreal ecosystems underlain by permafrost contain the largest below-ground carbon reservoirs globally [Hugelius et al., 2014], and these regions are also significantly impacted by wildfires [Loranty et al., 2016; Genet et al., 2013]. As air temperatures rise and regional climate changes, wildfires are expected to increase in frequency over the Arctic domain [Hinzman et al., 2005]. Under favorable environmental conditions, tundra regions are susceptible to burn

[Rocha et al., 2012]. Wildfires rapidly transfer soil and vegetation carbon into the atmosphere. More significantly, post-fire increases in thaw depth facilitate increased microbial decomposition and heterotrophic respiration within the thawed soil column, which gradually releases soil carbon to the atmosphere years after the wildfire event [Natali et al., 2014; Bret-Harte et al., 2013; Rocha et al., 2012; Grosse et al., 2011]. Furthermore, terrestrial arctic regions are thought to contain roughly twice the amount of carbon currently in the atmosphere, so any increases in wildfire frequency in the Arctic could have a marked effect on the global carbon cycle [Schuur et al., 2008].

Fire removes a portion of the insulating organic layer, increasing the ALT for years after the fire [Swanson, 1981; Mackay, 1995; Shur and Jorgenson, 2007; Rocha et al., 2012]. Regions with poor drainage, thick organic layers, and fine-grained soil recover rapidly after fire [Shur and Jorgenson, 2007]. As the surface vegetation grows back after a fire, the organic layer re-accumulates, and the ALT returns to its pre-fire values [Shur and Jorgenson, 2007; Mackay, 1995; Brown et al., 2015]. However, how long this recovery takes is poorly understood. As wildfire frequency is expected to increase over arctic regions through the 21st century, a more complete understanding of the interaction between wildfire, permafrost, and active layer dynamics is necessary.

The Yukon-Kuskokwim (YK) Delta is a subarctic lowland in the discontinuous permafrost zone dotted with lakes, thaw ponds, and wetlands [Burns, 1964]. The YK Delta represents an ecologically-driven permafrost system where vegetation dynamics control the formation of permafrost. Vegetation such as moss and grass and the surface layer of organic material thermally insulate the soil in summer, allowing the buildup of a permafrost layer and controlling ALT [Shur and Jorgenson, 2007; Pewe, 1963]. Major wildfires have burned across the YK Delta many times over the last hundred years. We focus on a wetland tundra region within the Izaviknek Highlands approximately 80 km northwest of Bethel, Alaska that has experienced more than 20 distinct wildfires since 1971 (Figure 4.1). We leverage the high density of fire scars of various ages to study ALT and permafrost thickness response after fire using the ReSALT algorithm.

4.2 Quantifying Permafrost Processes and Wildfire Interactions

4.2.1 InSAR Processing

Using 8 repeat pass ALOS PALSAR FBS (wavelength $\lambda = 23.6$ cm) scenes acquired between 08/12/2007 - 01/02/2010, we generate a stack of coregistered interferograms over the YK Delta study region using the motion-compensation processing algorithm developed in the Stanford Radar Group [Zebker et al., 2010]. We use the 5m resolution optical stereophotogrammetric ArcticDEM dataset to remove the topographic phase term from all interferograms. We multilook interferograms

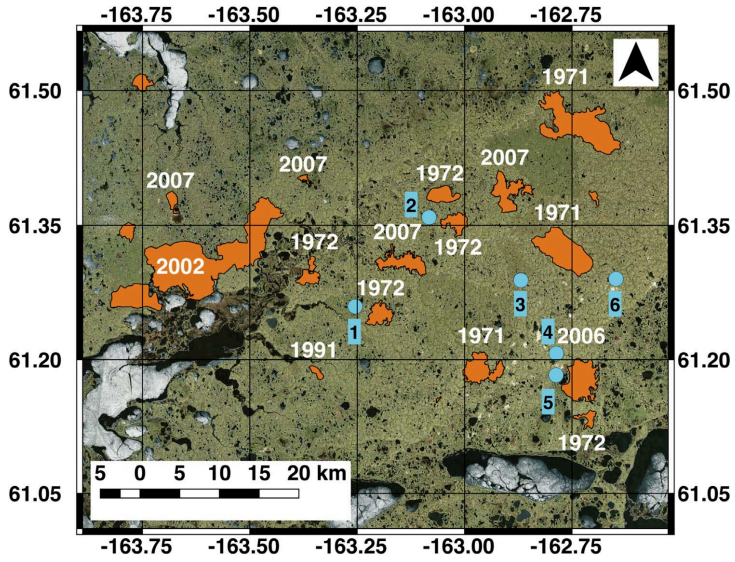

Figure 4.1: The Yukon-Kuskokwim Delta field study area. Wildfire burn zones are shown in orange and labeled by year of burn. Blue dots are the locations of field camps from the 2016 field campaign; in-situ measurements of thaw depth were made around these sites, characterizing both unburned and burned regions in nearby fire scars (e.g. the 2006 fire adjacent to site 5 and the 2007 fire adjacent to site 2).

for increased signal-to-noise ratio at the expense of spatial resolution, and apply a Goldstein filter to smooth out interferogram phase noise and aid in phase unwrapping [Goldstein and Werner, 1998]. We unwrap interferograms using the SNAPHU algorithm described in [Chen and Zebker, 2002], and deramp them to remove the best fit first-order orbital phase error [Chen et al., 2017a]. We visually examined the set of interferograms and removed those exhibiting ionospheric noise or severe decorrelation noise (see Appendix B for a table of interferograms used in the final analysis). As InSAR measures deformation in the line-of-sight (LOS) direction of the radar, we apply a LOS correction to all interferograms to decompose the deformation values into horizontal and vertical orientations [Chen et al., 2017a]. We mask consistently incoherent pixels from which precise deformation measurements cannot be retrieved, which masks out major lakes and water bodies in the study region. As a reference point, we chose an unburned location (61.3544°N,163.0911°W; near site 2 in Figure 4.1) where we measured ALT in 2016 and then apply our frozen soil expansion model to determine the absolute phase differences within the InSAR stack [Liu et al., 2012; Schaefer et al., 2015].

We apply the ReSALT algorithm on the 14 interferograms listed in B. These interferograms encompass scenes from the onset and end of summer thaw, as well as winter freeze-up. In general, the use of more interferograms will result in a more robust solution. Compared to the ALOS satellite, surface decorrelation is more severe for interferograms generated by the ERS-1 and ERS-2 satellites

due to their longer temporal baselines and relatively shorter wavelength ($\lambda \approx 5$ cm vs. $\lambda \approx 23$ cm). For this reason previous applications of the ReSALT algorithm have discarded winter scenes to avoid the potential for misinterpreting spurious signals associated with snow cover [Liu et al., 2010; Liu et al., 2012]. The longer wavelength ($\lambda \approx 23$ cm) and shorter temporal baseline of the ALOS PALSAR system used in this study both mitigate surface decorrelation associated with winter snow cover. Because snow cover is uncorrelated with time between winter-summer and multiple year winter scene pairs, we retain interferograms containing a winter scene that exhibit surface correlation comparable to summer-summer interferograms, but note that their inclusion is a potential source of uncertainty.

As derived in Section 3.6.1, the deformation time series model used is of the form:

$$\begin{bmatrix} \delta\phi_1 \\ . \\ . \\ . \\ \delta\phi_N \end{bmatrix} = \begin{bmatrix} t_{2,1} - t_{1,1} & \sqrt{ADDT_{2,1}} - \sqrt{ADDT_{1,1}} & B_{perp,1} \\ ... & ... & ... \\ ... & ... & ... \\ ... & ... & ... \\ t_{2,N} - t_{1,N} & \sqrt{ADDT_{2,N}} - \sqrt{ADDT_{1,N}} & B_{perp,N} \end{bmatrix} \begin{bmatrix} R \\ E \\ \epsilon_{topo} \end{bmatrix} \tag{4.1}$$

These deformation components represent, respectively, long-term trends in subsidence (R [m yr^{-1}], deformation associated with the seasonal freezing/thawing of the active layer (E [m]), and an error term associated with errors in the digital elevation model used (ϵ_{topo}).

ADDT is calculated from available air temperature records at Bethel, Alaska, and normalized such that the maximum value is one at the end of the thaw season [Liu et al., 2012]. The ReSALT algorithm solves for E, R, and ϵ_{topo} on a pixel-by-pixel basis using least-squares regression. This technique represents a modification of the Small Baseline Subset (SBAS) algorithm originally formulated in [Berardino et al., 2002] and used extensively in InSAR time series analysis [Hooper, 2008; Schmidt and Burgmann, 2003; Lauknes et al., 2010; Chen et al., 2014]. Error is taken to be the model residual errors; the root mean square error of the differences between the subsidence model and deformations from the interferogram stack [Liu et al., 2012; Liu et al., 2015; Schaefer et al., 2015]. The residual errors, as well as uncertainties in all model parameters, are propagated through the inversion routine and summed in quadrature to derive total model uncertainties. For a given stack of SAR images, this yields a finely-sampled map of derived ALT, and associated uncertainties.

We assume organic content and thus P decrease exponentially with depth from pure organic to pure mineral soil, consistent with field observation [Liu et al., 2012]. S represents the fraction of soil pore space filled with water and is safely assumed to be fully saturated soil on the YK Delta ($S = 1$). ALT is calculated using numerical integration, and uncertainty in ALT is estimated using Gaussian error propagation of uncertainty in E [Liu et al., 2012].

4.2.2 Fire Response Model

Fire increases ALT by removing insulating organic matter from the surface (Figure 4.2). Grass, moss and dead organic matter build up over time to create an organic layer that insulates the soil from warm air temperatures. Black soot increases absorption of sunlight and fire removes part of the organic layer, resulting in deeper summer thaw and larger ALT, and the potential for thinning of permafrost at depth. Rapid vegetation regrowth after a fire eliminates the albedo effect, but recovery of the organic layer takes many years. As the organic layer becomes thicker, its insulating effect increases and the ALT recovers back to pre-fire conditions [Shur and Jorgenson, 2007].

We use the ReSALT output to create a fire response model of seasonal subsidence and permafrost thickness. We assume post-fire variations in the seasonal subsidence result from variations in ALT, while variations in subsidence trends result from changes in permafrost thickness. Thermokarst subsidence is minimal in the YK Delta because the soil contains very little excess ground ice in the form of ice wedges or layers [Pewe, 1963; Ludwig et al., 2018]. Satellite imagery shows the 2007 fires occurred several months before the first ALOS scene, so all the fires in the study region occurred before the ALOS record.

To create a general permafrost thickness and ALT response model, we assume variations in seasonal subsidence and subsidence trends in burn scars result solely due to variations in time since initial burn. This implicitly assumes that all areas burned exhibit an identical fire response. We calculate the mean ReSALT estimates of seasonal subsidence, subsidence trend, ALT, and their associated uncertainties within each fire zone, yielding 13 estimates of post-fire seasonal subsidence and subsidence trend for 6 different points in time. We apply a student t-test at 95% significance to determine if values within the fire scars show a significant difference to values outside the scars. We generate two general response functions by sampling the subsidence trend and seasonal subsidence of each fire scar at its respective time since burn, spanning 1971-2007. We apply a nonlinear least-squares best fit to the subsidence trends with a simple quadratic model of fire response:

$$R_{fire}(t) = a_1 e^{b_1 t} + c_1 \tag{4.2}$$

where R_{fire} [cm yr^{-1}] is fire response subsidence trend, and a_1, b_1, and c_1 are empirical coefficients. Integrating Equation 4.2 gives the subsidence response associated with R_{fire}:

$$D_{fire}(t) = \int_0^t R_{fire}(\tau)d\tau = \int_0^t (a_1 e^{b_1 \tau} + c_1)d\tau \tag{4.3}$$

where D_{fire} [cm] is the fire response subsidence associated with the D_{fire}. Similarly, we estimate the fire response of seasonal subsidence with a nonlinear least-squares fit to a model of the form:

$$E_{fire}(t) = a_2 e^{b_2 t} + c_2 t + d_2 \tag{4.4}$$

where E_{fire} [cm] is the fire response in seasonal subsidence, and a_2, b_2, c_2, and d_2 are empirical coefficients that determine the quadratic response of the seasonal subsidence as a function of time. This function corresponds to the integral of the subsidence trend model in Equation 4.3 so that we can compare E_{fire} and D_{fire}. Because E only correlates with recent burns, we fit Equation 4.5 to fire burns from 1991-2007, as the seasonal subsidence of older fires is statistically indistinguishable from unburned permafrost (see results). For both response functions, we calculate the 2-norm of the residuals from the least-squares solution, the 2-norm of the data uncertainty, and treat these two error sources as dependent uncertainties.

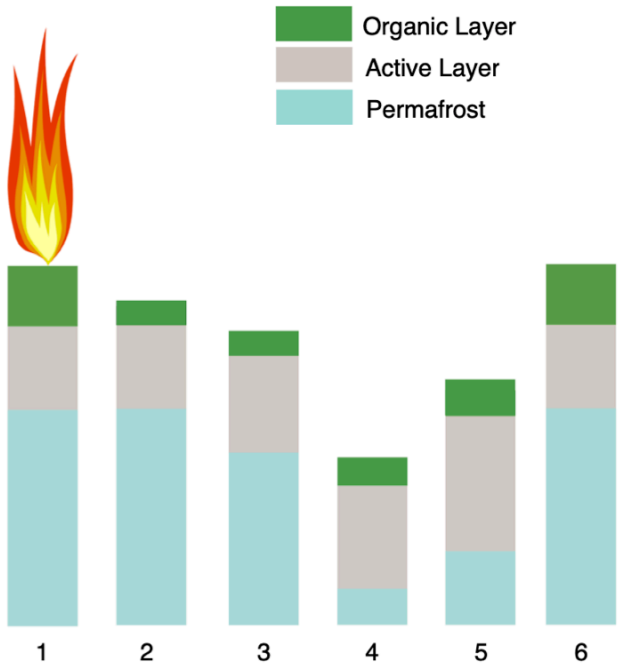

Figure 4.2: A schematic of fire response in permafrost [Shur and Jorgenson, 2007]. (1) Fire removes vegetation and part of the surface organic layer. (2) The removal of the insulating organic layer and change in albedo surface increases energy into the soil. (3) The ALT increases over several years. (4) ALT reaches a maximum. (5) The organic layer gradually thickens as a result of vegetation growth and the ALT decreases. (6) The permafrost system returns to pre-fire conditions.

4.2.3 Field Validation and Calibration

We validate the ReSALT estimates of ALT with field measurements from a 2016 summer field campaign. The standard technique for measuring ALT in the field is by mechanical probing of the active layer [Parsekian et al., 2012]. In addition, we employ field geophysical instruments such as ground-penetrating radars (GPRs) to image the permafrost table, which exhibits a sharp discontinuity in dielectric constant [Pilon et al., 1985; Chen et al., 2016]. We collected probing measurements and GPR transects in late August based out of 6 sites within the study region (Figure 4.1). From these sites, we sampled 2006 and 2007 burn scars and unburned tundra by dragging the GPR along the tundra surface [Schaefer et al., 2015]. A total of 24 km of GPR transect data was collected, encompassing approximately 12 km of data over burned and unburned tundra each. We made contemporaneous calibration probing measurements to estimate radar velocities, from which the ALT can be directly estimated from the two-way travel time of the radar. For calibration of ReSALT, we chose field measurements made in areas unaffected by wildfire, under the assumption that these unburned regions appear stable over the time period of interest. To assess the agreement between the ReSALT and GPR ALT values, we average all GPR traces within a single ReSALT pixel, and compare the absolute value difference between the GPR and ReSALT measurements using the χ^2 statistic [Schaefer et al., 2015]:

$$\chi^2 = (\frac{ALT_{ReSALT} - ALT_{GPR}}{\epsilon_{GPR}})^2 \tag{4.5}$$

where ALT_{GPR} is the in-situ ALT measured by GPR, ALT_{ReSALT} is the ReSALT-estimated ALT, and ϵGPR is the uncertainty in ALT_{GPR}. An ideal match occurs when $\chi^2 < 1$, indicating ReSALT and GPR values agree within uncertainty and are statistically identical. A good match occurs when the uncertainty bars overlap ($1 < \chi^2 < 2$). A poor match occurs when the uncertainty bars do not overlap ($\chi^2 > 2$). Variation within these categories has no physical meaning: a χ^2 of 0.5 is not 'better' than 0.9, since both are statistically identical.

4.3 Relationship between ALT and Wildfire

ReSALT measurements reveal a complex history of the effects of wildfires on permafrost and active layer dynamics. Fire zones appear as spatial anomalies in subsidence trends that are statistically significantly different from the surrounding, undisturbed tundra with low or uniform subsidence trends (Figure 4.3a). Recent fires exhibit large positive subsidence trends corresponding to subsidence while older fires exhibit negative subsidence trends corresponding to uplift. This pattern appears consistent with a post-fire phase of permafrost degradation and thinning, followed by a more gradual recovery phase. The spatiotemporal correlation of the subsidence trends with wildfire scars suggests

that the transitory effect of wildfire on permafrost can induce thinning of permafrost for decades after the fire, and that we can measure this signal with ReSALT. The subsidence trends within fire scars compare favorably to rates of permafrost degradation estimated by Schur and Jorgenson in a disturbed ecosystem-driven permafrost system [Shur and Jorgenson, 2007]. Additionally, the response appears consistent with modeling efforts to understand the effect of wildfire on permafrost in lowland boreal forests [41]. Subsidence trends for an ecosystem-driven permafrost region in thermal equilibrium are expected to be small [Shur and Jorgenson, 2007].

The seasonal subsidence shows a characteristic pattern corresponding to raised peat plateaus and separated by thermokarst gullies (Figure 4.3c). In general, the gullies have larger seasonal subsidence than the peat plateaus due to higher water content. The peat plateaus appeared uniformly flat and raised above the gullies by about three meters. The thickness of permafrost in the YK delta was previously estimated to be 10m under 1m peat plateaus, assuming a soil column of water ice [Jorgenson and Ely, 2001]. We observed peat plateaus ranging from $1 - 3$ m in height, which is consistent with soil expansion of 25-74 m of permafrost (Equation 3.22, $P = 0.45$ for a typical silty soil). However, we typically could not detect the permafrost table with the metal probes or GPR within the gullies indicating no permafrost at all or the presence of a thick layer of unfrozen soil known as a talik. Essentially, we see permafrost under the peat plateaus and no permafrost in the gullies. ReSALT readily detects seasonal subsidence due to active layer thaw over permafrost on the plateaus and due to freezing of surface soils in non-permafrost soils in the gullies.

Like in R, the fire scars also appear as spatial anomalies in seasonal subsidence. The most recent fires show large, statistically significant differences with the surrounding, undisturbed tundra (see Figures 4.8, 4.9, 4.10). However, the oldest fires show seasonal subsidence statistically identical to their unburned surroundings. This suggests wildfire has a more transient effect on seasonal subsidence than subsidence trends.

ALT shows the same mottled pattern as the seasonal subsidence, with larger values in the gullies and smaller values on the plateaus (Figure 4.3c). However, our field measurements indicate no permafrost in the gullies. What ReSALT measures as ALT in the gullies actually represents the thickness of the seasonally frozen surface layer in non-permafrost soil. Like the seasonal subsidence, we see statistically significant spatial anomalies in the more recent fires, but not for the oldest fires, suggesting ALT recovers from wildfires quicker than subsidence trends.

Comparison of ReSALT and GPR measurements of ALT yields ideal matches for 53% of the data and good matches for 13% of the data (Figure 4.4). An ideal match indicates the ReSALT and GPR values are statistically identical and a good match indicates the uncertainty bars overlap. ReSALT and GPR agree in the unburned tundra, but not in the 2007 fire zones. The ALOS data starts immediately after the 2007 fire so that the interferogram stack reflects the pre-recovery stage of the fire response model (steps 1-3 of Figure 4.2) [14]. We made the GPR measurements in 2016, nine years after fire and reflecting the last stages of fire recovery of the active layer. The ReSALT

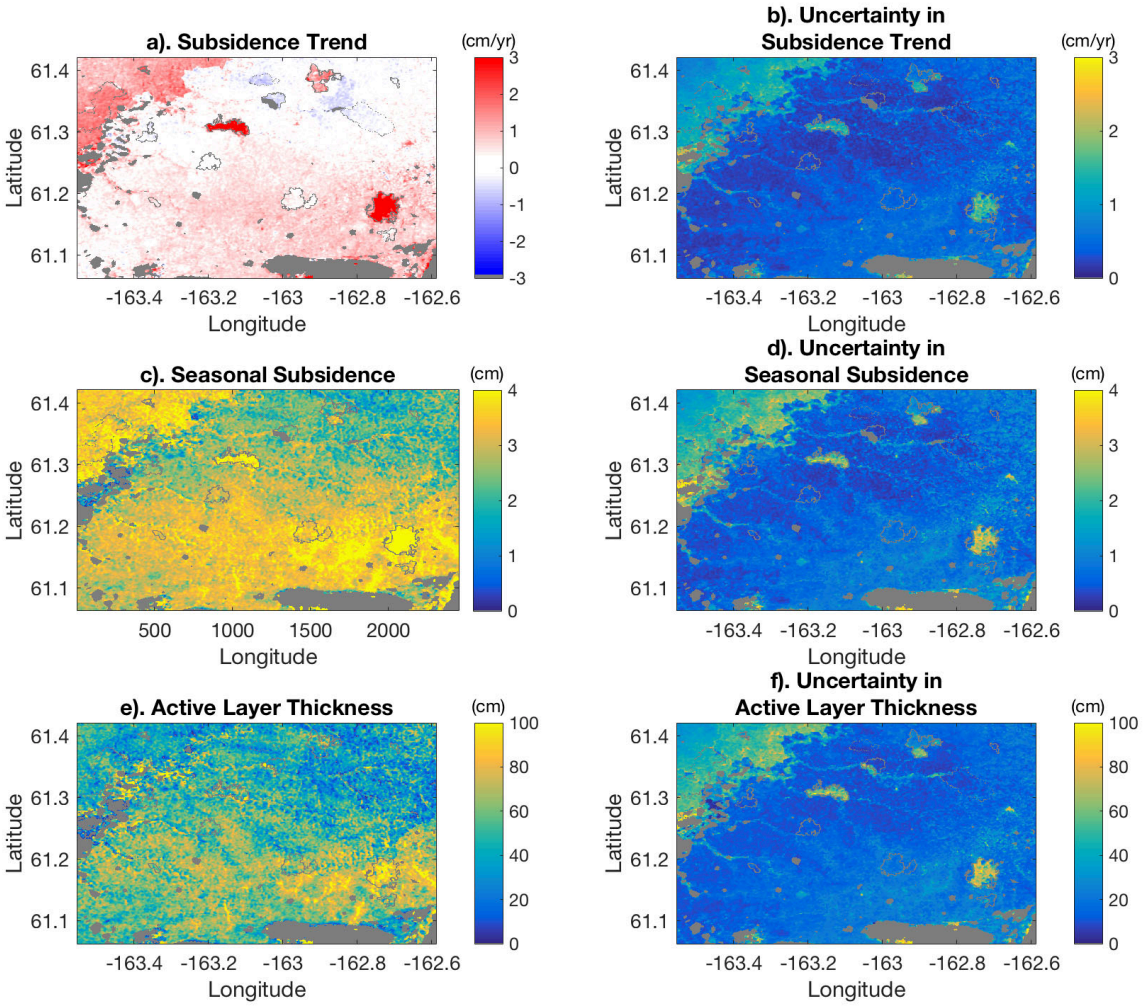

Figure 4.3: Results from application of the ReSALT algorithm to the YK study region. (a) ReSALT-derived long-term subsidence trend, positive values correspond to an increase in thaw depth (cm/yr). (b) Uncertainties in long-term trends. (c) ReSALT-derived average seasonal subsidence from 2007-2010 [cm yr^{-1}]. (d) Uncertainties in seasonal subsidence. (e) ReSALT-derived ALT (cm). (f) Uncertainties in ALT (cm). Of particular note are the large positive trends in recent burn areas from the 2000's, and negative trends in regions that were burned in the 1970's. Wildfires are outlined in gray, and a red box surrounds the fire scar discussed in Figure 4.4.

ALT shows a positive bias relative to GPR values in the 2007 fire zone, consistent with nine years of recovery after the fire.

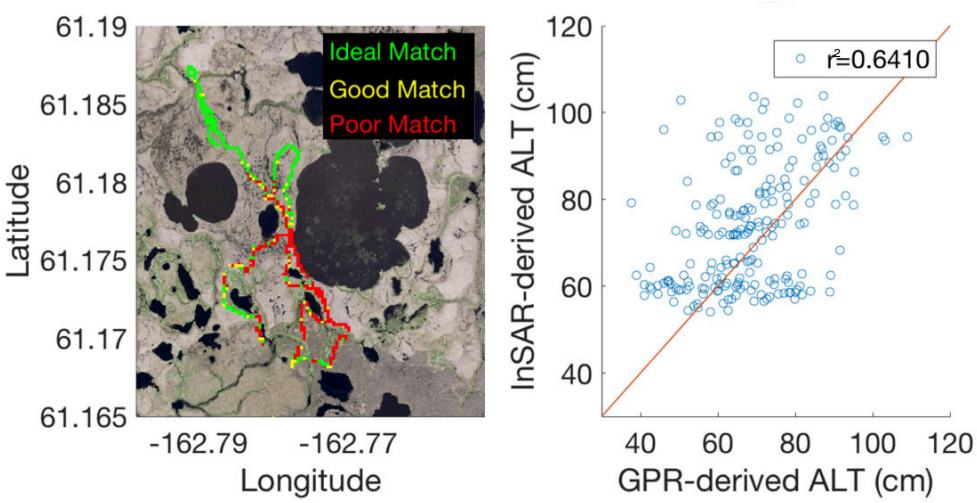

Figure 4.4: Comparison between GPR and InSAR estimates of ALT at site 5. Left: Total path of GPR, color-coded based upon the result of the χ^2 test. Right: Correlation between the GPR and InSAR estimates of ALT, r=0.6410. Both techniques capture fine spatial variability of ALT and yield mutually consistent results in unburned tundra, while there is little agreement in the region affected by the 2006 fire (bottom half of the survey).

The incorporation of scenes from either outside the thaw season, or in the uplift season may necessitate a more physically realistic model of seasonal subsidence than the one used in this work, as noted in [Chen et al., 2020]. Recently, Hu et al. introduced a composite index that encapsulates both the thaw subsidence and freeze uplift of permafrost, and demonstrated agreement with GPS reflectometry data [Yufeng et al., 2018]. Modifying the ReSALT algorithm to consider both freezing and thawing indices is the subject of ongoing work. Additionally, large seasonal variations in volumetric water content and saturation can be falsely interpreted as deformation signals [Zwieback et al., 2015a]. Incorporation of independent observations of soil moisture into the ReSALT algorithm is an important piece of ongoing work, as the ReSALT algorithm does not currently take into consideration spatial or temporal variability of volumetric water content. In general, the use of more interferograms leads to more robust solutions with the ReSALT algorithm. The launch of the NISAR mission in 2021 will allow for the collection of L-band ($\lambda \approx 23$ cm) SAR imagery suitable for InSAR at 6-12 day repeat intervals–a significant improvement to the repeat interval of the ALOS satellite. This will allow for more accurate characterization of the seasonal subsidence and subsidence trends of permafrost regions.

Our fire response models indicate seasonal subsidence and ALT recover much faster than subsidence trends after a fire (Figure 4.6). The seasonal subsidence response appears consistent with a

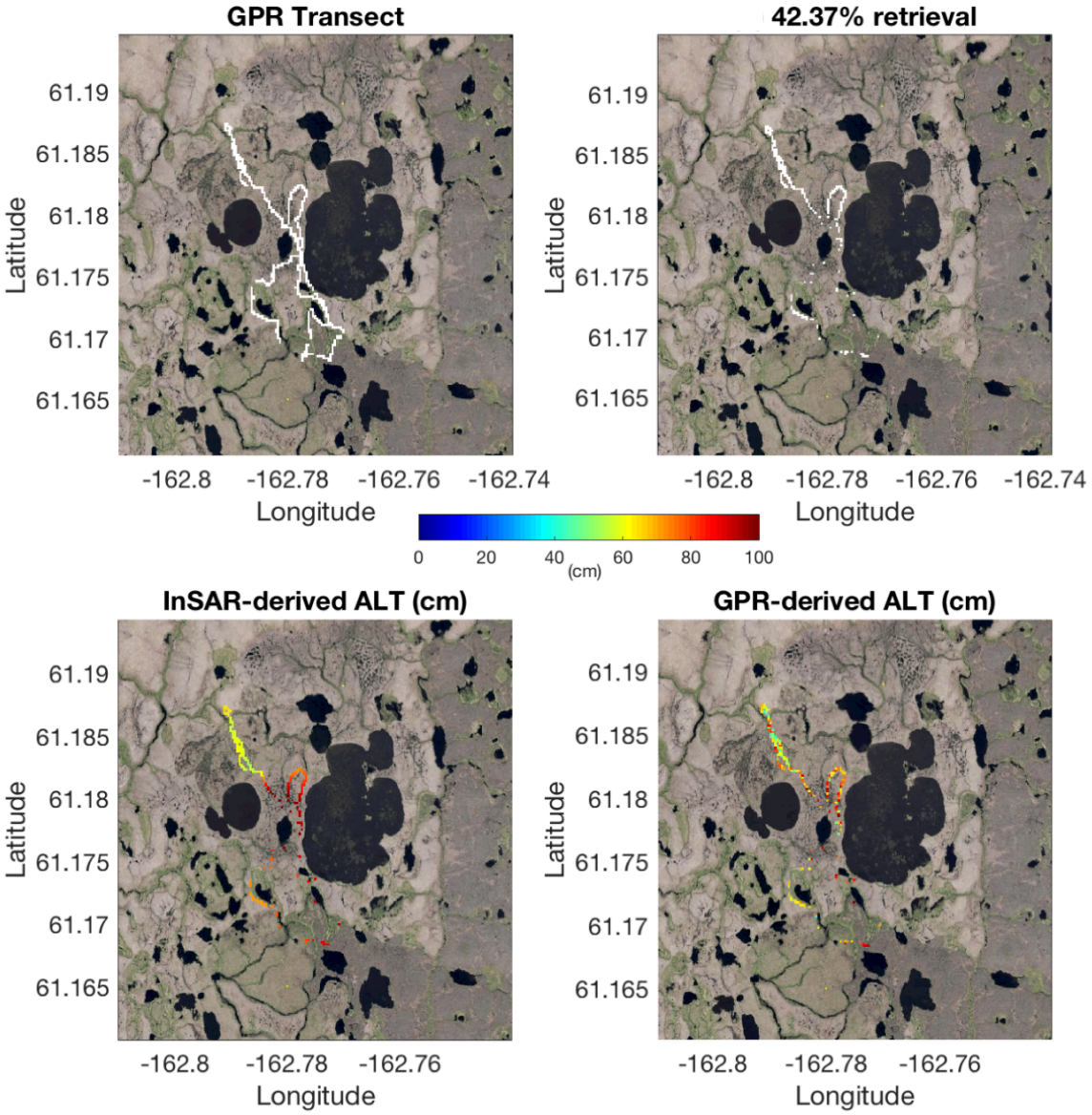

Figure 4.5: Comparison between GPR and InSAR estimates of ALT at site 5. Top left: Total path of GPR colored in white. Top right: Percentage of data for which ideal or good matches are obtained between the GPR and InSAR estimates of ALT. Bottom left: InSAR-derived ALT. Bottom right: GPR-derived ALT.

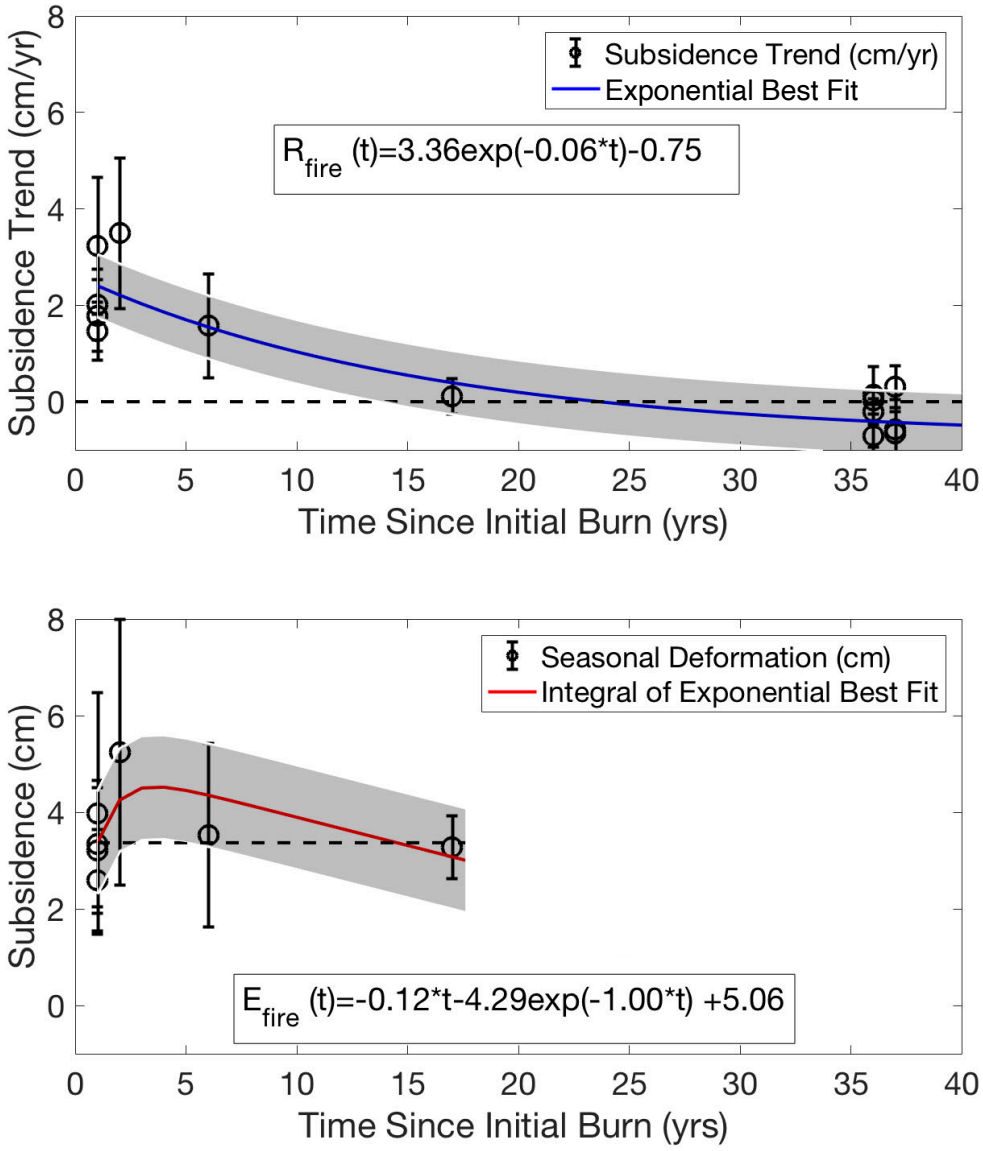

Figure 4.6: Top: Exponential best fit to subsidence trends, exhibiting an increase in permafrost thinning for the first two decades after fire, followed by a more gradual thickening as the permafrost slowly reforms. Dotted line represents 0 subsidence trend; the intersection of the subsidence trend with the 0 trend line corresponds to the beginning of permafrost recovery. Bottom: Integral-Exponential best fit to seasonal subsidence, exhibiting an increase in seasonal thaw depth for the first decade after fire, and a total recovery of approximately 16 years. Dotted line corresponds to a pre-fire seasonal subsidence of 3 cm.

previous study of post-fire active layer dynamics in the Canadian tundra [Mackay, 1995]. Immediately after a fire, the seasonal subsidence experiences a gradual increase for approximately a decade reflecting deeper seasonal thaw depths. The seasonal subsidence then reverses sign as the organic layer gradually re-accumulates and the thaw depth decreases [Mackay, 1995; Shur and Jorgenson, 2007; Rocha et al., 2012]. After 15 years, the seasonal subsidence returns to its pre-fire thermal equilibrium. As expected, ALT reflects seasonal subsidence and returns to pre-fire values after 15 years (not shown). In contrast, subsidence trends show a much longer response, changing from positive to negative at 25 years, indicating a change from subsidence to heave, and eventually returning to zero after 65-70 years.

4.4 Implications for Wildfire Recovery in Discontinuous Permafrost Environments

ReSALT measures two separate, but related responses to fire: active layer thickening and permafrost thinning (Figure 4.7). The integral of the subsidence trend response model (Equation 4.4) represents the impact of fire on permafrost thickness. The seasonal subsidence response model represents the impact of fire on the thickness of the active layer. The removal of vegetation and organic material by fire increases energy absorption by the ground, which will increase ALT, seasonal subsidence, and the permafrost temperature. The thickness of permafrost balances freezing from the surface and warming from the Earth's interior, so any increase in permafrost temperature would result in a thinning of the permafrost layer.

Both fire response models show two distinct phases: a perturbation phase and a recovery phase. Both response curves start at zero, which represents pre-fire thermal equilibrium conditions. In the perturbation phase, the subsidence increases from zero to a maximum value. In the recovery phase, the subsidence slowly decreases back to zero or pre-fire conditions. Both response models show a recovery phase approximately twice as long as the perturbation phase.

Fire increases the thickness of the active layer, resulting in an increase in seasonal subsidence. The perturbation phases lasts $\approx$5 years and peaks at 1.7 cm, which, using our soil expansion model, corresponds to a 26 cm increase in ALT. The ALT response model shows consistent results (not shown). The vegetation grows back quickly, eliminating the albedo effect and stopping the increase in ALT after $\approx$5 years. This appears consistent with the rapid post-fire vegetation regrowth associated with tundra fires [Viereck and Schandelmeier, 1980]. In the recovery phase, which lasts $\approx$10 years, the vegetation and organic layer thicken, insulating the soil and decreasing ALT and seasonal subsidence. After 15 ± 7 years, the organic layer returns to per-fire conditions, along with ALT and seasonal subsidence.

Fire raises the temperature of the permafrost layer, thinning the permafrost layer and inducing permafrost thaw [Rocha et al., 2012]. A warm temperature anomaly introduced at the surface takes

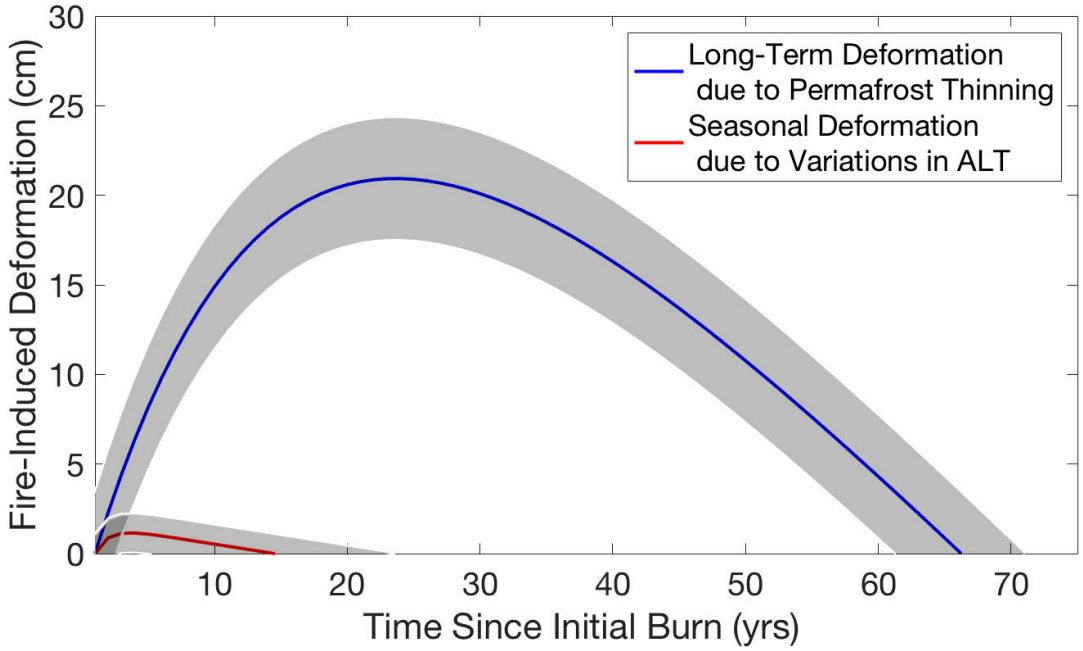

Figure 4.7: Comparison of the best fitting seasonal subsidence (Equation 4.2; red) and the integrated subsidence trend (Equation 4.4; blue) induced by wildfire, with their associated uncertainties in grey. These deformations are associated with, respectively, variations in the seasonal thaw depth of the active layer, and thinning of permafrost. These two processes occur over 15 ± 7 years, and 66 ± 5 years, respectively.

years to propagate downward throughout the soil column [Schaefer et al., 2009]. The subsidence response model peaks at 20 cm about 25 years after a fire. If we assume this subsidence is describable entirely by the soil physics model we have employed, for an initial permafrost thickness of 25 m of saturated silty soil with a porosity of 45% (consistent with an ice-rich permafrost column), 20 cm of subsidence corresponds to a thinning of the permafrost by ≈5 m, or 20%. Such subsidence cannot result from increases in active layer thaw depth, which would correspond to an increase in ALT of ≈5 m, which we do not observe. Some of this subsidence may be due to soil compaction, for which our soil physics model does not account. These estimates of permafrost thinning thus represent an upper bound estimate, as porosity is at the upper limit of silty soils.

The permafrost thinning response depends on the seasonal subsidence response, but takes approximately five times longer. The seasonal subsidence and ALT response depends on energy balance in the summer, but the permafrost thinning depends on annual energy balance. The permafrost thinning cannot peak until the seasonal subsidence and ALT peak, but lags due to the time required to propagate temperature anomalies. As a result, seasonal subsidence and ALT peak after 5 years, but permafrost thinning peaks after 25 years. Seasonal subsidence and ALT return to pre-fire conditions after 15 ± 7 years, but permafrost thickness returns to pre-fire conditions after 66 ± 5 years.

Our results emphasize the importance of ecological processes in controlling permafrost dynamics, where local vegetation plays a significant role in the thermal insulation of permafrost and the post-fire response [Shur and Jorgenson, 2007]. Removal of surface vegetation and a fraction of the overlying organic layer of the active layer by wildfire modifies the thermal insulation and albedo of the surface, making permafrost susceptible to a deeper seasonal thaw depth. In areas with a thick organic layer, poor drainage and fine-grained soil, the permafrost system can eventually return to its pre-fire equilibrium state, or reach a new thermal equilibrium [Viereck and Schandelmeier, 1980]. This response is driven by the gradual re-accumulation of an organic layer as a by-product of the ecological regrowth of the surface vegetation, which insulates the permafrost and gradually decreases the seasonal thaw depth of the active layer [Shur and Jorgenson, 2007]. Simultaneously, wildfires induce a thinning of permafrost; the recovery time scales between active layer and permafrost differ by almost a factor of five, and thickening of the permafrost is first contingent upon the total recovery of the active layer. Post-fire active layer dynamics differ in dissimilar permafrost regimes, such as black spruce forests, where fire can initiate irreversible permafrost degradation [Shur and Jorgenson, 2007; Jafarov et al., 2013]. However, we demonstrate that ReSALT can successfully infer and discriminate between post-fire permafrost and active layer dynamics of permafrost. In the future, this technique should be extended to other regions under different permafrost and climatic regimes to further constrain post-fire permafrost active layer dynamics as a function of permafrost regime and fire severity.

4.5 Summary

In this chapter, we demonstrated that fire in the YK Delta increases seasonal subsidence and ALT while simultaneously thinning the permafrost layer. We successfully applied the ReSALT algorithm to the YK Delta to estimate seasonal subsidence, subsidence trends, ALT, and uncertainties. ALT ranges from 10-120 cm, and correlates with surface geomorphology. We compared the ReSALT and GPR measurements of ALT agree for 68% of the pixels, with higher agreement in undisturbed tundra than in fire zones. Using burn scars and fire ages, we constructed fire response models. Seasonal subsidence and ALT response to fire peaks at 5 years and returns to pre-fire conditions after 15 ± 7 years. The peak seasonal subsidence response is 1.7 cm corresponding to an increase in ALT of 26 cm. The permafrost thins in response to fire, with a peak at 25 years and a recovery to pre-fire conditions after 66 ± 5 years. The peak subsidence associated with permafrost thinning was 20 cm, corresponding to a thinning of the permafrost layer by 5 meters. In the next chapter, we will address the issue of InSAR decorrelation, its relationship to soil moisture, and geodetic errors associated with it.

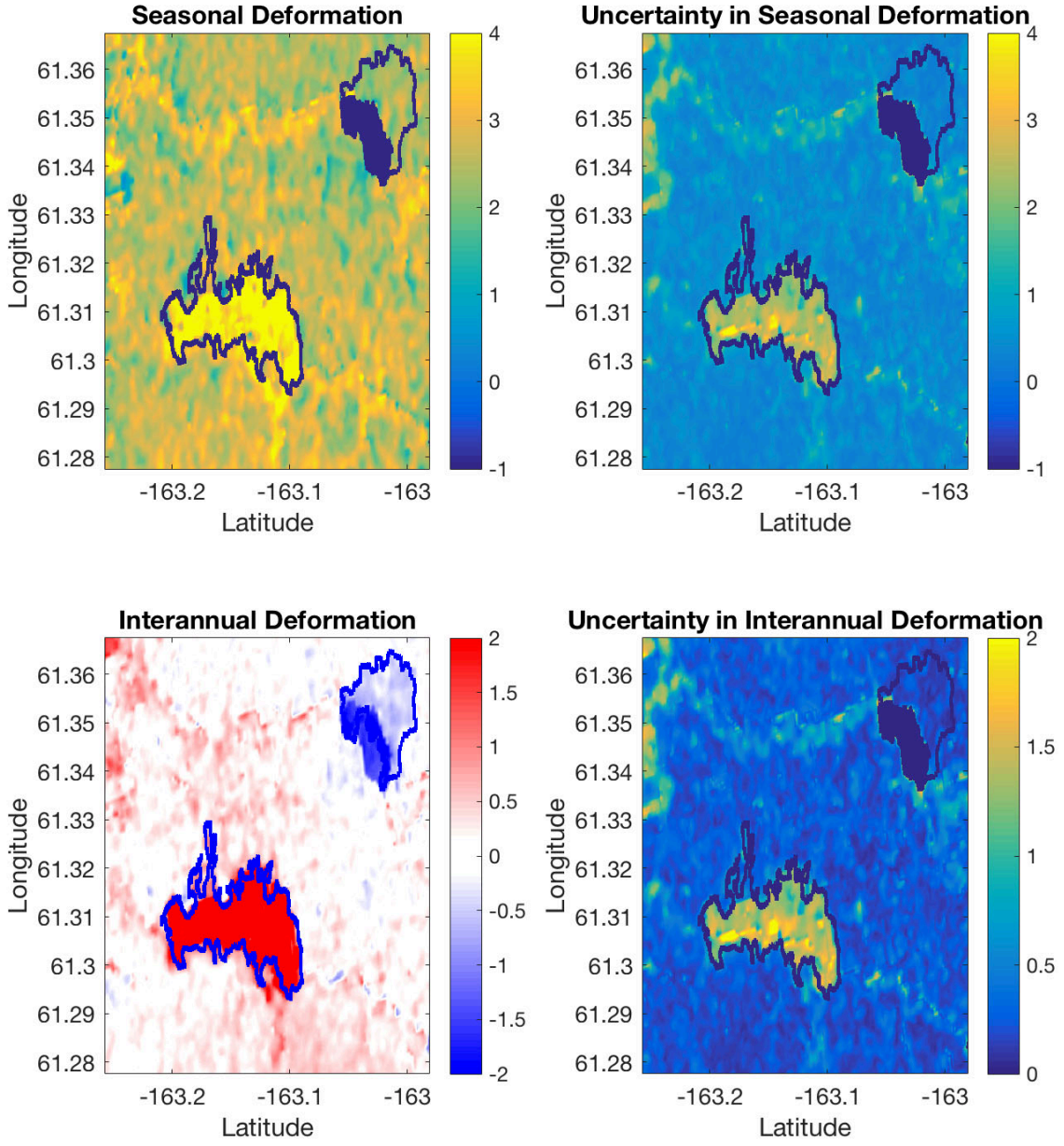

Figure 4.8: Seasonal deformation (top row) and interannual deformation (bottom row) for a 2007 fire (bottom left fire) and 1972 fire (top right fire).

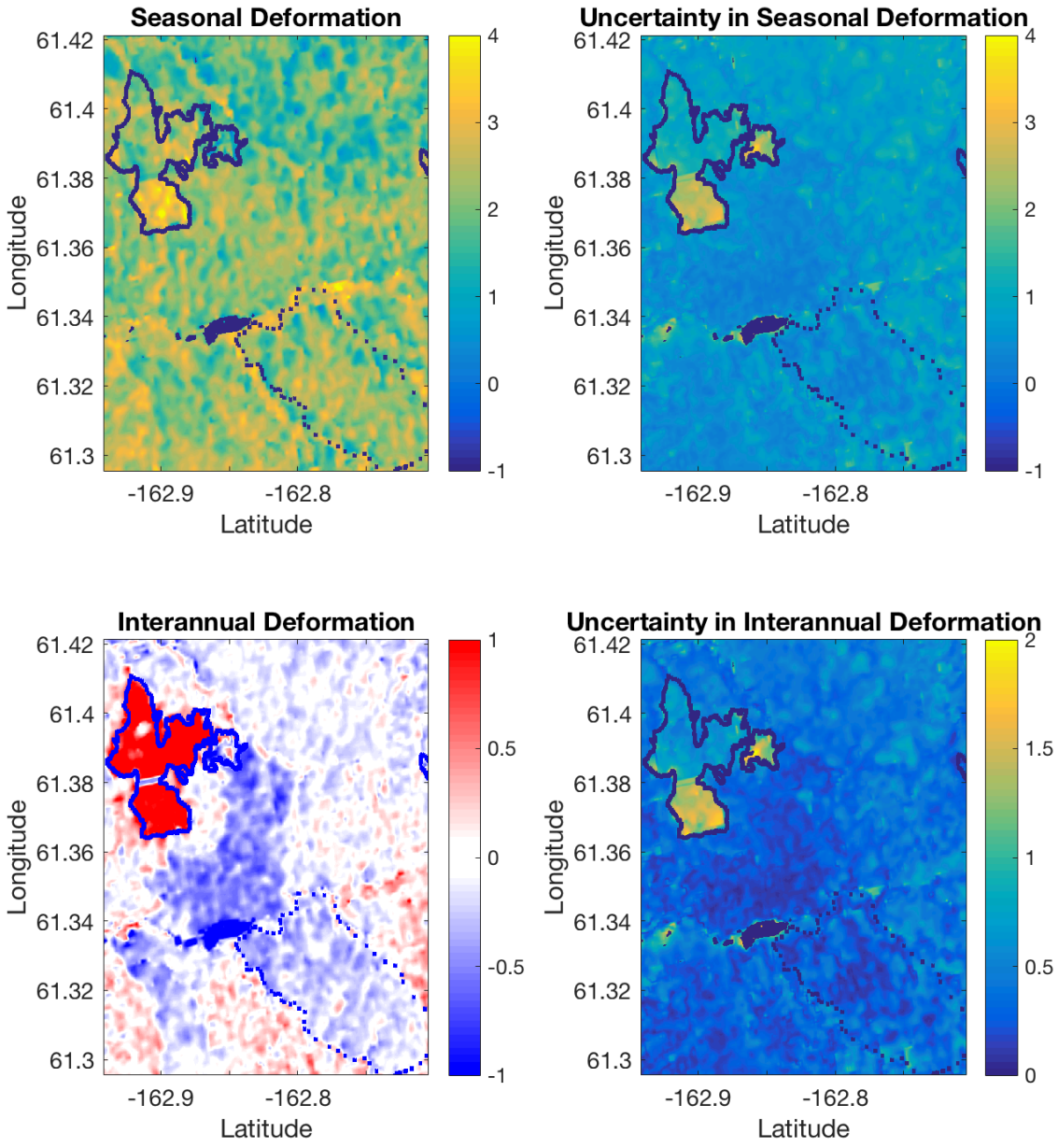

Figure 4.9: Seasonal deformation (top row) and interannual deformation (bottom row) for a 2007 fire (top left fire) and 1971 fire (bottom right fire).

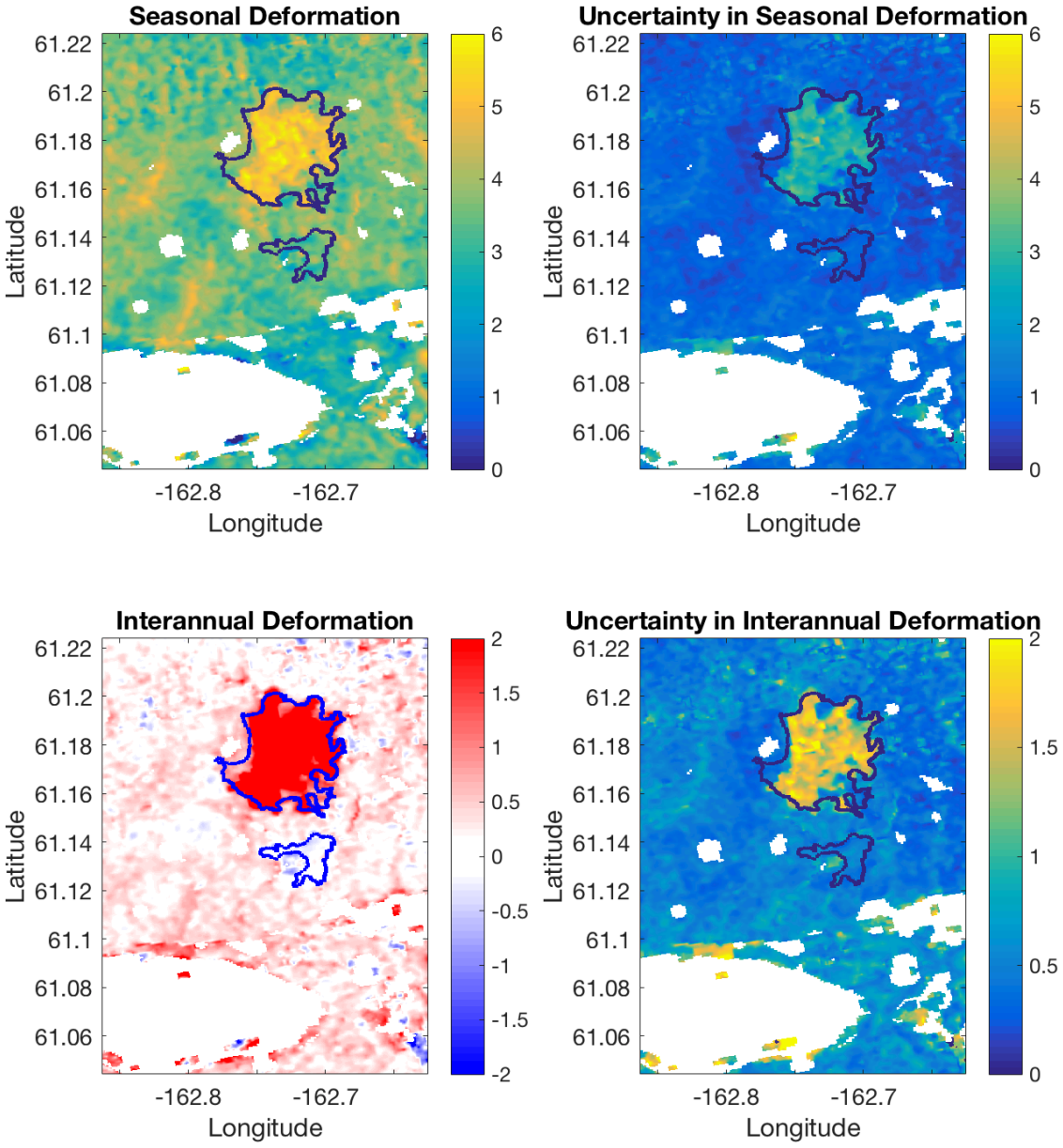

Figure 4.10: Seasonal deformation (top row) and interannual deformation (bottom row) for a 2006 fire (top fire) and 1972 fire (bottom fire).

Chapter 5

Decorrelation Phase from Closure Phase

In this chapter, we present a novel method for quantifying and correcting phase errors in interferometric synthetic aperture radar (InSAR) data associated with signal decorrelation. Our method relates the observed phase nonclosure (referred to as closure phase) of triplet combinations of any three individual SAR scenes to the decorrelative phase signal in individual interferograms (pairs of SAR scenes). We apply a singular value decomposition (SVD) method to solve for the minimum-norm least-squares best fitting estimate of decorrelation phase for any arbitrary collection of SAR images. We then remove this decorrelative phase from individual interferograms; these corrected interferograms can then be used with existing InSAR time-series analysis algorithms. We demonstrate this method on ALOS PALSAR scenes of a groundwater pumping subsidence feature in the Central Valley of California, and briefly discuss potential future applications of this algorithm to study a variety of environmental and surface physical processes that contribute to InSAR signal decorrelation.

5.1 Relationship between Closure Phase and Decorrelation Phase

Interferometric synthetic aperture radar (InSAR) is a well-established technique of measuring millimeter to centimeter scale surface deformation at fine spatial resolution [Rosen et al., 2000]. Spaceborne InSAR missions, such as Sentinel-1A/B, the ALOS PALSAR satellite, and the upcoming NISAR mission, provide long time-series of observations of the Earth at a global scale with repeat times on the order of several days. Conventionally, a series of SAR single look complex (SLC) images are acquired over a region of interest, from which any possible pair of SLCs can be cross-multiplied

with respect to each other to form a complex correlation. As derived in Section 3.4, the complex correlation $\tilde{\gamma}$ is defined as:

$$\tilde{\gamma} = \frac{\langle s_1 s_2^* \rangle}{\sqrt{\langle s_1 s_1^* \rangle \langle s_2 s_2^* \rangle}} \tag{5.1}$$

For clarity of the following derivation, we express the interferometric phases in their more familiar unwrapped notation, while reminding readers that actual implementation of the algorithm is conducted rigorously by treating all phases as the (wrapped) argument of complex products and conjugates. In scenarios where decorrelation phase is significant, phase unwrapping errors can introduce 2π phase ambiguities to the following equations. This phenomenon is more thoroughly discussed in Section 5.3.2.

For a given image pixel, the resulting interferometric phase is directly related to the change in range between the sensor location and the illuminated ground target:

$$\phi_{12} = \phi_2 - \phi_1 = -\frac{4\pi}{\lambda}(r_2 - r_1) + \phi_{...} \tag{5.2}$$

where ϕ_{12} is the interferometric phase, ϕ_1 and ϕ_2 are the phases associated with scenes 1 and 2, respectively, r_1 and r_2 are the ranges from the sensor to the target for scenes *1* and *2*, respectively, λ is the radar wavelength, and $\phi_{...}$ represents additional phase terms (e.g. atmospheric phase screen, topographic error phase, decorrelation phase).

Recall from Section 3.7 that for any triplet of three SAR images, the bicoherence $\tilde{\Xi}$ is defined as the product of two complex coherences multiplied by the complex conjugate of the third [Zwieback et al., 2015b]:

$$\tilde{\Xi}_{123} = \tilde{\gamma}_{12}\tilde{\gamma}_{23}\tilde{\gamma}_{13}^* \tag{5.3}$$

The closure phase ξ_{123} is simply the argument of the bicoherence $\xi = \angle\tilde{\Xi}_{123}$, and is therefore a linear combination of the three interferometric phases:

$$\xi_{123} = \phi_{12} + \phi_{23} - \phi_{13} \tag{5.4}$$

As discussed in Section 3.7, closure phase is totally insensitive to propagational phase (i.e. surface deformation, atmospheric phase screen, topographic error terms); the components of the interferometric phase that are directly related to deformation of the ground's surface will always sum

identically to zero for simple piston-like deformation [Zwieback et al., 2016]. To see this, we can express the interferometric phase of an interferogram as:

$$\phi^{int} = \phi^{p} + \phi^{d} + \phi^{n} \tag{5.5}$$

where ϕ^{int} is the total interferometric phase, ϕ^{p} is the propagative component of interferometric phase associated with ground deformation, topography, and atmospheric phase screens, ϕ^{d} is the decorrelative component of interferometric phase introduced from temporal decorrelation, and ϕ^{n} is a zero-mean Gaussian additive noise term due to thermal noise. The decorrelative component is due to temporally varying electrical and scattering properties of the surface; in most InSAR time-series algorithms, ϕ^{d} is neglected, or folded into the additive noise term [Nolan and Fatland, 2003; Nolan et al., 2003; Nesti et al., 1995]. However, temporal decorrelation is correlated across SAR scenes and is not a simple additive noise term [Agram and Simons, 2015]. With the definition of the interferometric phase in Equation 5.5, we can express the closure phase for any 3 SAR scenes as:

$$\begin{aligned}
\xi_{123} &= \phi_{12} + \phi_{23} - \phi_{13} \\
\xi_{123} &= \phi^{p}_{12} + \phi^{d}_{12} + \phi^{p}_{23} + \phi^{d}_{23} - \phi^{p}_{13} - \phi^{d}_{13} + \phi^{n}_{N} \\
\xi_{123} &= -\frac{4\pi}{\lambda}(\phi_2 - \phi_1) + \phi^{d}_{12} - \frac{4\pi}{\lambda}(\phi_3 - \phi_2) + \phi^{d}_{23} + \dots \\
&\quad + \frac{4\pi}{\lambda}(\phi_3 - \phi_1) - \phi^{d}_{13} + \phi^{n}_{N}
\end{aligned} \tag{5.6}$$

where ϕ^{n}_{N} is a combined additive noise term for the three scenes. For simple piston-like deformation, the propagative phase terms cancel, and Equation 5.6 simplifies to:

$$\xi_{123} = \phi^{d}_{12} + \phi^{d}_{23} - \phi^{d}_{13} + \phi^{n}_{N} \tag{5.7}$$

For single look interferograms, where no spatial averaging (multilooking) is applied during phase estimation, Equation 5.7 will always evaluate identically to zero [Samiei-Esfahany et al., 2016]. Similarly, for a perfectly coherent surface with time invariant scattering and electrical properties, the total closure phase will always sum to zero. Signal decorrelation, and multilooking during coherence estimation introduces non-zero closure phase [Agram and Simons, 2015]; because nonzero closure phase is fundamentally a product of signal decorrelation, it is directly related to variations in the scattering and electrical properties of the ground surface.

Because closure phase is directly related to decorrelation phase, and totally insensitive to propagative phase terms, closure phase can be exploited to reduce interferogram phase errors, and improve InSAR time series analysis and deformation monitoring. In Section 5.2, we present an efficient

algorithm that resembles the popular SBAS algorithm [Berardino et al., 2002], which can be implemented to solve for the best fitting set of decorrelation phases for a given stack of interferograms and their associated phase triplets. In Section 5.3, we demonstrate this algorithm by applying it to a set of ALOS PALSAR data collected over a subsidence feature in California's Central Valley associated with agricultural groundwater pumping. We discuss the results of the algorithm, and its potential for reducing phase errors and improving deformation monitoring [Zwieback et al., 2017]. In Section 5.4 we discuss future refinements that can be made to the algorithm, comment on its potential applicability to the study of a range of physical properties and environmental parameters that contribute to InSAR signal decorrelation, and provide concluding remarks.

5.2 Algorithm Formulation

Consider a series of N focused SAR images that have been coregistered to the same geographic region of interest, indexed by their relative order of acquisition. The total number of possible interferograms M that can be formed from these N images satisfies the following inequality from [Berardino et al., 2002]:

$$\frac{N}{2} \leq M \leq \frac{N(N-1)}{2} \tag{5.8}$$

In the SBAS technique, the number of interferograms M will depend upon the number of small baseline (SB) subsets of interferograms in the inversion, which is determined by the chosen spatial and temporal baselines. The total number of possible closure phase triplets K that can be formed by N images satisfies the following inequality:

$$\frac{N}{3} \leq K \leq \frac{N(N-1)(N-2)}{6} \tag{5.9}$$

Similarly, the number of triplet subsets in the inversion will depend upon the chosen spatial and temporal baselines. For any coregistered pixel, we can express the k^{th} closure phase ξ_k as a function of the associated interferometric phases:

$$\begin{aligned} \xi_k &= \phi_{k_1} + \phi_{k_2} - \phi_{k_3} \\ \xi_k &= \phi^p_{k_1} + \phi^d_{k_1} + \phi^p_{k_2} + \phi^d_{k_2} - \phi^p_{k_3} - \phi^d_{k_3} + \phi^n_N \end{aligned} \tag{5.10}$$

where ϕ_{k_1}, ϕ_{k_2}, and ϕ_{k_3} are the three interferograms associated with the k^{th} closure phase ξ_k, and ϕ^n_N is a combined additive noise term for the three scenes. For simple piston-like deformation, Equation

5.10 simplifies to:

$$\xi_k = \phi^d_{k_1} + \phi^d_{k_2} - \phi^d_{k_3} + \phi^n_N \tag{5.11}$$

Equation 5.11 defines a system of K equations with M unknowns, which can be expressed as:

$$\xi = B\phi^d \tag{5.12}$$

where ξ is a [K x 1] vector of closure phases, ϕ^d is an [M x 1] vector of decorrelation phase, and B is a [K x M] matrix whose elements are either 0 or ± 1. In general, B will be rank deficient; While N SAR images can form $\binom{N}{2}$ interferograms and $\binom{N}{3}$ closure triplets, only $N-1$ interferograms and $\binom{N-1}{2}$ triplets are independent. The rank of B is therefore $\binom{N-1}{2}$. Equation 5.12 can be solved with the SVD method as in [Berardino et al., 2002], whereby the pseudo-inverse $B^\dagger$ of B yields a minimum-norm least-squares solution for $\hat{\phi}^\xi$ of the form:

$$\hat{\phi}^d = B^\dagger \xi \tag{5.13}$$

Because wrapped interferometric phase is used both for closure phase estimation and the SVD inversion, the best fitting decorrelation phase will also be a wrapped phase. The process of unwrapping interferometric phase converts the modulo 2π wrapped phase ϕ^{int} to an unwrapped phase φ^{int} by estimating the total integer number of 2π phase cycles associated with the interferometric phase. We can express the unwrapped interferometric phase of any interferogram φ^{int} as follows:

$$\varphi^{int} = 2\pi X + \phi^{int} \tag{5.14}$$

where X is an integer, and ϕ^{int} is the wrapped interferometric phase. Similarly, we can define the unwrapped decorrelation phase φ^d as:

$$\varphi^d = 2\pi Y + \phi^d \tag{5.15}$$

where Y is an integer, and ϕ^d is the wrapped decorrelation phase. We can express the true wrapped propagative phase as:

$$\phi^p = \phi^{int} - \phi^d \tag{5.16}$$

which is equal to the true unwrapped propagative phase, modulo 2π:

$$\varphi^p = mod[(\phi^{int} - \phi^d), 2\pi] \tag{5.17}$$

The phase closure SVD algorithm provides an estimate of the wrapped decorrelation phase $\hat{\phi^d}$. We can therefore express an estimate of the unwrapped propagative phase $\hat{\varphi^p}$ as:

$$\hat{\varphi^p} = mod[(\phi^{int} - \hat{\phi^d}), 2\pi] \tag{5.18}$$

We employ several simplifying assumptions to make this problem easier to solve, although we note that in the general case these assumptions may not always be valid. First, we assume that the magnitude of the decorrelation phase is less than 2π, i.e. $Y = 0$. In this case, the estimate of the wrapped decorrelation phase $\hat{\phi^p}$ is equivalently an estimate of the unwrapped decorrelation phase, i.e. $\hat{\varphi^p} = \hat{\phi^p}$. We can rewrite Equation 5.18 as:

$$\hat{\varphi^p} = 2\pi X + (\phi^{int} - \hat{\phi^d}) \tag{5.19}$$

As long as the magnitude of the estimated wrapped decorrelation phase is much smaller than the magnitude of the wrapped interferometric phase (i.e. $|\hat{\phi^d}| \ll |\phi^{int}|$), then $\phi^{int} - \hat{\phi^d} \approx \phi^{int}$, in which case the estimate of the integer number of phase cycles in the unwrapped phase will be identical whether or not we remove the wrapped decorrelation phase estimate before phase unwrapping. If, however, $\phi^{int} - \hat{\phi^d} \neq \phi^{int}$, then removing the wrapped decorrelation phase estimate can introduce a residue into the phase unwrapping process. The introduction of residues can potentially alter the global unwrapped phase estimate from SNAPHU. Alternatively, Equations 5.12-5.13 can be reformulated to explicitly solve for the phase ambiguity via an ILS method as in [Samiei-Esfahany et al., 2016], although this technique is more computationally intensive and does not explicitly solve for decorrelation phase.

After removing the best fitting decorrelative phase from the interferometric phase, this estimate of the propagative phase can then be unwrapped and incorporated into existing InSAR time series algorithms, such as PSI and SBAS [Hooper et al., 2004; Berardino et al., 2002; Hooper, 2008]. Furthermore, the propagative phase component can be further separated into ground deformation

components and atmospheric phase screen components, for which several methods are available [Jolivet et al., 2014; Bekaert et al., 2015]. Our algorithm is represented in a block diagram form in Figure 5.1. Blue arrows correspond to standard steps in InSAR processing for time series applications, whereas the additional steps due to our algorithm are in black.

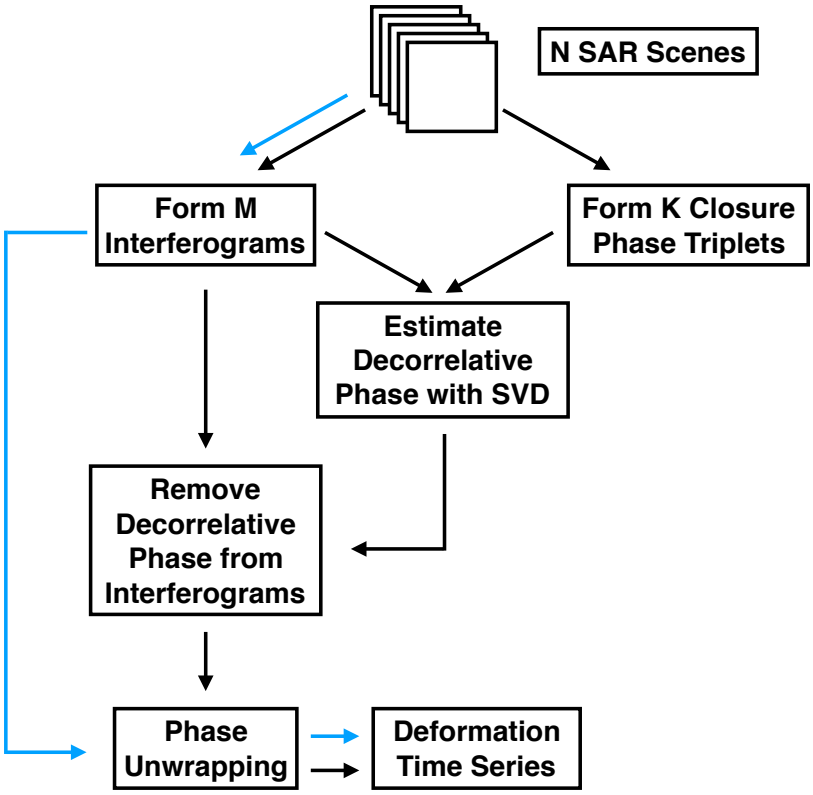

Figure 5.1: Block diagram of the presented algorithm. Arrows in blue correspond to standard steps in InSAR post-processing; arrows in black correspond to steps added as part of this algorithm.

5.3 Demonstration of Algorithm

5.3.1 ALOS dataset, California Central Valley

We applied the algorithm to a set of $N = 19$ ALOS-PALSAR SAR images acquired between 2007-01-05 and 2011-03-03 over an area of ground subsidence in the Central Valley, California associated with groundwater pumping. These SAR images are generated as in [Zebker et al., 2010], with 16 (32) looks taken in range (azimuth), and a total of $M = 171$ interferograms and $K = 969$ phase closure triplets are generated (of which 153 are independent). The best fitting phase error due

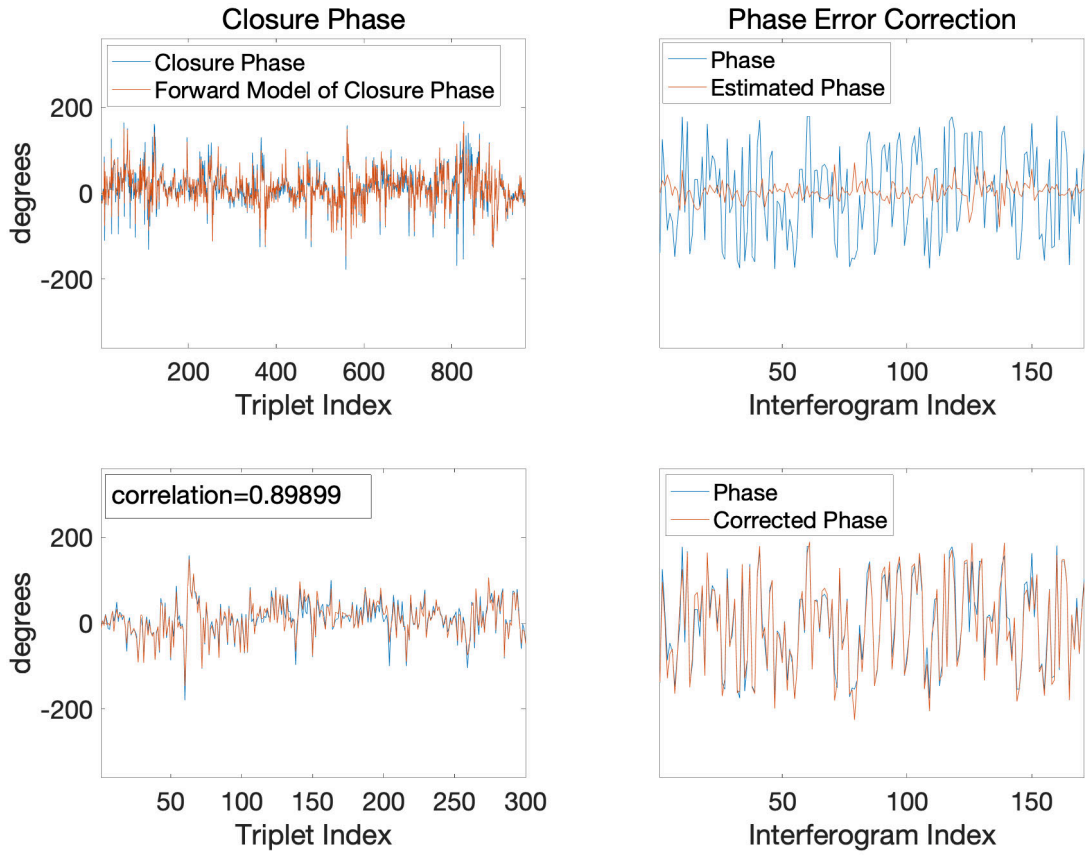

Figure 5.2: Demonstration of the phase closure SVD algorithm for a single pixel. Top left: The actual $K = 969$ closure phase values for a single pixel are plotted in blue, while the forward model of closure phase (Equation 5.12) are plotted in red. Bottom left: a smaller portion of the top left figure is shown to illustrate the good agreement between the actual phase closure and the forward model of the phase closure. Top right: The actual $M = 171$ interferometric phases for the same pixel are plotted in blue, while the estimated decorrelation phases (Equation 5.13) are plotted in red. Bottom right: The actual $M = 171$ interferometric phases for the same pixel are plotted in blue, while the corrected propagative phase (Equation 5.16) are plotted in red.

to phase nonclosure is solved for and removed from the set of interferograms with a truncated SVD method (see Figure 5.2 for an example). We unwrap both the original and the corrected interferograms using the SNAPHU algorithm [Chen and Zebker, 2002], phase calibrate both sets of unwrapped interferograms, and then stack each set of interferograms to estimate the mean line of sight (LOS) velocity associated with the subsidence feature as in [Chen et al., 2017b]. These results, along with the difference in estimated LOS velocity between the corrected and uncorrected sets of interferograms, and the average coherence of the stack of interferograms, are displayed in Figure 5.3.

For suitably large deformation signals, such as the central surface subsidence feature in Figure 5.3, The difference in inferred mean LOS velocity due to decorrelation phase is small. Notice, however, deviations in velocity estimates associated with agricultural fields, where variable vegetation and soil moisture superimposes phase errors over the deformation signal (see Figure 5.4). Even in regions of high coherence ($\gamma > 0.7$), standard deviations in differences in velocity estimates on the order of several millimeters per year can be observed between adjacent bare agricultural surfaces, likely reflecting variable soil moisture. In agricultural fields distant from the subsidence feature, these deviations in deformation rates are comparable to the magnitude of the total inferred ground deformation rates themselves. Even minor temporal decorrelation can introduce systematic biases in inferred deformation rates, which can be significant when considering subtle deformation signals.

We can directly compare the empirical variance of the best fitting decorrelation phase to the Cramer-Rao lower bound, which is commonly used for uncertainty analysis in InSAR applications [Seymour and Cumming, 1994; Guarnieri and Tebaldini, 2007]. We model the coherence as containing a temporal, spatial, and thermal component as in [Zebker and Villasenor, 1992]:

$$\gamma_{total} = \gamma_{temporal} \cdot \gamma_{spatial} \cdot \gamma_{thermal} \tag{5.20}$$

where the thermal decorrelation is defined as:

$$\gamma_{thermal} = \frac{1}{1 + \frac{1}{SNR}} \tag{5.21}$$

The SNR of the ALOS PALSAR instrument ranges from 20-30 dB, yielding $\gamma_{thermal} \approx 0.9$. The spatial decorrelation is due to variations in the path length to distributed scatterers contained within each resolution cell caused by variable spatial baseline between SAR image acquisitions, and is derived in [Zebker and Villasenor, 1992] as:

$$\gamma_{spatial} = 1 - \frac{2|B_p|R_{az}cos^2(\theta)}{\lambda r} \tag{5.22}$$

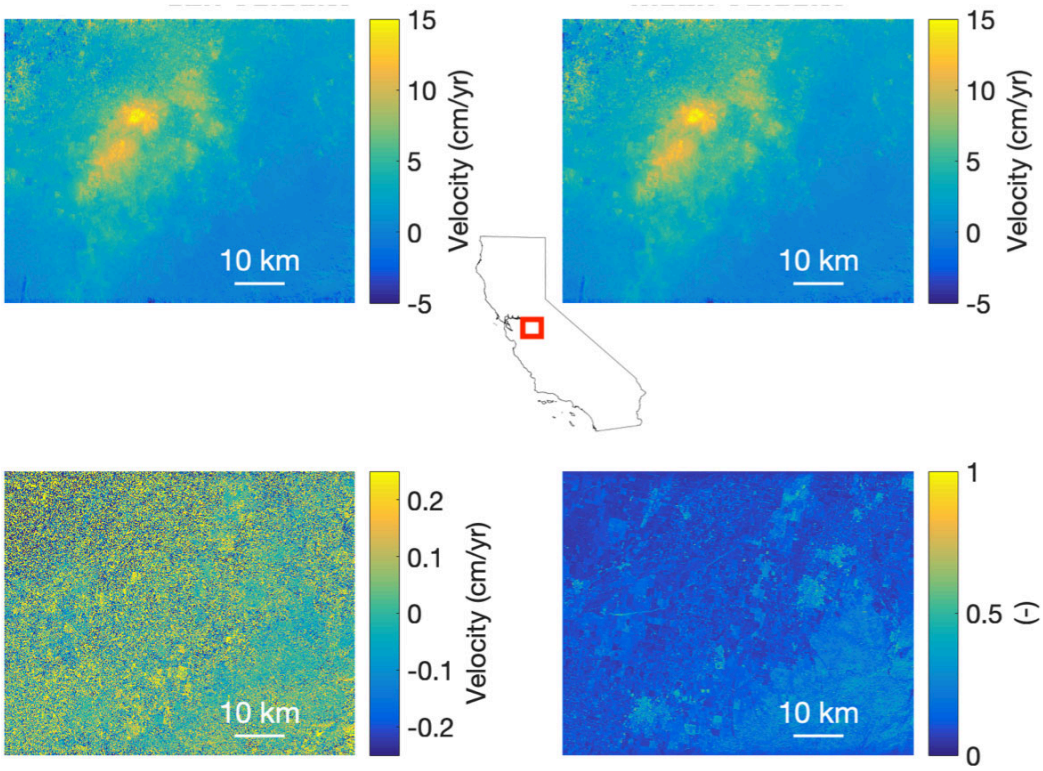

Figure 5.3: Top left: Estimated LOS velocity for stack of original interferograms. Top right: Estimated LOS velocity for stack of corrected interferograms. Bottom left: Difference between estimated LOS velocities for original and corrected interferograms (i.e. the component of the mean LOS velocity estimate due to decorrelative phase). Bottom right: The average coherence of the series of interferograms. Positive velocities correspond to subsidence.

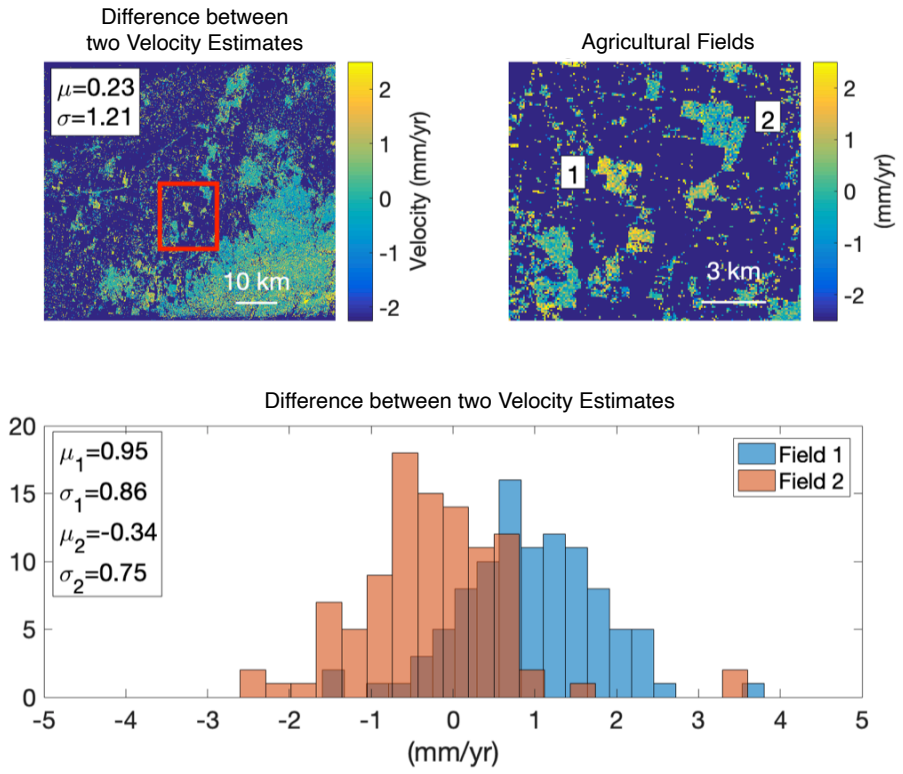

Figure 5.4: Top left: Difference between estimated LOS velocities for original and corrected interferograms, with scene-wide mean and standard-deviation of regions with $\gamma > 0.35$. Top right: Difference in velocity estimates of two agricultural fields corresponding to the red box in the top left figure. Bottom: Histogram of difference in velocity estimates between agricultural fields 1 and 2, with their respective mean values and standard deviations noted.

where $|B_{perp}|$ is the magnitude of the perpendicular spatial baseline, R_{az} is the native azimuth resolution (5 m for ALOS PALSAR), θ is the incidence angle (34.3° for this dataset), λ is the wavelength (23.7 cm), and r is the range from the radar to the illuminated surface ($r \approx 847,166$ m in this case).

We assume that nonzero phase closure is due solely to temporal decorrelation, and we therefore estimate the total temporal decorrelation by rearranging Equation 5.20:

$$\gamma_{temporal} = \frac{\gamma_{total}}{\gamma_{spatial} \cdot \gamma_{thermal}} \tag{5.23}$$

The Cramer-Rao bound on phase variance, as in [Seymour and Cumming, 1994; Guarnieri and Tebaldini, 2007; Samiei-Esfahany et al., 2016], is:

$$\sigma_{\varphi_{cr}} = \frac{1}{2L}\frac{1-\gamma^2}{\gamma} \tag{5.24}$$

where L is the number of looks and γ is the coherence. We can modify Equation 5.24 by substituting $\gamma_{temporal}$ for γ:

$$\sigma_{\varphi_{temporal_{cr}}} = \frac{1}{2L}\frac{1-\gamma_{temporal}^2}{\gamma_{temporal}} \tag{5.25}$$

To derive the Cramer-Rao lower bound on phase variance due to temporal decorrelation. Figure 5.5 illustrates that the variance of the best fitting decorrelation phase is properly bounded by Equation 5.24, and that as the temporal coherence increases, the decorrelation phase variance approaches the Cramer-Rao bound. However, for heavily decorrelated regions, where decorrelation phase errors are large, the actual phase variance is noticeably larger than the Cramer-Rao lower bound. Nonetheless, it is evident that the empirical variance of the decorrelation phase is strongly correlated with coherence, and can be approximated by the Cramer-Rao bound. These results further show that nonzero phase closure arises from signal decorrelation, and that this relationship is captured by the simple model described in Section 5.1.

5.3.2 Potential Phase Unwrapping Errors

Application of the phase closure SVD algorithm modifies the inputs for phase unwrapping, introducing the potential for different unwrapped phase solutions. We investigate this algorithm's susceptibility to generating phase unwrapping errors by unwrapping both the original ('uncorrected') and the decorrelation-corrected ('corrected') interferograms using SNAPHU. We then compare both the

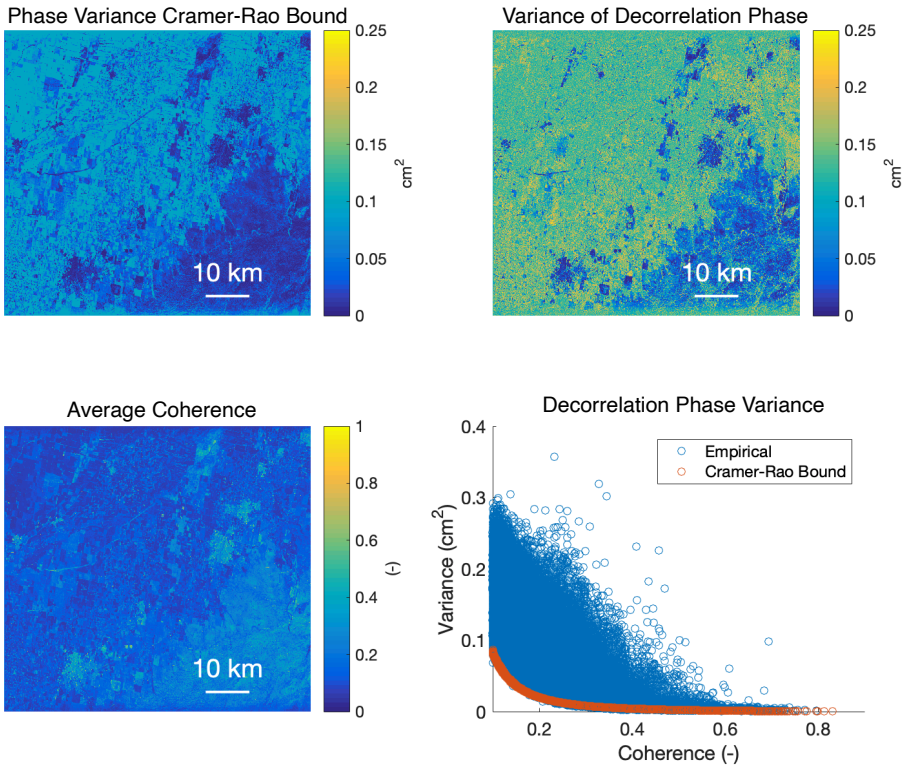

Figure 5.5: Top left: Cramer-Rao lower-bound of phase variance. Top right: The empirical variance of the decorrelation phase. Bottom left: The average coherence of the series of interferograms. Bottom right: Decorrelation phase variance vs. coherence, lower-bounded by the Cramer-Rao bound.

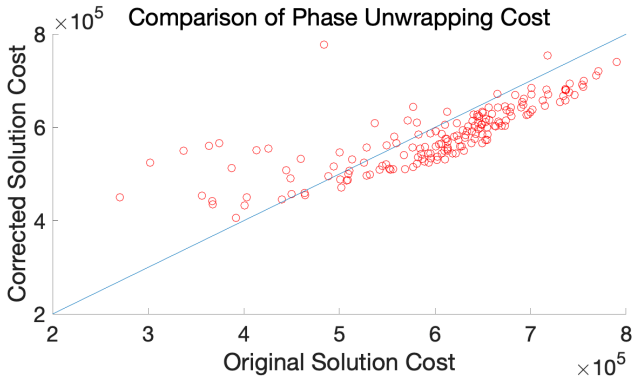

Figure 5.6: SNAPHU phase unwrapping solution cost for corrected vs. uncorrected interferograms.

solution costs and the final solutions for both cases. A lower SNAPHU solution cost corresponds to a better solution to the phase unwrapping problem [Chen and Zebker, 2002; Chen and Zebker, 2001]. Figure 5.6 shows a scatter plot of the SNAPHU phase-unwrapping solution costs for the corrected vs uncorrected interferograms. Points lying under the diagonal line indicate a lower solution cost, and therefore an improved phase unwrapping solution, for the corrected interferograms compared to the uncorrected interferograms. When the decorrelation phase solved for with this algorithm is removed from the original interferograms, a more reliable estimate of the true unwrapped propagative phase is found.

We can define the relative cost improvement (RCI) of removing the best fitting estimate of phase decorrelation as follows:

$$RCI = \frac{c_1 - c_2}{c_1} \tag{5.26}$$

where c_1 is the SNAPHU solution cost for unwrapping the phase of the uncorrected interferogram, while c_2 is the SNAPHU solution cost for unwrapping the phase of the corrected interferogram. Values of $RCI > 0$ therefore correspond to improved unwrapping solutions after applying the decorrelation phase correction. The RCI as a function of both the temporal and spatial baselines of each interferogram pair is displayed in Figure 5.7. It is apparent that RCI increases as the temporal baseline increases. Intuitively, temporal decorrelation is strongly correlated with temporal baseline, so for larger temporal baselines we expect larger decorrelation phases. Conversely, we do not observe as direct of a relationship between RCI and spatial baseline. There are several interferograms with small spatial baselines for which RCI is negative, but this may be due to the correlation between spatial and temporal baseline for the ALOS spacecraft (i.e. these negative RCI values are actually attributable to small temporal baselines rather than spatial baselines). Traditionally, temporal decorrelation is assumed independent of spatial baseline and attributed merely to the stochastic

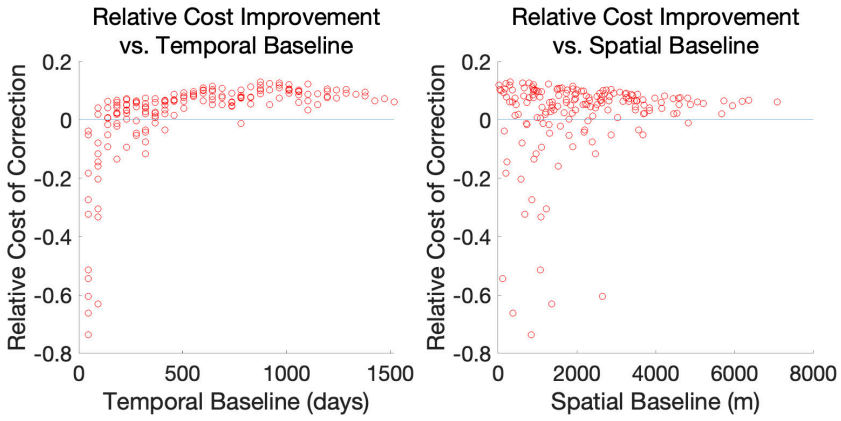

Figure 5.7: RCI vs. temporal (left) and spatial (right) baselines.

random motions of surface scatterers within a resolution element between image acquisitions (which is consistent with the behavior in Figure 5.6). If, however, temporal decorrelation is partially attributable to propagation through a decorrelative volume such as a vegetation canopy or snowpack, then significant differences in spatial baseline will result in different path lengths through the decorrelative volume, in which case one might expect a more pronounced correlation between spatial baseline and decorrelation phase (and thus RCI). Nonetheless, these results suggest that the estimate of decorrelation phase provided by the phase closure SVD solution is comparable to the true decorrelation phase, and its successful removal results in improved phase unwrapping solutions.

For scenes with significant decorrelation, isolated patches of coherent phase distributed across the scene can exhibit 2π phase ambiguities with respect to each other. Integer phase ambiguities between different patches is a commonly-reported issue in phase unwrapping [Lauknes et al., 2011; Reeves et al., 2011]. Application of the phase closure SVD algorithm can change the scene-wide distribution of 2π phase ambiguities between isolated patches of phase. This is illustrated in Figure 5.8; color groups (i.e. green, yellow, and blue) correspond to different estimates of the integer number of phase cycles per pixel during phase unwrapping as between the original unwrapped interferograms and the corrected interferograms. We note, however, that these phase ambiguities are normally distributed, and for a suitably large set of interferograms (N=171 in this study), the difference in phase ambiguities between isolated decorrelation patches tends towards zero when the entire stack of interferograms is considered.

Whether or not this phase closure SVD algorithm is used, the phase unwrapping procedure can introduce 2π phase ambiguities. However, we have demonstrated that removing the best fitting decorrelative phase from a set of interferograms using the phase closure SVD algorithm leads to improved phase unwrapping solutions for the majority of interferograms analyzed. The potential to use closure phase for improved phase unwrapping solutions has been noted by others [Zhang et al.,

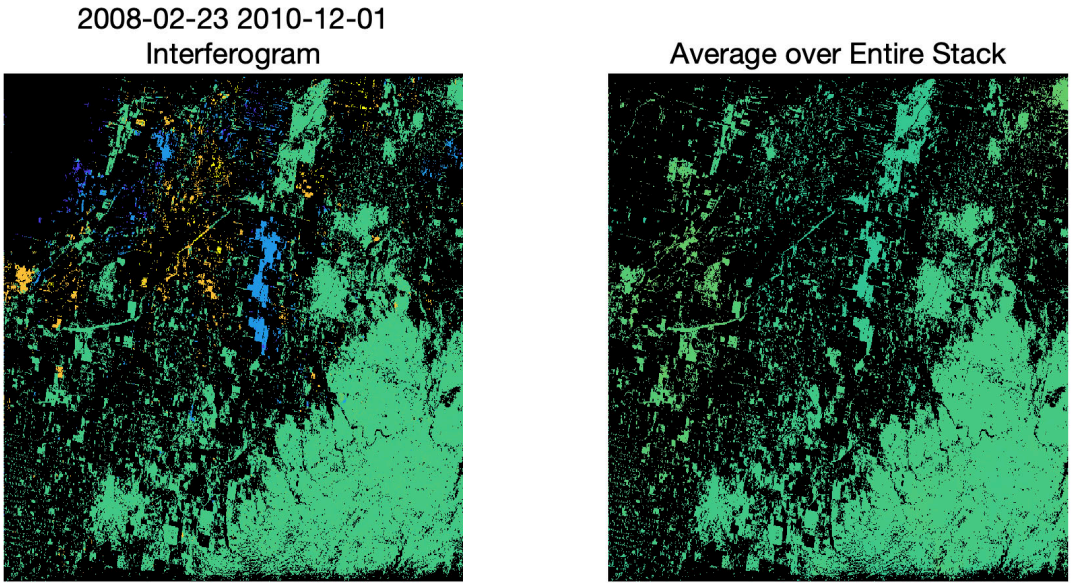

Figure 5.8: Color groups (i.e. green, yellow, and blue) correspond to different estimates of the integer number of phase cycles per pixel during phase unwrapping between the corrected and uncorrected interferograms. A single interferogram (top), illustrating phase ambiguities over several agricultural fields, (bottom) the average integer difference of phase cycles over the entire set of interferograms is effectively constant for a suitably large set of interferograms (N=171 in this study).

2018]. Interferometric phase closure can be exploited to both quantify the decorrelative component of phase noise, and to retrieve improved unwrapped phase solutions for InSAR applications.

5.4 Summary

The algorithm presented in this chapter leverages the intrinsic information contained within closure phase triplets to estimate the component of the interferometric phase that is due solely to signal decorrelation in InSAR. Conceptually, the algorithm is analogous to the SBAS algorithm, where the closure phase triplets and the decorrelative component of interferometric phase in this algorithm are analogous to the deformation phase and interferometric phase as described in [Berardino et al., 2002].

We apply this algorithm to a set of ALOS SAR scenes collected over a subsidence feature in California's Central Valley, and demonstrate that the variance of the algorithm's estimated decorrelative phase component is comparable to the theoretical phase variance due to signal decorrelation as calculated in [Rodriguez and Martin, 1992]. We demonstrate an improvement in phase unwrapping solutions after removing the decorrelation phase. Furthermore, differences in the mean LOS velocity between stacks of uncorrected and corrected interferograms can differ by several millimeters per year. In applications where deformation rates are expected to be small, such as slow slip earthquakes or interseismic deformation, or where surface deformations are strongly correlated with temporal decorrelation, such as the freezing and thawing of permafrost, phase errors due to signal decorrelation can introduce a significant bias to inferred deformation rates.

Because this is a simple linear model, it is relatively straightforward to introduce a-priori knowledge of the temporal behavior of the decorrelative phase. Additionally, the decorrelative phase can be further subdivided into components arising from specific physical processes, such as time-variable dielectric permittivity (due to variable soil moisture content as in [De Zan et al., 2014; Zwieback et al., 2015b]), or surface roughness. Given a suitable physical model to describe the effect of these decorrelative phenomena on the radar signal phase, this technique could be applied to time-series analysis of properties such as soil moisture (recently as in [De Zan and Gomba, 2018]), snow water equivalent (SWE), vegetation cover/biomass, surface roughness, and others. These points are addressed in the following chapter, where we derive a simple physical decorrelation model, and discuss the potential for soil moisture estimation using closure phase and decorrelation phase observations.

Chapter 6

Closure Phase-Consistent Interferometric Model

In this chapter, we derive a general imaging model for interferometric synthetic aperture radar (InSAR) that explicitly considers the statistical properties of surface roughness and volume scattering. We show that this 'partially-correlated interferometric model' (PCIM) reduces to the common imaging models used by the SAR community when idealized simplifications concerning the statistics of scattering elements are made. The PCIM model provides analytic solutions when more physically realistic assumptions of scattering statistics, surface roughness, and volume scattering are retained, while simpler imaging models cannot adequately capture this physical behavior. We demonstrate the potential of the PCIM model for more accurate investigations of interferometric closure phase, and its sensitivity to wavelength-dependent behavior in interferometric closure phase – which has not previously been reported in the literature. We discuss the benefit of the PCIM model for both improved error quantification in existing geodetic techniques, and its potential for soil moisture retrieval; specifically within the context of the upcoming dual-frequency NISAR mission. Finally, we propose a methodology for retrieving soil moisture information from closure phase observations. We briefly discuss implementation of this methodology, and then discuss the degree to which the assumed interferometric soil moisture model, and the assumed statistics of surface scatterers impacts the sensitivity of closure phase observations to surface soil moisture.

6.1 Soil Moisture and InSAR Signal Decorrelation

Interferometric synthetic aperture radar (InSAR) is a radar-based geodetic technique capable of resolving centimetric-level deformation of the Earth's surface with millimetric precision at high spatial resolution [Rosen et al., 2000]. Decorrelation of the radar signals in an interferometric pair is often

the critical limiting phenomena that precludes precise geodetic measurement. For this reason, much effort has been devoted to understanding both the physics and statistics of decorrelation noise, as well as the geophysical processes and properties that give rise to interferometric decorrelation [Zebker and Villasenor, 1992; Agram and Simons, 2015]. Since the publication of Zebker and Villasenor's work on interferometric decorrelation, many subsequent papers have related decorrelation to a range of imaging properties [Tough et al., 1995; Gatelli et al., 1994; Lee et al., 1994; Joughin et al., 1994; Touzi et al., 1999; Ferretti et al., 1999], and surface/geophysical properties [Treuhaft et al., 1996; Treuhaft and Siqueira, 2000; Rabus et al., 2010; Luo et al., 2000; Hoen and Zebker, 2000; Hensley et al., 2011; De Zan et al., 2014; De Zan et al., 2015; Zwieback et al., 2015a].

There has been significant interest in recent years in understanding the effects of soil moisture on interferometric measurements [Nolan and Fatland, 2003; Nolan et al., 2003; Barrett et al., 2013]. Several scattering models have been proposed that relate variations in the dielectric permittivity of the surface and near subsurface (associated with changes in volumetric water content) to variations in measured interferometric phase [De Zan et al., 2014; Zwieback et al., 2015b]. It has also has been noted that phase nonclosure, or lack of phase triangularity (hereafter referred to as closure phase) is similarly sensitive to the soil moisture state of the surface and near subsurface. As a result, there is continuing interest in exploiting phase closure as a method of mapping soil moisture, as the spatial resolution of active SAR instruments is several orders of magnitude finer than most radiometers used for conventional soil moisture measurement [De Zan and Gomba, 2018; Entekhabi et al., 2010]. An initial attempt at a soil moisture retrieval using closure phase showed promising results [De Zan and Gomba, 2018], although additional work is needed to more fully formulate a complete physical understanding of the physical link between closure phase and variable soil moisture, as well as how closure phase manifests in active radar imaging systems.

Here, we demonstrate that a mathematical idealization made in Zebker and Villasenor [1992], and implicitly adopted by most subsequent studies on interferometric decorrelation, is inconsistent with several of the other implicit assumptions made by scattering models that explicitly consider soil moisture. Namely, the assumption made of statistically uncorrelated scatterers (i.e. any ensemble distribution of scatterers with a Dirac delta autocorrelation function) is invalid when a volume of scatterers with variable dielectric permittivity is considered.

In this chapter, we propose a more general formulation of the interferometric scattering model described in Zebker and Villasenor [1992], which is generalized for scattering targets of any arbitrary autocorrelation function. We demonstrate that this partially-correlated interferometric model (PCIM) is reducible to the models derived in De Zan et al. [2014] and Zwieback et al. [2015] under idealized scattering assumptions. We further demonstrate that the PCIM model provides a more complete physical basis for the manifestation of interferometric closure phase which is dependent upon both systematic changes in dielectric permittivity as well as the statistics of the scattering elements themselves, thus explicitly linking closure phase to both systematic phase effects (variations

in dielectric permittivity) and stochastic phase effects (statistical scattering). Using Monte Carlo simulations, we discuss closure phase within the context of signal decorrelation, and demonstrate key differences between the PCIM model and previous scattering models. We discuss the potential of the PCIM model for soil moisture retrievals, with a specific focus on the upcoming NASA-ISRO Synthetic Aperture Radar (NISAR) mission. Lastly, we propose a simple algorithm for estimating changes in soil moisture from closure phase and decorrelation phase observations.

The rest of the chapter is organized as follows: Section 6.2 provides a brief background on interferometric decorrelation and interferometric closure phase. Section 6.3 details the PCIM model. Section 6.4 contains the results from model simulations based upon the PCIM. Section 6.5 discusses the most salient aspects of the PCIM model, as well as its potential for improved soil moisture retrieval using closure phase measurements. Section 6.6 details the simple soil moisture retrieval algorithm, and Section 6.7 provides concluding remarks.

6.2 Closure Phase and Surface Scattering Properties

A focused SAR image is an array of complex-valued pixels, each of which corresponds to the complex SAR backscatter from a given resolution element (resel) from the surface of the earth. As shown in Section 3.7, the complex correlation is:

$$\hat{\gamma} = \frac{\langle s_1 s_2^* \rangle}{\sqrt{\langle s_1 s_1^* \rangle}\sqrt{\langle s_2 s_2^* \rangle}} \tag{6.1}$$

For any three SAR images, the bicoherence is defined as:

$$\hat{\Xi}_{123} = \hat{\gamma}_{12}\hat{\gamma}_{23}\hat{\gamma}_{13}^* \tag{6.2}$$

Like the correlation, the bicoherence is a complex quantity with a corresponding phase term, the closure phase:

$$\xi_{123} = \angle\hat{\Xi}_{123} \tag{6.3}$$

The closure phase is invariant to any purely propagational phase terms – such as surface deformation, atmospheric delay, or topographic errors – that contribute to the interferometric phase of the individual SAR pairs [De Zan et al., 2014; Zwieback et al., 2015b; Michaelides et al., 2019b]. For an idealized, perfectly coherent scattering element, the closure phase should always be identically

zero. However, a combination of stochastic signal decorrelation and systematically variable attenuation rates and transmission wavenumbers during volume scattering can generate nonzero closure phase [De Zan et al., 2015; Michaelides et al., 2019b].

In this manner, closure phase is most sensitive to the physical scattering properties of the ensemble of scatterers that give rise to SAR backscatter in any given resel. This direct sensitivity to target scattering properties and invariance to propagational phase terms makes closure phase a potentially powerful complementary interferometric observable to interferometric phase and correlation. However, the physics and statistics that give rise to closure phase have yet to be completely determined. While the models proposed by [De Zan et al., 2014] and [Zwieback et al., 2015b] show potential to leverage closure phase for retrieval of surface soil moisture content, we propose a modification to De Zan's 2014 model. By explicitly accounting for 1): Snell's Law refraction and the horizontal divergence of transmitted ray paths that it induces in volume scattering, and 2): a more general expression for the autocorrelation of the ensemble scattering elements that give rise to SAR backscatter, our model detailed below offers applicability to a greater range of scattering targets and phenomena.

6.3 PCIM Model

In the most general formulation, we can model the time-dependent scattering target of the surface, near-subsurface, and any vegetation layers or diffusely distributed sub-resolution scattering elements as a general ensemble volume of stochastic scatterers $g(x, y, z, t)$. Ignoring the y-axis without loss of generality, we can express the SAR signal s acquired at time $t = t_1$ as:

$$s_1 = \int\int \rho(x_1, z_1, t_1) e^{-i2k_0 r_1} e^{-i2k_{x1} x_1} e^{-i2k_{z1} z_1} dx_1 dz_1 + n_1 \tag{6.4}$$

where the complex SAR backscatter $\rho(x_1, z_1, t_1)$ is a product of the radar system impulse response (assumed constant) and the ensemble distribution of complex scatterers (i.e. $g(x, y, z, t)$) at time $t = t_1$, k_0 is the wave velocity of the radar wave in vacuum (assumed time-invariant and purely real), r_1 is the component of the ray path that propagates in vacuum (i.e. the range to the target), x_1 and z_1 are the horizontal and vertical components of the ray path within the scattering volume, respectively, k_{x1} and k_{z1} are the corresponding components of the transmitted complex wavenumber in the scattering volume, and n_1 is an additive thermal noise term. We can similarly define the SAR signal s_2 measured by the SAR interferometer at time $t = t_2$ as:

$$s_2 = \int\int \rho(x_2, z_2, t_2) e^{-i2k_0 r_2} e^{-i2k_{x2} x_2} e^{-i2k_{z2} z_2} dx_2 dz_2 + n_2 \tag{6.5}$$

The complex correlation I_{12} formed by complex conjugation of these two signals is therefore:

$$I_{12} = \langle s_1 s_2^* \rangle = \int\int\int\int \langle \rho(x_1, z_1, t_1)\rho(x_2, z_2, t_2)^* \rangle [\mathbf{K}] dx_1 dx_2 dz_1 dz_2 + \langle n_1 n_2^* \rangle \tag{6.6}$$

where:

$$[\mathbf{K}] = e^{-i2k_0(\langle r_1 - r_2 \rangle)} e^{-i2(\langle k_{x1}x_1 - k_{x2}^* x_2 \rangle)} e^{-i2(\langle k_{z1}z_1 - k_{z2}^* z_2 \rangle)} \tag{6.7}$$

Note that this expression is equivalent to the numerator of Equation 6.1 (i.e. the unnormalized complex correlation). Because scattering is a stochastic process, I_{12} is implicitly a statistical estimator, the fidelity of which depends upon the number of independent samples ('looks') taken during the ensemble averaging during estimation. The statistics of the complex correlation I_{12}, as well as the interferometric phase $\phi_{12} = \angle I_{12}$, are therefore dependent upon the statistics of each ensemble average in Equation 6.6. Real-valued and complex-valued wavenumbers, as well as scatterer positions are usually assumed to be deterministic parameters, while the complex SAR backscatter is generally assumed a stochastic random process [Zebker and Villasenor, 1992; De Zan et al., 2014].

The two dominant noise terms that manifest during complex correlation estimation are speckle and thermal noise [Goodman, 1985; Rodriguez and Martin, 1992; Ulaby and Long, 2014]. Speckle noise arises from the stochastic nature of the distribution of scattering elements. A common simplification is made by assuming that backscatter arises from uniformly distributed and uncorrelated scattering centers, whereby the ensemble average of the product of the two SAR backscatter terms becomes:

$$\langle \rho(x_1, z_1, t_1)\rho(x_2, z_2, t_2)^* \rangle = f(x_1, z_1, t_1)\delta(x_1 - x_2, z_1 - z_2, t_1 - t_2) \tag{6.8}$$

where $f(x, z, t)$ is a real function that encodes the radar cross-sections of embedded scatterers, and $\delta(q - q')$ is the Dirac delta function. In most InSAR applications, volume scattering is neglected, and by insertion of Equation 6.8, Equation 6.8 simplifies to:

$$I_{12} = \langle s_1 s_2^* \rangle = \int\int f(x_1 = 0, z_1 = 0, t_1) e^{-i2k_0(\langle r_1 - r_2 \rangle)} dx_1 dz_1 + \langle n_1 n_2^* \rangle \tag{6.9}$$

whereby the interferometric phase is a function purely of the ensemble expectation of the change in range between the illuminated ground surface at $x_1 = 0,\ z_1 = 0$ and the SAR platform. Subsurface penetration of the SAR signal was considered in De Zan et al. [2014] and Zwieback et al. [2015], by modifying Equation 6.8 to:

$$\langle \rho(z_1)\rho(z_2)^* \rangle = f(z_1)\delta(z_1 - z_2) \tag{6.10}$$

whereby the scatterer radar cross-section distribution is assumed time-invariant and a function solely of depth, which reduces Equation 6.6 to:

$$I_{12} = \langle s_1 s_2^* \rangle = \int\int f(z_1) e^{-i2k_0(\langle r_1 - r_2 \rangle)} e^{-i2(\langle k_{z1} z_1 - k_{z2}^* z_2 \rangle)} dz_1 + \langle n_1 n_2^* \rangle \tag{6.11}$$

In addition to the change in range between image acquisitions, the interferometric phase is now also affected by changes in the complex vertical wavenumber k_z. Variations in the real component of the vertical wavenumber generate a phasor term analogous to the phasor caused by changes in range, while the imaginary component of the wavenumber attenuates the complex correlation (which in turn can induce a depth-dependent phase excursion). If variations in the refraction angle at the air-surface interface are assumed negligible and Equation 6.10 is taken to be constant with depth – as in De Zan et al. [2014] – then Equation 6.11 has an analytic solution of the form:

$$I_{12} = \langle s_1 s_2^* \rangle = \frac{1}{2i(k_{z1} - k_{z2}^*)} \tag{6.12}$$

In actuality, physically realistic variations in the complex dielectric permittivity of a scattering volume can generate variations in the refraction angle which can in turn generate divergences of the refracted ray path on the order of millimeters to centimeters for soils, and tens of centimeters for vegetation canopies (see Appendix C). Such deviations between image acquisitions modifies the autocorrelation of the volume ensemble of scattering elements, introducing systematic biases in both interferometric phase and complex correlation.

Equation 6.8 can be more generally expressed as:

$$\langle \rho(x_1, z_1, t_1)\rho(x_2, z_2, t_2)^* \rangle = R(x_1 - x_2, z_1 - z_2, t_1 - t_2) \tag{6.13}$$

where R is the autocorrelation of the complex signal ρ. In the case of time-invariant uncorrelated scatterers, the autocorrelation of such a distribution reduces to the form of Equation 6.8. Such a simplification is idealized, and invalid either when scattering distributions are more accurately modeled as stochastic processes, and/or when variable dielectric permittivity during volume scattering causes a horizontal divergence of the transmitted ray path.

By way of example we first consider the case of a homogeneous volume of time-variant dielectric permittivity and explicitly account for horizontal divergences in refracted ray paths. We then

consider a volume with fluctuations in dielectric permittivity (conceptually analogous to either compositional variations, changes in volumetric soil moisture, pore space, and/or surface roughness), which we model as stochastic random processes. We derive an expression for the complex correlation for the above volume in the presence of a time-variant bulk dielectric permittivity. Finally, we consider the general case of a scattering volume with time-variant bulk dielectric permittivity and time-dependent dielectric fluctuations.

Case 1: Time-variant homogeneous scattering volume

Conceptually, this scenario is equivalent to the model derived by [De Zan et al., 2014] with the explicit inclusion of variable refraction angle. For simplicity, we drop the range phasors and thermal noise terms from Equation 6.6, as these are not affected by the volume integration. For a homogeneous scattering volume, we first assume that scatterers are uncorrelated vertically and perfectly correlated horizontally. This is equivalent to making the assumption of uncorrelated scatterers in Equation 6.8 while explicitly considering divergence of refracted ray paths. From Appendix C, we have noted that the horizontal wavenumber is unchanged upon transmission and purely real (i.e. $k_{x1} = k_{x2}^*$), so Equation 6.6 simplifies to:

$$I_{12} = \int\int\int f(z_1) e^{-i2(\langle k_x (x_1 - x_2)\rangle)} e^{-i2(\langle (k_{z1} - k_{z2}^*) z_1\rangle)} dx_1 dx_2 dz_1 \tag{6.14}$$

We note that $x_1 - x_2$ is equivalent to the horizontal offset between the refraction ray paths (see Appendix C). Making use of the linearity of the horizontal offset with respect to depth, we can rewrite Equation 6.14 as:

$$I_{12} = \int f(z_1) e^{i2(\langle k_x \frac{\partial \chi_{12}}{\partial z} z_1\rangle)} e^{-i2(\langle (k_{z1} - k_{z2}^*) z_1\rangle)} dz_1 \tag{6.15}$$

where the partial derivative of the horizontal offset with respect to depth, $\frac{\partial \chi_i}{\partial z}$, is independent of horizontal position.

We can see that Equation 6.3 is analogous to the expression derived by [De Zan et al., 2014] with the addition of a phasor term that is the product of the horizontal wavenumber and $\frac{\partial \chi_i}{\partial z}$. Both the horizontal and vertical phasors are dependent upon the dielectric contrast; the horizontal phasor through the term $\frac{\partial \chi_i}{\partial z}$, and the vertical phasor through the term $(k_{z1} - k_{z2}^*)$.

Notably, the signs of these two terms remain the same regardless of dielectric contrast (or the sign of the dielectric contrast); however the sign change of the horizontal phasor ensures that the horizontal and vertical phasors act contrary to each other. Conceptually, neglecting to account for horizontal phase shifts due to variable refraction ray path as in De Zan et al. [2014] and Zwieback

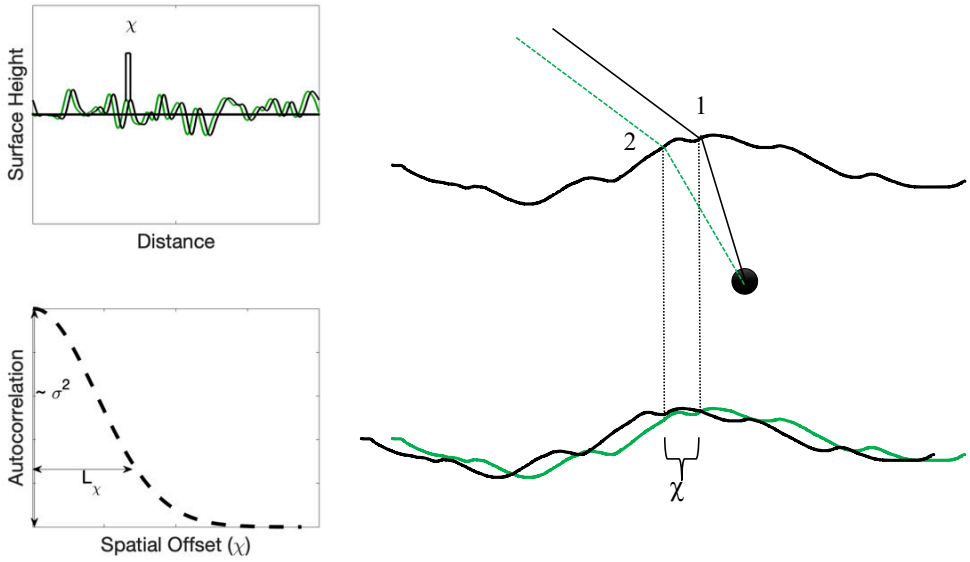

Figure 6.1: Right: Geometry of subsurface scattering. Variations in refractive angle due to variations in complex permittivity result in different ray paths between the SAR platform and the embedded scatterer. Top left: The autocorrelation of a stochastic random process is dependent upon the spatial lag, x_χ. Bottom right: The magnitude of the autocorrelation is dependent upon the standard deviation of the surface heights σ and the correlation length L_χ of the surface.

et al. 2015 results in an overestimate of the interferometric phase due to propagation through a volume of time-variant dielectric permittivity.

Case 2: Time-invariant scattering volume with spatial dielectric fluctuations

The model described in De Zan et al. [2014] and Zwieback et al. 2015 implicitly assumes that variations in refractive angle as a function of subsurface dielectric permittivity are small enough to be ignored. If, however, variations in refractive angle are explicitly accounted for in conjunction with stochastically rough surfaces, the autocorrelation of any volume distribution of scatterers will no longer be an idealized Dirac delta function. This point is demonstrated in Figure 6.1, which illustrates a stochastically rough surface overlying a homogeneous, time-variable dielectric halfspace with an embedded scatterer. Variations in the dielectric permittivity of the subsurface cause variations in the refractive angle at the air/surface interface; this in turn causes a variation in the total ray path between the embedded scatterer and the SAR interferometer. For any two ray paths corresponding to acquisition times with different bulk dielectric permittivities of the subsurface, the refraction points at the air/surface interface will differ from one another.

Analogously, for two ray paths that each impinge upon the surface at the same refraction point,

differences in subsurface dielectric permittivity will cause differences in refractive angle, yielding an increasing divergence between the two subsurface ray paths as a function of depth. Mathematically, this is equivalent to de-focusing the SAR interferometric imaging response; due to the divergence of the subsurface ray paths, the impulse response of the SAR interferometer is no longer a Dirac delta function. Instead, the interferometric impulse response (which is equivalent to the autocorrelation of the scatterer distribution) is actually a function of the surface roughness (or more generally, the statistics of the entire ensemble volume of scatterers), the dielectric contrast between image acquisitions, and the depth to discrete scatterers.

This interferometric impulse response can be represented as:

$$\langle \rho(x_1, z_1)\rho(x_2, z_2)^* \rangle = R(x_1 - x_2, z_1 - z_2) \tag{6.16}$$

This generalized model of the SAR interferometer's impulse response is illustrated in Figure 6.1, for an example wide-sense stationary (WSS) stochastic process with a Gaussian autocorrelation function. As the depth to any scatterer increases, and/or the contrast in dielectric permittivity between image acquisitions is made more pronounced, the horizontal spatial offset – and therefore the offset in refraction point at the air/surface boundary – will increase in turn. The smaller the autocorrelation length of the rough surface, the faster the autocorrelation of the rough surface approaches zero. The simplified model proposed by [De Zan et al., 2014] and [Zwieback et al., 2015b] corresponds to the limiting case where the autocorrelation length of the surface approaches zero, generating a Dirac delta autocorrelation function. Using the generalized autocorrelation expression in Equation 6.16, Equation 6.6 becomes:

$$I_{12} = \int\int\int\int R(x_1 - x_2, z_1 - z_2) e^{-i2k_0(r_1 - r_2)} e^{-i2k_x(x_1 - x_2)} e^{-i2(k_{z1}z_1 - k^*_{z2}z_2)} dx_1 dx_2 dz_1 dz_2 \tag{6.17}$$

The following changes of variables can be made:

$$x_2 = x_1 + \chi \qquad\qquad \chi = x_2 - x_1 \tag{6.18}$$

$$z_2 = z_1 + \zeta \qquad\qquad \zeta = z_2 - z_1 \tag{6.19}$$

$$k^*_{z2} = k_{z1} + \kappa_z \qquad\qquad \kappa_z = k^*_{z2} - k_{z1} \tag{6.20}$$

where χ and ζ are the increments of their respective stochastic processes, x and z. Assuming stationarity of increments, the autocorrelation function depends only upon the increment rather than the position in the stochastic process [Waechter et al., 2004]. Inserting these changes of variables into Equation 6.17 and simplifying yields:

$$I_{12} = \int\int R(\chi,\zeta)e^{-i2k_0(r_1-r_2)}e^{-i2(k_{z1}-k^*_{z2})z_1}e^{i2(k_x\chi+k^*_{z2}\zeta)}dx_1dz_1 \tag{6.21}$$

Upon inspection of Equation 6.17, it is evident that it is merely a more generalized form of the model first derived in De Zan et al. [2014]. When the autocorrelation of the stochastic distribution of scatterers is taken to be a Dirac delta function (as in De Zan et al. [2014] and Zwieback et al. 2015), $\chi \to 0$, $\zeta \to 0$ $R(\chi,\zeta) \to 1$, the last exponential in Equation 6.21 evaluates to 1, and the integration kernel in Equation 6.21 reduces to the form of Equation 6.11. We can therefore consider this last exponential term as a 'perturbation term' which encodes phasors associated with both horizontal spatial offset due to variable refractive angle, as well as small-scale (i.e. sub-facet) vertical surface roughness:

$$e^{i2(k_x\chi+k^*_{z2}\zeta)} = e^{i2k_x\chi}e^{i2k^*_{z2}\zeta} \tag{6.22}$$

where we have divided the exponential perturbation term into two components, the first of which encodes horizontal spatial offset, and the second of which encodes vertical small-scale roughness variations. Recognizing that the vertical roughness, z, is itself a WSS stochastic process with horizontal position x as the independent variable, we can express the exponent of the second exponential in Equation 6.22 as:

$$\zeta = z' - z = z(x+\chi) - z(x) \tag{6.23}$$

If we assume that the autocorrelation of the surface roughness is jointly distributed, then:

$$R(\chi,\zeta) = R(\chi)R(\zeta) \tag{6.24}$$

For a stationary process, the expectation of ζ will be zero:

$$E[\zeta] = E[z(x+\chi) - z(x)] = E[z(x+\chi)] - E[z(x)] = 0 \tag{6.25}$$

and the exponential perturbation term reduces to:

$$e^{i2k_x\chi} = e^{i2(\langle k_x \frac{\partial \chi_{12}}{\partial z} z_1\rangle)} \tag{6.26}$$

as in the previous section. We can then rewrite Equation 6.21 as:

$$I_{12} = \int\int R(\chi,\zeta) e^{-i2k_0(r_1-r_2)} e^{-i2(k_{z1}-k_{z2}^*)z_1} e^{i2k_x\chi} dx_1 dz_1 \tag{6.27}$$

Again, we notice that for spatially uncorrelated scatterers with identically zero correlation lengths, Equation 6.27 reduces to the form derived in De Zan et al. [2014] and Zwieback et al. 2015. If more physically realistic distributions of scatterers are considered, Equation 6.27 progressively deviates from the simpler form of Equation 6.11 as a function of both the autocorrelation of the stochastic process (in particular, the correlation length), and the horizontal offset (which is in turn a function of the dielectric contrast, and the scatterer depth).

Because the horizontal offset is implicitly a function of depth, and the wide-sense stationarity of the autocorrelation implies that the autocorrelation is a function only of the horizontal offsets (and not the horizontal positions), if we assume (1) that the scatterer distribution is purely a function of depth, and (2) that vertical interfaces are uncorrelated with each other, then Equation 6.27 simplifies to:

$$I_{12} = \int R(\chi) e^{-i2k_0(r_1-r_2)} e^{-i2(k_{z1}-k_{z2}^*)z_1} e^{i2k_x \frac{\partial \chi_{12}}{\partial z} z_1} dz_1 \tag{6.28}$$

where the dependence of the horizontal lag χ on depth z has been made explicit, and the complex correlation is now an integral only with respect to depth. If the autocorrelation is taken to be a Dirac delta function, the horizontal perturbation term evaluates to unity, and Equation 6.28 reduces to the familiar form derived in De Zan et al. [2014]. If horizontal layers are assumed to be perfectly correlated with themselves, then $R(\chi) = 1$ for all χ, and Equation 6.28 reduces to:

$$I_{12} = \int f(z_1) e^{-i2k_0(r_1-r_2)} e^{-i2(K_{z1}-k_{z2}^*)z_1} e^{i2k_x\chi(z_1)} dz_1 \tag{6.29}$$

This is analogous to the solution from De Zan et al. [2014], with an additional phase term in the integrand. Because the sign of the horizontal perturbation is opposite that of the vertical propagation term, this horizontal perturbation term generates a phase contrary to the phase caused from variations in the vertical wave velocity. In this sense, neglecting the horizontal phase terms caused by variable refractive angle results in an overestimate of the interferometric phase term due

to propagation in a volume of time-variant dielectric permittivity.

Case 3: Time-variant scattering volume with spatio-temporal dielectric fluctuations

To account for time-dependent behavior of the distribution of scatterers – due to, for example, progressive decorrelation due to random reorientation of surface scatterers or redistribution of surface roughnesses – one can generalize the equations from Case 2 by making the complex SAR backscatter explicitly a function of time. The autocorrelation of the complex SAR backscatter will therefore be:

$$\langle \rho(x_1, z_1, t_1) \rho(x_2, z_2, t_2)^* \rangle = R(x_1 - x_2, z_1 - z_2, t_1 - t_2) \tag{6.30}$$

Assuming stationarity in time as well as space, the integral corresponding to the interferogram will therefore be:

$$I_{12}(\tau) = \int\int R(\chi, \zeta, \tau) e^{-i2k_0(r_1 - r_2)} e^{-i2(k_{z1} - k_{z2}^*)z_1} e^{i2k_x \chi} dx_1 dz_1 \tag{6.31}$$

where $\tau = t_1 - t_2$ is the temporal baseline between the two image acquisitions. While it is relatively straightforward to derive these mathematical expressions, the choice of what the most appropriate statistical model to use for the distribution of scatterers and its associated autocorrelation is less obvious. We shall defer further consideration of this point until Section 6.5.

6.4 Comparison of PCIM Model with Monte Carlo Simulations

To assess the validity of the PCIM model presented in Section 6.3, we compare it to both the model described in De Zan et al. [2014] (referred to as the 'De Zan model'), and simulations from a Monte Carlo scattering model [Zebker, 2020]. The most salient difference between the De Zan model and the PCIM model is a change in the integration kernel (i.e. Equation 6.21). the integration kernel of the PCIM model has an additional depth-dependent phasor term associated with horizontal ray path divergence, as well as an additional depth-dependent attenuation rate associated with the statistics of the ensemble scattering volume. As such, both models depend heavily upon: 1) the assumed distribution of scatterers, in particular the vertical distribution of scatterers within the volume and their associated autocorrelation functions, and 2) the assumed dielectric mixing model.

Figure 6.2 compares the De Zan and PCIM models using the Hallikainen dielectric mixing model [Hallikainen et al., 1985] and two vertical scatterer distributions: 1) a constant, depth-independent

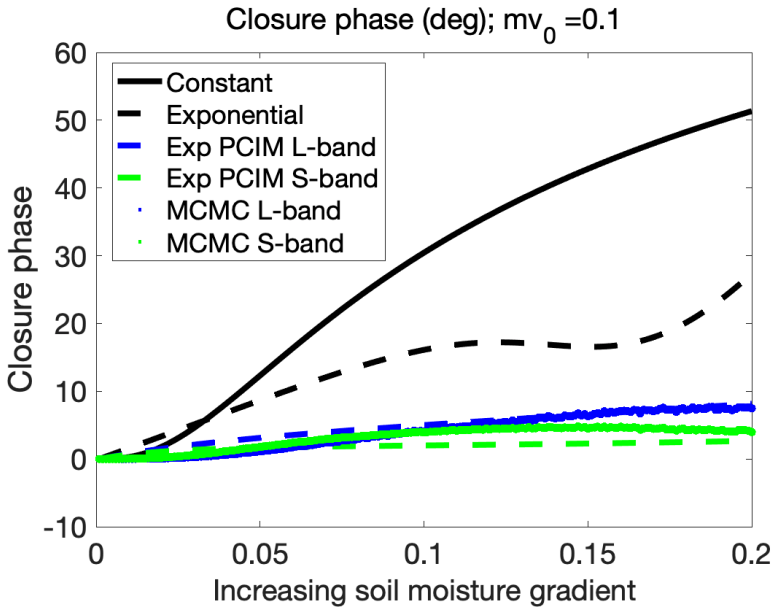

Figure 6.2: Comparison of the De Zan and PCIM models for a linear soil moisture gradient with initial soil moisture $mv_0 = 0.1$ and the dielectric mixing model from Hallikainen et al. [1985]. Both a constant, depth-independent scatterer distribution (solid line), and an exponential depth distribution (dashed lines) are shown. The wavelength dependence of the closure phase is only captured by the PCIM model with a depth-dependent scatterer distribution. Mean closure phase values from MCMC simulations for an exponential distribution of scatterers are plotted alongside the theoretical results.

distribution, and 2) an exponentially decaying distribution. For simplicity, we assumed a linear gradient in soil moisture between the 3 image acquisitions; that is, the soil moisture content in Image 3 is twice that of Image 2, which is in turn twice that of Image 1. As stated in Section 6.3, the PCIM model systematically estimates a smaller phase closure value than the De Zan model for both vertical distributions of scatterers.

The PCIM model predicts a noticeable wavelength-dependence on the closure phase for depth-dependent scattering models. In contrast, the De Zan model predicts a slight wavelength dependence for the exponential distribution, and wavelength independence for the constant distribution, as illustrated in Figure 6.3. This wavelength dependence arises from the real and imaginary components of the analytic expression for the bicoherence being equally proportional to the wavelength in Equation 6.12; the complex argument will therefore be independent of wavelength. Imposing a nonzero, wavelength-independent attenuation (which is purely real), breaks this independence, as the real and imaginary components are no longer equally proportional to the wavelength. The wavelength-dependence of the closure phase from the PCIM model is even more pronounced, as the autocorrelation of the distribution of volume scatterers introduces an additional attenuative term, even in the case of a constant distribution of vertical scatterers.

Comparing the results from our Monte Carlo model simulations to both the De Zan and PCIM models, we can see that the PCIM model yields a closer match to the simulation results than the De Zan model. Figure 6.4 illustrates the integration kernel of the two models, evaluated at a depth of 15 cm. The wavelength dependence of the closure phase is clear, as is the closer fit between the PCIM model and the simulation results. While the wavelength dependence is captured by the integration kernel of the De Zan model, without accounting for the phase terms associated with the horizontal depth-dependent ray path divergence, the De Zan integration kernel has a higher wavenumber than the PCIM kernel (see the leftward translation of the dotted line with respect to the solid line in Figure 6.4). This higher wavenumber is responsible for the observed leftward shift, which is observed for all integration depths (see Figure 6.5). The De Zan model systematically predicts a larger wavenumber than the PCIM model. as a result it diverges less from the infinite integration depth solutions (solid green and blue lines) than the PCIM model and Monte Carlo simulations, which better agree with each other. When integrated to arbitrary (or infinite) depth, the over-prediction of the wavenumber in the De Zan model results in a systematic over-estimate of the interferometric phase in comparison to the PCIM model and simulation results (see again Figure 6.2).

We generated numerical simulations and Monte Carlo simulations of closure phase as a function of both soil moisture gradient and effective integration depth. Figure 6.6 displays the results for both L-band and S-band. The numerical simulations of the analytic model and the Monte Carlo modeling generally agree, though they begin to diverge for large soil moisture gradients. It is evident that the analytical solution for a constant vertical depth distribution integrated to infinity presented

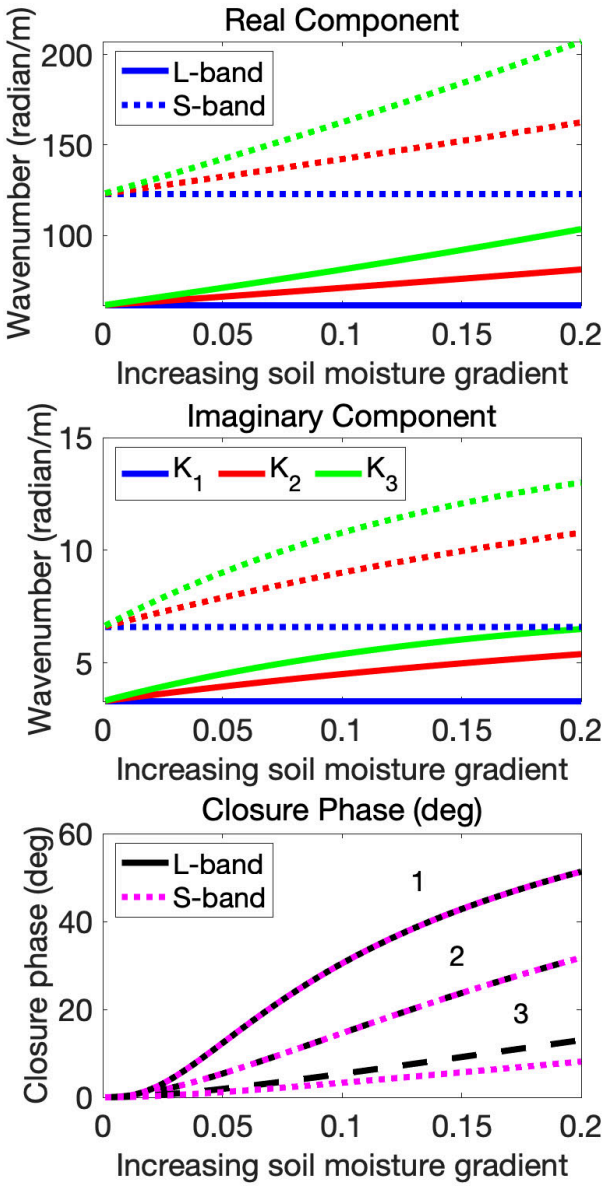

Figure 6.3: Wavelength Dependence. Top: The real component of the complex wavenumber for a constant vertical distribution. Middle: imaginary component. Bottom: The theoretical closure phases for L-band (black) and S-band (purple) yield identical results for a constant vertical distribution (curve 1). An exponential vertical distribution yields a very weak wavelength dependence with the De Zan model (curve 2). An exponential vertical distribution yields a more apparent wavelength dependence with the PCIM model (curve 3). Color schemes in top and middle plots are consistent.

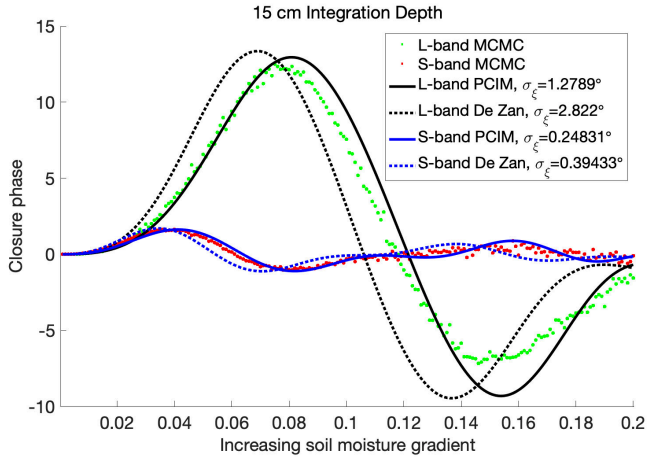

Figure 6.4: Comparison of the integration kernel of the De Zan (dotted) and PCIM (solid) lines evaluated at a depth of 15 cm. MCMC simulation results are plotted alongside for comparison. Standard deviation between the simulation results and the De Zan and PCIM models are inset.

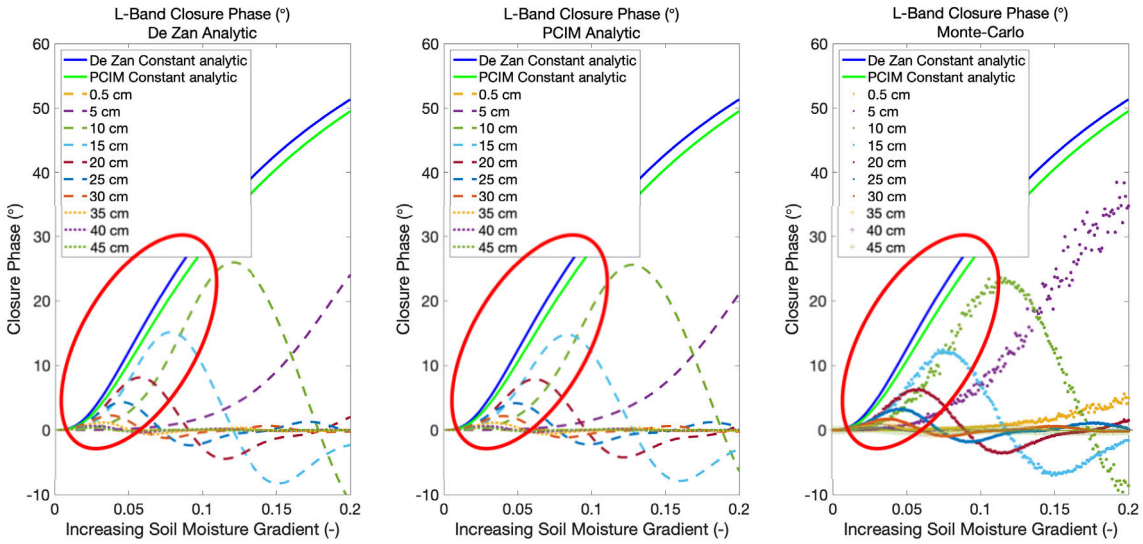

Figure 6.5: Left: De Zan analytic model. Middle: PCIM analytic model. Right: Monte Carlo simulations. The PCIM model and Monte Carlo simulations both resolve a greater divergence between the infinite integration depth solutions (solid green and blue lines) and finite integration depth solutions (dotted lines), than the De Zan model.

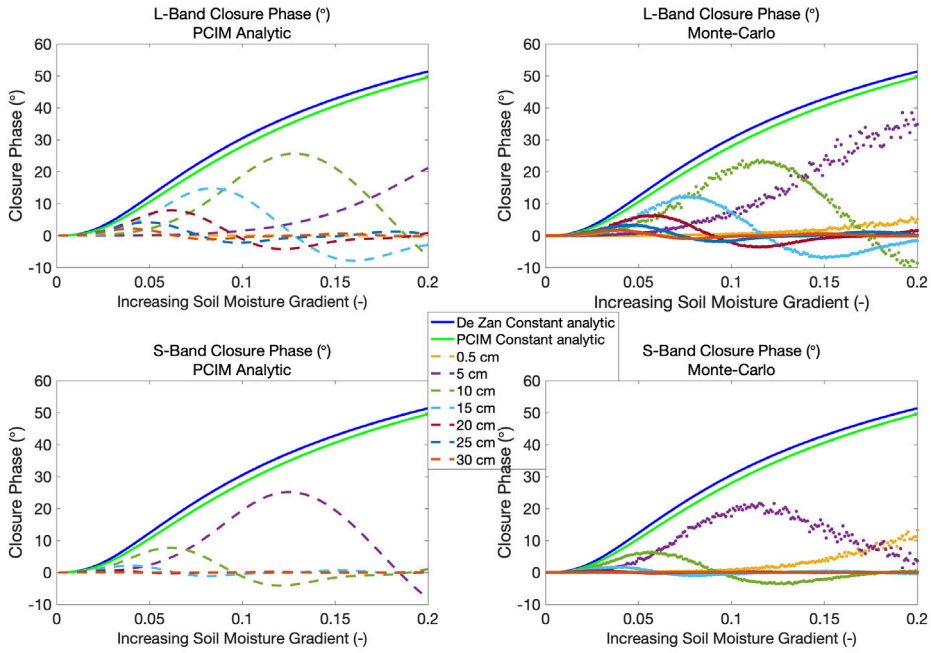

Figure 6.6: Comparison between analytic and Monte Carlo closure phase in L-band (top) and S-band (bottom) for: an infinite subsurface integration depth and constant vertical scatterer distribution using the De Zan model (solid blue line); an infinite subsurface integration depth and constant vertical scatterer distribution using the PCIM model (solid green line); varying discrete integration depths using the PCIM model (dotted lines); and Monte Carlo simulations for varying discrete integration depths (dots, colors are consistent with dotted lines).

in De Zan et al. [2014] is an upper-bound estimate for all solutions with a more physical finite depth of integration. For finite integration depths at both frequencies, penetration of at least $\sim \frac{\lambda}{10}$ is necessary for significant closure phase. Closure phase increases rapidly with increasing penetration depth for a small range, and then gradually decreases as integration depth continues to increase. Past an integration depth of $\sim \lambda$, significant closure phase is not observed. Despite the fact that the analytical solution for infinite integration depth is wavelength-independent, there is a clear wavelength dependence for finite integration depths, with larger wavelengths (lower frequencies) producing larger closure phase excursions. Notably, the solutions for finite integration depths are not monotonic as a function of soil moisture gradient. This is true for both the De Zan model and the PCIM model. However, as the vertical distribution of scatterers is constrained to be an exponential or Gaussian distribution, the behavior becomes more monotonic (as in Figure 6.2).

The numerical results from Figure 6.6 are repeated in Figure 6.7, where closure phase is now displayed as a function of effective integration depth (vertical axis) and increasing soil moisture gradient (horizontal axis). The $\frac{1}{e}$ penetration depths for each image used to form a closure phase triplet are shown in magenta (where images with larger soil moisture values correspond to shallower

penetration depths). The qualitative similarity between the two frequencies is apparent, as is the wavelength-dependence. Significantly, nonzero closure phase is mostly confined to a narrow band of integration depth and soil moisture, which suggests that measured closure phase is most sensitive to the soil moisture state at a given depth ($\sim \frac{D_{pene}}{2}$). Furthermore, this depth sensitivity is wavelength-dependent, with higher frequencies (smaller wavelengths) sensitive to shallower depth bands.

This wavelength sensitivity to different depths immediately suggests the potential to use multifrequency closure phase observations to characterize soil moisture at different depths. The upcoming dual-frequency L-band and S-band NISAR mission would provide an ideal opportunity to generate contemporaneous, dual-frequency closure observations. Furthermore, the nonmonotonic nature of the closure phase as a function of soil moisture gradient suggests that contemporaneous, multifrequency closure phase measurements could exploit this systematic wavelength dependence for improved soil moisture characterization.

The sensitivity of the PCIM model to the gradient in soil moisture suggests that the exponential decay in soil moisture observed following precipitation events [Njoku et al., 2003; McColl et al., 2017] provides a natural physical process around which to develop an initial closure phase-based soil moisture retrieval algorithm (see Figure 6.8). Because the gradient in soil moisture is constantly varying during an exponential decay, the closure phase signature associated with a soil moisture drydown should in turn be unique at any point in time. By generating time series of contemporaneous L-band and S-band NISAR observations of expected or known drydown events – associated with precipitation events or flooding events, for example – a time series of interferometric phase, closure phase, and decorrelation phase (through the algorithm presented in Chapter 5) could be made. Observation of unique closure phase signatures as a function of time since initiation of a drydown event, as well as systematic differences between L-band and S-band observations, would provide a powerful validation of the PCIM model proposed here.

Successful validation of soil moisture estimates from the PCIM model would require a combination of in-situ measurements of soil moisture and independent, simultaneous retrieval estimates of soil moisture from a radiometer such as SMAP [Colliander et al., 2017; Grassotti et al., 2003]. Direct comparison to in-situ measurements, and cross-calibration with existing soil moisture retrieval algorithms would be the most robust methods of assessing the fidelity of closure phase-based soil moisture estimates. [Narvekar et al., 2013; Al-Yaari et al., 2017; Al-Yaari et al., 2019]. Furthermore, overlapping datasets of radiometric and active radar observations would allow for error quantification of multiple retrieval algorithms using the statistical method of triple-collocation [McColl et al., 2014]. Finally, the difference in spatial resolution between passive radiometric and active radar measurements can be as large as a factor of 100, providing a unique opportunity to compare how soil moisture varies across spatial scales, which is of paramount importance for regional hydrologic modeling, watershed characterization, and climate forecasting [McCabe and Wood, 2006].

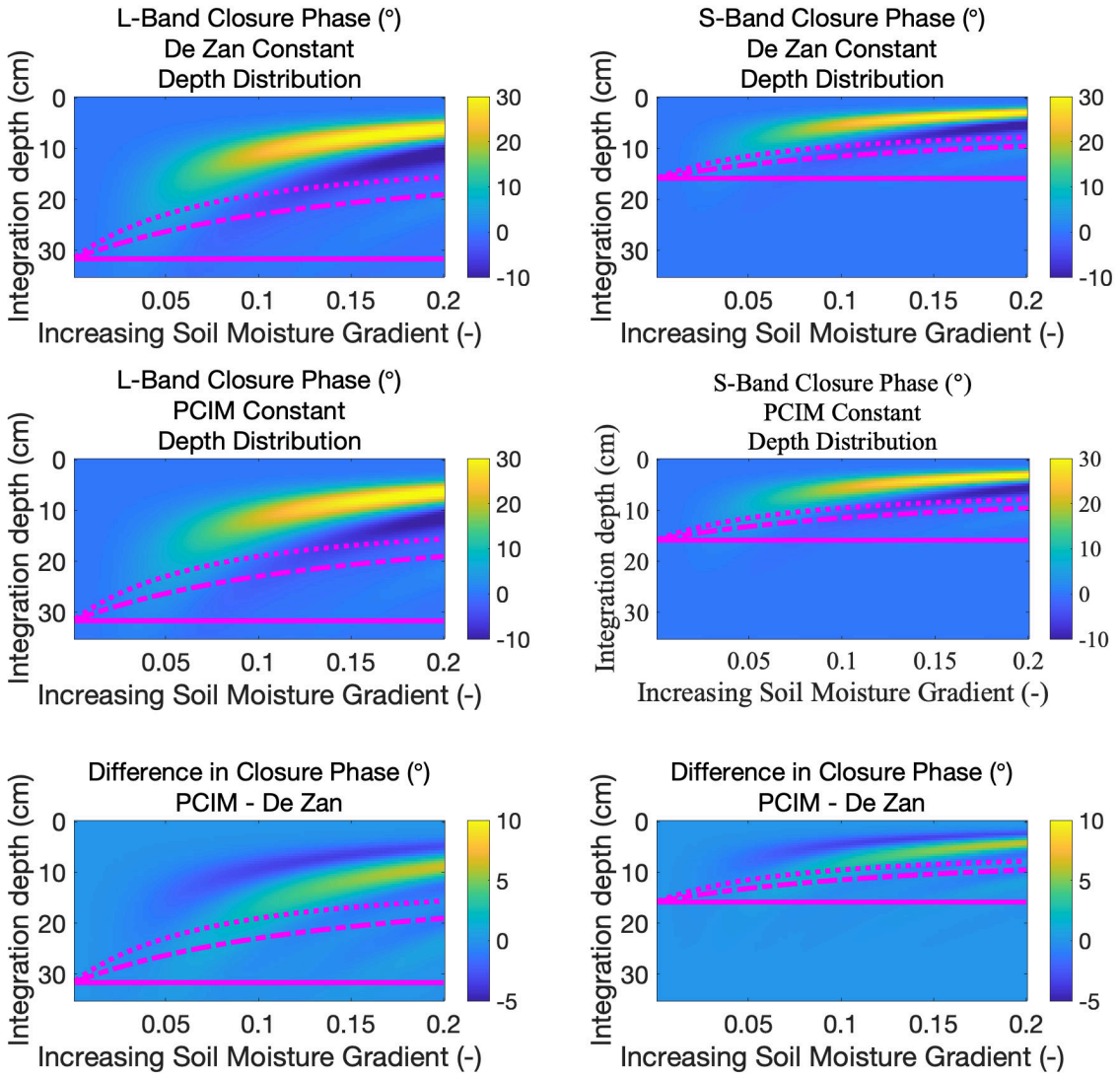

Figure 6.7: Numerical simulations of closure phase as a function of integration depth and soil moisture gradient (under the assumption of a monotonic gradient across 3 SAR images) for a constant vertical distribution of scatterers at L-band (left column) and S-band (right column). First row: De Zan model. Second row: PCIM model. Third row: difference between PCIM and De Zan model. Penetration depth for each image shown in magenta (solid: Image 1, dot-dashed: Image 2, dotted: Image 3).

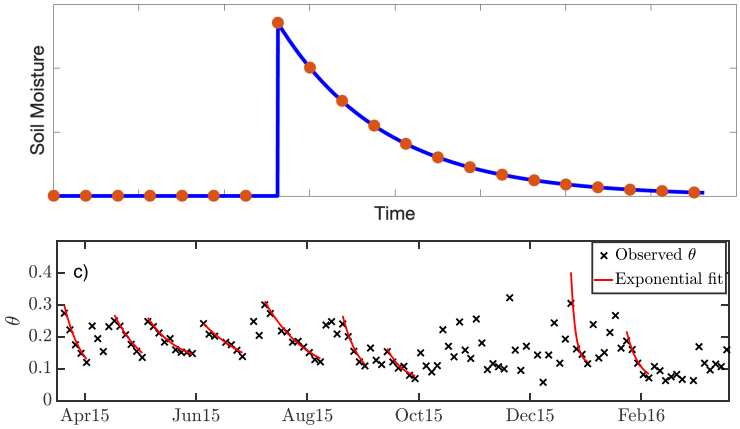

Figure 6.8: Top: Depiction of an idealized time-series application test for the proposed closure phase model. The blue line represents a time series of soil moisture for an impulse event such as a rain storm or agricultural flood event; soil moisture is constant until the impulse event, and gradually decays to its previous value. If several repeat SAR observations (represented as red circles) are collected over the course of the event, a dense network of closure phase triplets can be formed for different soil moisture gradients (the derivative of the blue line). Bottom: An example from SMAP-derived soil moisture values displaying this exponential behavior as the wetted soil undergoes a drydown (adapted from McColl et al. [2017].

6.5 A Preliminary Soil Moisture Retrieval Algorithm

While nonzero phase closure is fundamentally due to signal decorrelation between SAR scenes within a triplet [Michaelides et al., 2019b], there has been particular interest in relating closure phase to temporal variations in surface and near-subsurface soil moisture state [De Zan and Gomba, 2018]. We will assess the degree to which soil moisture can be retrieved using closure phase-based inversions. We demonstrate an inversion of decorrelation phase from closure phase with Sentinel-1A InSAR imagery collected during the 2018 Kilauea Eruption, and demonstrate the potential for phase closure to bias conventional geodetic time series estimates. Finally, we estimate temporal changes in soil moisture from the inferred decorrelation phase.

6.5.1 Estimating Decorrelation Phase from Closure Phase

Chapter 5 of this thesis presented an algorithm with which to estimate the component of interferometric phase that is due to signal decorrelation by exploiting subsets of closure phase triplets [Michaelides et al., 2019b]. Because closure phase is invariant to propagational phase terms, Equation 5.4 can be re-expressed as:

$$\xi_{123} = \phi^d_{12} + \phi^d_{23} - \phi^d_{13} \tag{6.32}$$

where $\hat{\phi}_{ij}^{d}$ are decorrelation phase terms. For a series of coregistered SAR scenes, a system of linear equations of the form of Equation 6.32 can be constructed and inverted via a singular value decomposition (SVD) to solve for the best-fitting estimate of decorrelation phase values for each interferogram pair:

$$\xi = B\phi^{d} \qquad \phi_{est}^{d} = B^{\dagger}\xi \tag{6.33}$$

where $B^{\dagger}$ is the pseudo-inverse of B and ϕ_{est}^{d} is the best-fitting estimate of the decorrelation phase. An example is demonstrated in Figure 6.9. Sentinel-1A data was collected over Hawaii from 4/11/2018 - 11/01/2018 during the 2018 Kilauea eruption. The first row of Figure 6.9 displays the average coherence and a single closure phase triplet formed from the 04/11/2018-04/23/2018-09/20/2018 scenes. The following rows shows the three corresponding interferogram pairs, and their associated solutions for decorrelation phase after application of the SVD algorithm.

The separation of the surface deformation associated with the Kilauea eruption is evident in the decorrelation phase. Similarly, there are clear spatial patterns within the decorrelation phase associated with vegetation cover, various lava channels within Hawaii Volcanoes National Park, and along the slopes of Mt. Kilauea.

6.5.2 Soil Moisture Gradient Estimation

After estimating the decorrelation phase associated with each interferogram pair, we convert the estimates of decorrelation phase into temporal variations of soil moisture. To do so, it is necessary to have both an interferometric model that incorporates variations in soil moisture (and therefore dielectric permittivity of the near subsurface), as well as a model for the vertical distribution of scattering elements that give rise to SAR backscatter within each surface resolution element [De Zan et al., 2014]. We compare the interferometric model derived in De Zan et al. [2014] with the 'PCIM' model.

The impact of variable soil moisture on interferometric phase depends upon both the spatial distribution and autocovariance function of the scatterers that give rise to SAR backscatter. As illustrated in Figure 6.10, the assumption of a constant scatterer distribution with depth (constant) vs. an exponential distribution with depth (exponential), and the assumption of uncorrelated scatterers with Dirac delta-like autocorrelations (-) vs. a partially-correlated correlated distribution of scatterers with exponential autocorrelations (PCIM) can modify the sensitivity of interferometric phase to changes in soil moisture.

Even modest differences, such as prescribing a constant depth-distribution vs. an exponential depth-distribution (with a decay constant of 0.14 cm^{-1}), or an exponential autocorrelation with a correlation length of 3.6 cm can change the sensitivity of interferometric phase to soil moisture by

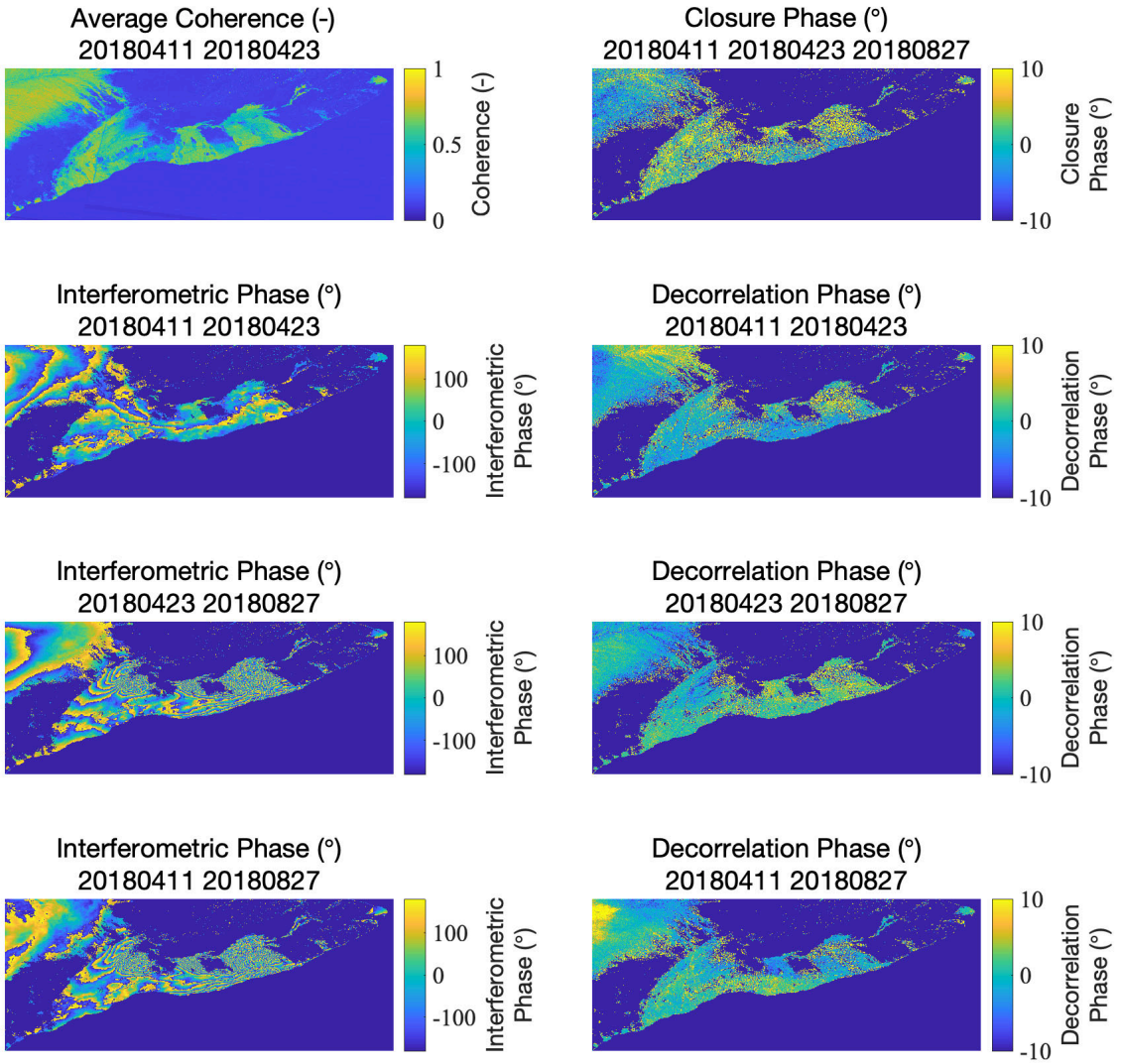

Figure 6.9: Demonstration of decorrelation phase estimates from closure phase. Top row: average coherence (left), closure phase triplet 04/11/2018-04/23/2018-08/27/2018 (right). Following rows: 3 possible interferometric pairs corresponding to closure phase triplet 04/11/2018-04/23/2018-08/27/2018 (left) and their associated decorrelation phase estimates (right). Note that decorrelation phase is insensitive to propagational phase terms (atmospheric noise and surface deformation), but is sensitive to surface features (lava flow channels in Hawaii Volcanoes National Park, bare soil, and lightly vegetated surfaces).

a factor of 3 or more. For physically realistic estimates of soil moisture from interferometric phase, it is therefore necessary to have a reasonably accurate model of the scattering statistics of an area of interest.

We estimate the change in soil moisture between the 04/23/2018 and 08/27/2018 scenes from the associated decorrelation phase estimate for the different sensitivities displayed in Figure 6.10. A lower sensitivity of the interferometric model to soil moisture results in a larger inferred dynamic range of soil moisture gradients. In this particular example, the exponential depth-distribution of scatterers with exponential autocorrelation functions seems to give the most physically realistic estimate of soil moisture gradients.

6.6 Concluding Remarks and Summary

We have presented here a more general derivation of the interferometric scattering model first proposed in De Zan et al. [2014]. Explicitly considering both volume scattering and the statistical autocorrelation of stochastically rough surfaces, results in a more general interferometric model that is valid for a range of scattering distributions, rough surfaces, and volume scattering regimes. Neglecting to include more realistic scattering autocorrelation functions can result in a systematic over-estimate of the interferometric and closure phase associated with variable dielectric permittivity, potentially biasing phase-based soil moisture retrievals. Additionally, phase changes due to variable dielectric permittivity are shown to be frequency-dependent when more realistic vertical scattering distributions are considered.

While it is relatively straightforward to derive the general form of the PCIM interferometric model, choosing the most appropriate statistics to represent the vertical distribution of scatterers and their associated autocorrelation function is less obvious. Constant vertical distributions [De Zan et al., 2014; De Zan and Gomba, 2018] and linear depth distributions [Zwieback et al., 2015b] have been previously used for their simplicity and closed form expressions for the complex correlation, although these modeling results suggest that they may be more appropriate as upper-bound estimates. While Gaussian and exponential distributions yield closer agreement to model simulations, their analytical expressions are more complex (see Appendix D), and they require more prescribed parameters. Discrete sums of scattering elements, and scattering volumes with finite integration depths, similarly display good agreement with modeling results, but their model complexity may limit their applicability. More rigorous comparisons between different scattering distributions with modeling results and real data is needed.

We have presented a simple theoretical experiment to validate the PCIM model for soil moisture retrievals using close phase observations. By exploiting the dependence of the model on soil moisture gradients – as well as the frequency dependence of the model – we propose to investigate precipitation drydown events, which have been previously shown to display exponential behavior in soil moisture

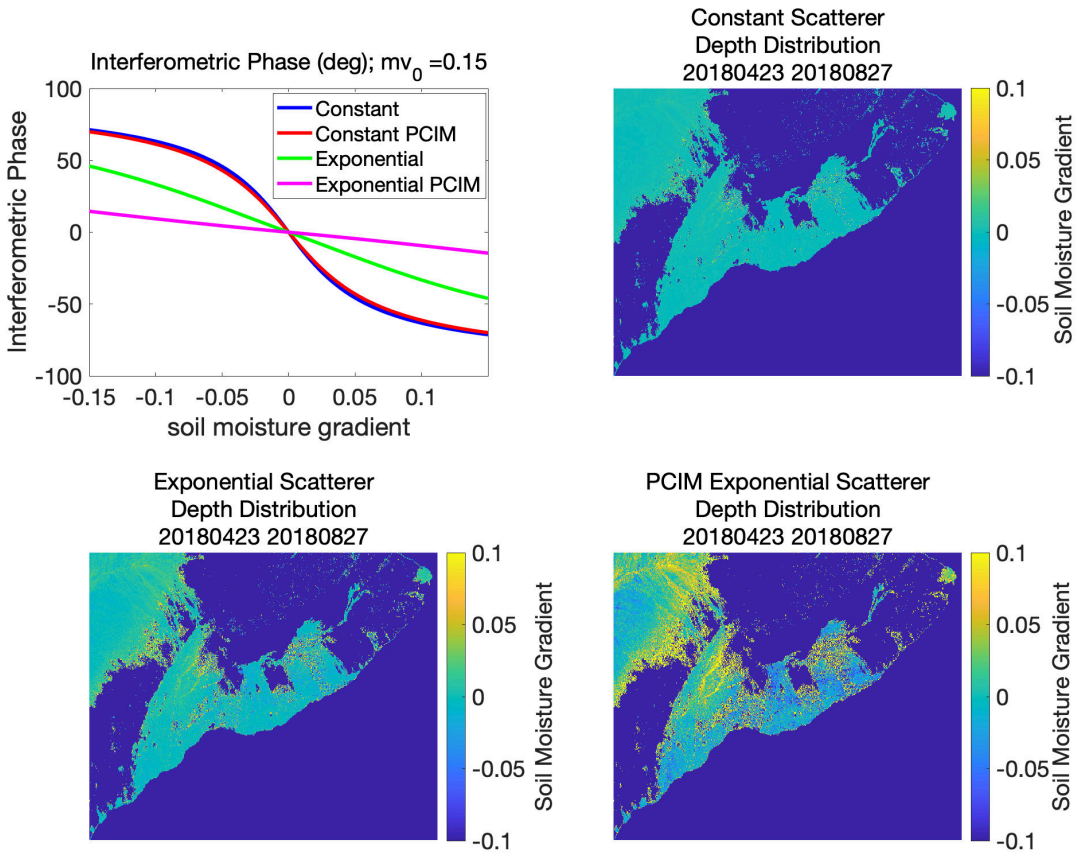

Figure 6.10: Estimation of soil moisture gradients from decorrelation phase estimates. Top left: sensitivity of different interferometric models and scatterer distributions to changes in soil moisture. Top right: soil moisture estimation for a constant depth-distribution of scatterers and the interferometric model from De Zan et al. [2014]. Bottom left: soil moisture estimation for an exponential depth-distribution of scatterers (decay constant of 0.14 cm^{-1}) and the interferometric model from De Zan et al. [2014]. Bottom right: soil moisture estimation for an exponential depth-distribution of scatterers (decay constant of 0.14 cm^{-1}), an exponential scatterer autocorrelations with a 3.6 cm correlation length.

content as a function of time. Resolving time-dependent differences in closure phase associated with a drydown would validate the model's dependence upon the measured soil moisture gradient. Frequency dependence of closure phase values would similarly be consistent with the PCIM model, and might be used to infer differences in soil moisture as a function of sensing depth, as well as determine the vertical profile of scattering elements giving rise to backscatter. The upcoming NISAR mission is an excellent candidate for such a validation experiment.

We have also presented a preliminary, demonstrative soil moisture retrieval scheme based upon closure phase and decorrelation phase observations. In order to develop dedicated soil moisture retrieval algorithms that utilize interferometric closure phase and decorrelation phase, a more thorough understanding of the scattering physics that give rise to these phase terms, as well as the scattering statistics of various surface types, is necessary. The main advantage of the estimation scheme presented here over the method proposed in De Zan and Gomba 2018 [2014] is its computational efficiency, reliance solely on interferometric phase as an observable (i.e. does not use coherence magnitude as part of the inversion), and its ability to be incorporated relatively seamlessly into conventional InSAR time series workflows. However, we do not claim at present that this estimation scheme is superior to the one presented in De Zan and Gomba 2018; further comparison of the two methods is warranted. At present, we note that this proposed method is both computationally efficient and provides physically plausible estimates of soil moisture variations from InSAR decorrelation phase; more thorough analysis is needed to determine its accuracy. Additionally, closure phase is sensitive to other forms of systematic decorrelation, such as changes in vegetation canopy water content. These additional decorrelation terms can confound any soil moisture signal that might be contained within a closure phase observation, necessitating a more thorough understanding of other forms of systematic InSAR decorrelation sources.

Chapter 7

Conclusion

7.1 Summary

In this thesis, we have introduced techniques for quantifying permafrost processes, soil moisture, and surface scattering properties with InSAR. We demonstrated that seasonal thaw subsidence and active layer thickness can be successfully estimated in discontinuous permafrost environments. Furthermore, we estimated the long-term behavior of permafrost that has been affected by wildfire, and provided bounds on post-fire permafrost recovery timescales. These results both broaden the known range of permafrost environments that can be successfully monitored with InSAR, and provide a novel method for studying permafrost and wildfire interactions.

We proposed a novel algorithm that utilizes InSAR closure phase observations to estimate the component of interferometric phase that is due to signal decorrelation. We demonstrated this algorithm over a large subsiding portion of California's Central Valley, showing that the decorrelation phase component – due to temporal variations in surface scattering properties such as crop growth and soil moisture – can be successfully separated from the deformation component of the InSAR phase signal. We demonstrated that uncertainty due to signal decorrelation on the order of mm/yr can be separated from the deformation signal; such errors can be of the same order of magnitude as the signal of interest in several InSAR applications.

Lastly, we derived a physics-based interferometric SAR imaging model that considers the effects of variable soil moisture and surface scattering properties by explicitly incorporating the relevant physics into the imaging model. We compared this imaging model to previously-proposed imaging models and numerical simulations, and discussed the major differences between our model and other imaging models. Finally, we discussed the potential that our proposed model has for resolving soil moisture at fine spatial resolution, and presented a preliminary procedure for quantifying temporal changes in soil moisture that relies on a synthesis of the work presented in Chapters 5 and 6. We hope that the work presented in this thesis will be helpful in expanding the range of physical processes

that can be regularly studied with InSAR platforms. To that end, we have identified a few areas of future work that are natural extensions from the work presented in this thesis.

7.2 Future Work

In Chapter 4, we demonstrated that seasonal and interannual deformation processes can be resolved by InSAR in discontinuous permafrost zones. Extending the work presented here to a region of sporadic or isolated permafrost would be valuable to ascertain the full range of permafrost environments that can be monitored with InSAR methods. Such an analysis, drawing on the results presented here, would go a long way towards implementing a framework for regional-scale permafrost monitoring efforts. Additionally, the ability to quantify post-fire permafrost behavior with InSAR is a powerful new technique. However, the large variability of both permafrost and wildfire regimes across the Arctic means that the estimates provided here are not necessarily applicable to the entire Arctic domain. Future studies of other Arctic wildfires would shed light on the full range of post-fire permafrost behavior, and provide a more complete understanding of the interactions between wildfire and permafrost within the context of a warming Arctic.

The closure phase-based algorithm presented in Chapter 5 shows promise as a method of quantifying uncertainties in conventional InSAR analyses due to signal decorrelation. In many regions, such as vegetated surfaces, wetlands, or areas that experience snow cover, signal decorrelation can preclude precise geodetic measurements with InSAR, as errors introduced by signal decorrelation can be on the same order of magnitude as the signal of interest. A more rigorous analysis of signal decorrelation errors might shed greater light on the full potential of this technique for uncertainty quantification and error mitigation. Additionally, the flexibility of the design matrix used in this technique allows for the incorporation of empirical and physics-based models of signal decorrelation, which might allow for the further separation of decorrelation phase, such as distinguishing between soil moisture variations, vegetation water content, and snow water equivalent in a permafrost environment.

In Chapter 6, we derived a physics-based SAR imaging model that incorporates the statistics of stochastically rough scattering surfaces and volumes, as well as the effect of variable dielectric permittivity due to changing soil moisture. Examination of this model and comparison with numerical simulations revealed that this model is dependent upon the statistical characteristics of the scatterers that contribute to SAR backscatter. In light of this, future research into the statistics of different scattering volumes, as well as the ability to estimate these statistics from InSAR observations, is warranted. We also introduced a preliminary method for quantifying temporal variations in soil moisture at active radar spatial resolutions by combining the results from Chapters 5 and 6. The full potential for soil moisture retrieval from decorrelation phase and closure phase has not yet been rigorously studied, however. Such an analysis is an obvious extension of this thesis, and would

provide further insight into the degree to which soil moisture can be estimated with active radar phase measurements.

Lastly, the general nature of the imaging model derived in Chapter 6 gives it explanatory power for a range of physical scattering processes beyond merely the scenario of temporally-varying soil moisture. Volume scattering elements that undergo changes in dielectric permittivity – such as vegetation canopies, melting snow packs, and thawing permafrost active layers – can all be modeled with our proposed imaging model. The range of physical processes that can give rise to systematic decorrelation phase and nonzero closure phase is potentially vast, and should be studied in greater detail. Such analysis would also require a more thorough understanding of the statistics of scatterers, which may be unique to each physical process of interest.

For ease of demonstration, we analyzed InSAR data with the algorithm proposed in Chapter 5 and the imaging model derived in Chapter 6 over California's Central Valley and Hawaii's Mt. Kilauea – areas that have been extensively studied with InSAR and exhibit some areas of bare surfaces that maintain temporal coherence. Testing these techniques in more complicated environments, such as permafrost regions, is another obvious extension of this thesis. Initial results show great promise, with variations in surface scattering properties due to seasonal permafrost processes observed, as well as systematic changes in closure phase, decorrelation phase, and inferred scattering properties observed between wildfire-affected and unaffected permafrost. The ongoing nature of this research precluded its inclusion in this thesis, but we hope to continue refining the techniques presented in this thesis, and expand the range of physical processes that can be studied with InSAR.

Appendix A

ReSALT Processing Methodology Employed in Chapter 4

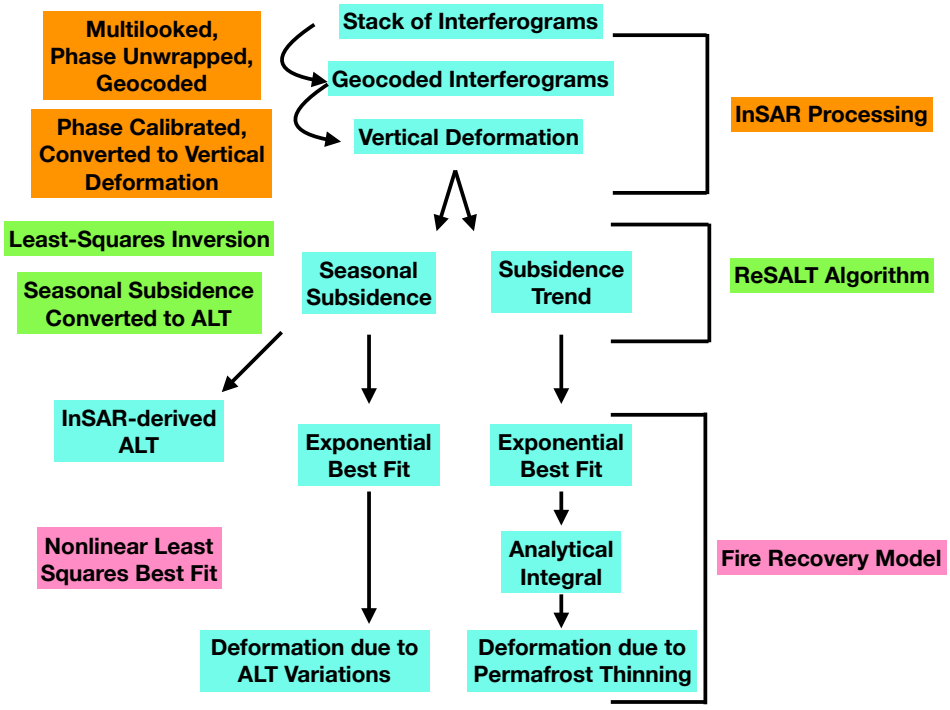

Figure A.1: Diagram of processing applied to InSAR data as described in Section 4.2. Data at various levels of processing are in blue; processing steps described in Section 4.2.1 are in orange; processing steps described in Section 3.6.1 are in green; processing steps described in Section 4.2.2 are in pink.

Appendix B

InSAR Scene Pairs Used in Chapter 4

Interferogram #	Date 1	Date 2	Scene 1	Scene 2	Time Span (days)	Perpendicular Baseline (m)
1	20070812	20070927	ALPSRP082461220	ALPSRP089171220	46	389
2	20070812	20071228	ALPSRP082461220	ALPSRP102591220	138	2514
3	20070812	20080814	ALPSRP082461220	ALPSRP136141220	368	-5003
4	20070812	20100102	ALPSRP082461220	ALPSRP209951220	874	-27
5	20070927	20071228	ALPSRP089171220	ALPSRP102591220	92	1544
6	20070927	20100102	ALPSRP089171220	ALPSRP209951220	828	-997
7	20071228	20080212	ALPSRP102591220	ALPSRP109301220	46	1034
8	20071228	20081230	ALPSRP102591220	ALPSRP156271220	368	-4408
9	20071228	20090214	ALPSRP102591220	ALPSRP162981220	414	-3527
10	20071228	20100102	ALPSRP102591220	ALPSRP209951220	736	-1137
11	20080212	20100102	ALPSRP109301220	ALPSRP209951220	690	-2171
12	20081230	20090214	ALPSRP156271220	ALPSRP162981220	46	881
13	20081230	20100102	ALPSRP156271220	ALPSRP209951220	368	3271
14	20090214	20100102	ALPSRP162981220	ALPSRP209951220	322	2390

Table B.1: InSAR scene pairs used in Chapter 4.

Appendix C

Variable Refractive Angle Sensitivity Analysis

Consider the viewing geometry illustrated in C.1. A SAR signal at time t_1 impinges upon a horizontal surface at depth $z = 0$ and horizontal position $x = 0$. The transmitted ray path is refracted, where the angle of the refracted ray path with respect to the normal of the surface is modified according to Snell's Law:

$$\sqrt{\epsilon_0} \sin\theta_0 = \sqrt{\epsilon_1} \sin\theta_1 \tag{C.1}$$

where ϵ_0 is the dielectric permittivity of free space, ϵ_1 is the real component of the complex dielectric permittivity of the subsurface (we assume $\epsilon_1 > \epsilon_0$ and is spatially uniform), and θ_0 and θ_1 are the incidence angle and refraction angle, respectively. As the refracted ray path penetrates the subsurface, it intercepts horizontal interfaces at progressively larger distances from the impingement point at $x = 0$:

$$x_1(z) = z \tan\theta_1 \tag{C.2}$$

where the horizontal distance is linear with depth z. Combining Equations C.1 and C.2, Equation C.2 can be rewritten as:

$$x_1 = z \tan(\sin^{-1}(\frac{\sqrt{\epsilon_0} \sin\theta_0}{\sqrt{\epsilon_1}})) \tag{C.3}$$

Consider a separate SAR signal at time t_2 that impinges upon the same point of the surface. Now, however, the real component of the dielectric permittivity of the subsurface has changed to ϵ_2. This change in dielectric permittivity results in a different refraction angle, and therefore the horizontal component of the refracted ray path diverges from the impingement point at a different linear rate:

$$x_2 = z \tan(\sin^{-1}(\frac{\sqrt{\epsilon_0}\sin\theta_0}{\sqrt{\epsilon_2}})) \tag{C.4}$$

assuming that $\epsilon_2 > \epsilon_1$, then $\theta_2 < \theta_1$, and the second refracted ray path diverges from $x = 0$ less than the first ray path. The difference between the horizontal interception of these two paths, which we call the horizontal offset χ, is:

$$\chi_{12} = x_2 - x_1 \tag{C.5}$$

Combining Equations C.3 and C.4 with C.5, the horizontal offset can be re-expressed as:

$$\chi_{12} = z[\tan(\sin^{-1}(\frac{\sqrt{\epsilon_0}\sin\theta_0}{\sqrt{\epsilon_2}})) - \tan(\sin^{-1}(\frac{\sqrt{\epsilon_0}\sin\theta_0}{\sqrt{\epsilon_1}}))] \tag{C.6}$$

the horizontal offset is linear with respect to depth, and the rate at which it changes with depth is related to to incidence angle and the dielectric contrast of the subsurface between the two image acquisitions. We can re-express the real component of the dielectric permittivity at acquisition 2 as:

$$\epsilon_2 = \epsilon_1 + \Delta\epsilon \tag{C.7}$$

where the dielectric contrast $\Delta\epsilon$ can be positive or negative. Equation C.6 then becomes:

$$\chi_{12} = z[\tan(\sin^{-1}(\frac{\sqrt{\epsilon_0}\sin\theta_0}{\sqrt{\epsilon_1 + \Delta\epsilon}})) - \tan(\sin^{-1}(\frac{\sqrt{\epsilon_0}\sin\theta_0}{\sqrt{\epsilon_1}}))] \tag{C.8}$$

As stated above, the horizontal offset is linear with depth, and therefore the partial derivative of the horizontal offset with respect to depth is:

$$\frac{\partial\chi_{12}}{\partial z} = \tan(\sin^{-1}(\frac{\sqrt{\epsilon_0}\sin\theta_0}{\sqrt{\epsilon_1 + \Delta\epsilon}})) - \tan(\sin^{-1}(\frac{\sqrt{\epsilon_0}\sin\theta_0}{\sqrt{\epsilon_1}})) \tag{C.9}$$

Target	Dielectric Permittivity (R)	Dielectric Permittivity (I)	Penetration Depth (cm)	Horizontal Divergence (cm)
Dry soil	2-6	0-3	6	1.5
Wet Soil	20-40	3-15	3	.25
Ice	3.-3.2	10^{-5}-10^{-2}	1366	22
Dry Snow	1-3	0-0.5	27	13
Wet Snow	2-15	0.5-2.5	12	4
Vegetation Canopy	1-1.2	10^{-4}-10^{-2}	837	108

Table C.1: Horizontal Divergence of Representative Geophysical Targets at L-band, adapted from [Cihlar and Ulaby, 1974; Stiles and Ulaby, 1981; Tomasanis, 1990; Schmugge and Jackson, 1992; Ulaby, 1985].

Similarly, the partial derivative of horizontal offset with respect to dielectric contrast is:

$$\frac{\partial \chi_{12}}{\partial \Delta\epsilon} = \frac{-z\sqrt{\epsilon_0}\sin\theta_0}{2(\epsilon_1+\Delta\epsilon)^{3/2}(\frac{-\epsilon_0\sin^2\theta_0+\epsilon_1+\Delta\epsilon}{(\epsilon_1+\Delta\epsilon)})^{3/2}} \tag{C.10}$$

Equations C.8, C.9, and C.10 can be evaluated for a range of dielectric contrasts and depths for different geophysical targets. Table C lists several such targets evaluated at L-band, as well as representative ranges of dielectric constants, autocorrelation lengths, and realistic sensing depths (on the order of the penetration depth). Clearly, significant horizontal offsets are physically realistic for a range of geophysical scattering volumes.

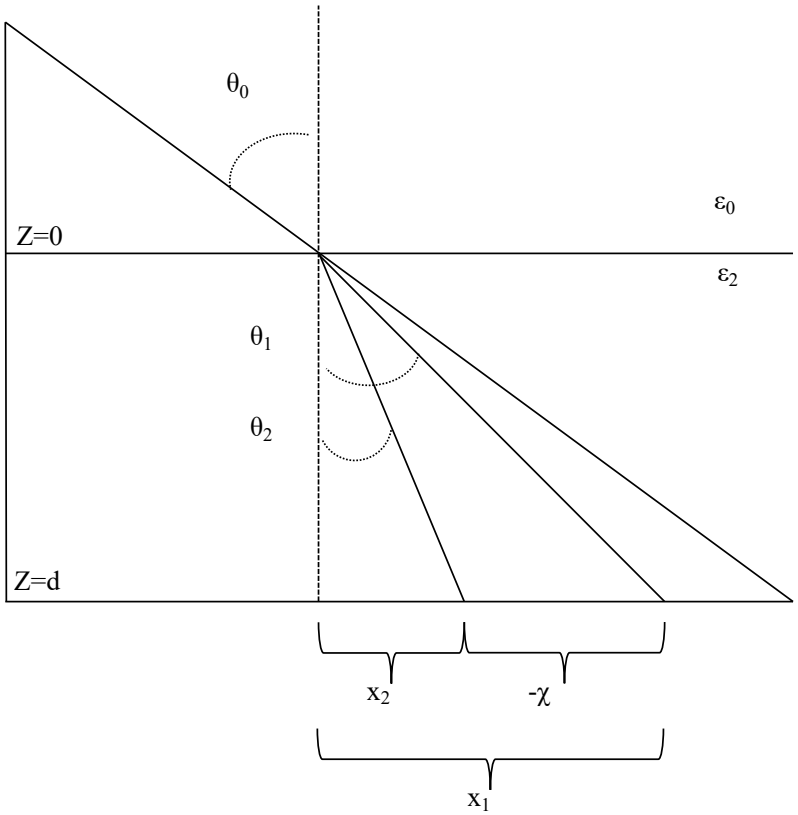

Figure C.1: Refraction through a volume with a time-varying bulk dielectric permittivity results in a varying angle of refraction. This in turn causes a horizontal divergence of the refracted raypaths, which increases with depth.

Appendix D

Vertical Scatterer Distribution Analytical Solutions

Beginning with Equation 6.11, if the vertical distribution of scatterers is taken to be constant with depth $f(z) = f_0$, than Equation 6.11 can be written as:

$$I_{12} = \int_0^\infty f_0 e^{-i2k_0(r_1-r_2)} e^{-i2(K_{z1}-k_{z2}^*)z} e^{i2k_x \frac{\partial \chi}{\partial z} z} dz \tag{D.1}$$

This is analogous to the model derived in [De Zan et al., 2014], with an additional phase term associated with the horizontal divergence of the refracted raypaths. The analytical solution of Equation D.1 is:

$$I_{12} = \frac{-if_0 e^{-i2k_0(r_1-r_2)}}{2(k_{z1} - k_{z2}^* - k_x \frac{\partial \chi}{\partial z})} \tag{D.2}$$

This is analogous to the solution in [De Zan et al., 2014], with an additional term that 'damps out' the phase excursion do to the variable vertical wave velocity (note that $\frac{\partial \chi}{\partial z}$ is constant with respect to depth, and depends on the dielectric contrast between image acquisitions). The solution for an exponential distribution of scatterers follows immediately:

$$I_{12} = \frac{f_0 e^{-i2k_0(r_1-r_2)}}{2i(k_{z1} - k_{z2}^* - k_x \frac{\partial \chi}{\partial z}) + \sigma} \tag{D.3}$$

where σ is the extinction coefficient of the scattering distribution.

If we relax the assumption of idealized scatterer autocorrelations, we can derive an analytical solution for the complex coherence. We assume that scatterers are distributed constantly as a function of depth $f(z) = f_0$, and we assume a Gaussian autocorrelation of horizontal scattering interfaces in the form:

$$R(\chi(z)) = R(\frac{\partial \chi}{\partial z} z) = e^{-\frac{(\frac{\partial \chi}{\partial z} z)^2}{2L^2}} \tag{D.4}$$

where L is the correlation length of the interface. Equation 6.11 then becomes:

$$I_{12} = \int_0^\infty f_0 e^{-\frac{(\frac{\partial \chi}{\partial z} z)^2}{2L^2}} e^{-i2k_0(r_1 - r_2)} e^{-i2(k_{z1} - k_{z2}^*)z} e^{i2k_x \frac{\partial \chi}{\partial z} z} dz \tag{D.5}$$

which has an analytical solution of the form:

$$I_{12} = \frac{i f_0 L}{\frac{\partial \chi}{\partial z}} \sqrt{\frac{\pi}{2}} e^{-i2k_0(r_1 - r_2)} \cdot e^{-(\frac{2L^2(-k_{z1} + k_{z2}^* + k_x \frac{\partial \chi}{\partial z})^2}{(\frac{\partial \chi}{\partial z})^2})} \cdot erfi(\frac{L^2(2k_{z1} - 2k_{z2}^* - 2k_x \frac{\partial \chi}{\partial z}) - i(\frac{\partial \chi}{\partial z})^2 z}{\sqrt{2} L \frac{\partial \chi}{\partial z}}) + C \tag{D.6}$$

where C is an integration constant. When evaluated from $z = 0$ to $z = \infty$, Equation D.6 reduces to:

$$I_{12} = \frac{f_0 L}{\frac{\partial \chi}{\partial z}} \sqrt{\frac{\pi}{2}} e^{-i2k_0(r_1 - r_2)} \cdot e^{-(\frac{2L^2(-k_{z1} + k_{z2}^* + k_x \frac{\partial \chi}{\partial z})^2}{(\frac{\partial \chi}{\partial z})^2})} \cdot [1 - i \; erfi(\frac{\sqrt{2} L (k_{z1} - k_{z2}^* - k_x \frac{\partial \chi}{\partial z})}{\frac{\partial \chi}{\partial z}})] \tag{D.7}$$

Appendix E

Effects of Nonzero Perpendicular Baseline

As shown in the main text, the interferometric phase is proportional to a linear combination of the contrast in complex vertical wavenumber, as well as horizontal divergence of the refracted ray paths:

$$I_{12} \propto e^{-\frac{i4\pi}{\lambda}(x_1 \sin\theta_{01} - x_2 \sin\theta_{02})} e^{-\frac{i4\pi}{\lambda}(z_1\sqrt{\epsilon_1}\cos\theta_{r1} - z_2\sqrt{\epsilon_2}\cos\theta_{r2})} \tag{E.1}$$

Consider first the phasor associated with the horizontal wavenumber:

$$e^{-\frac{i4\pi}{\lambda}(x_1 \sin\theta_{01} - x_2 \sin\theta_{02})} \tag{E.2}$$

Any nonzero variations in the component of the spatial baseline perpendicular the the LOS will result in an incremental change in the incidence angle of the SAR signal [Zebker and Villasenor, 1992]. We can furthermore relate x_1 and x_2 with their horizontal offset χ:

$$\begin{aligned} \theta_{02} &= \theta_{01} + \Delta\theta \\ x_2 &= x_1 + \chi \end{aligned} \tag{E.3}$$

Inserting Equations E.3 into Equation E.2 yields:

$$e^{-\frac{i4\pi}{\lambda}(x_1 \sin\theta_{01} - (x_1+\chi)\sin(\theta_{01}+\Delta\theta))} \tag{E.4}$$

For small variations in the incidence angle (i.e. $\Delta\theta \ll 1$), then the following approximation can be made:

$$\begin{aligned} \sin(\theta_{01} + \Delta\theta) &= \sin\theta_{01}\cos\Delta\theta + \cos\theta_{01}\sin\Delta\theta \\ &if\ \Delta\theta \ll 1 \\ \sin(\theta_{01} + \Delta\theta) &\approx \sin\theta_{01} + \Delta\theta\cos\theta_{01} \end{aligned} \tag{E.5}$$

and Equation E.4 reduces to:

$$e^{\frac{i4\pi}{\lambda}\chi\sin\theta_{01}} e^{\frac{i4\pi}{\lambda}x_2\Delta\theta\cos\theta_{01}} \approx e^{\frac{i4\pi}{\lambda}\chi\sin\theta_{01}} e^{\frac{i4\pi}{\lambda}\frac{x_2|B|\cos^2\theta_{01}}{r}} \tag{E.6}$$

where $|B|$ is the magnitude of the spatial baseline, and r is the range from the spacecraft to the illuminated target. We can see that the phasor associated with the horizontal wavenumber is composed of two terms: a term related to the horizontal divergence of the refracted ray paths that was derived in Appendix C, and a term proportional to the incremental change in the incidence angle associated with a nonzero spatial baseline.

We can similarly analyze the vertical component of the interferometric phasor:

$$e^{-\frac{i4\pi}{\lambda}(z_1\sqrt{\epsilon_1}\cos\theta_{r1} - z_2\sqrt{\epsilon_2}\cos\theta_{r2})} \tag{E.7}$$

where θ_r is the refracted ray path angle with respect to the normal (determined via Snell's Law refraction). We can linearly approximate the incremental change in the refracted raypath angle as:

$$\begin{aligned} \theta_r &= \sin^{-1}\left(\frac{\sqrt{\epsilon_0}\sin\theta_0}{\sqrt{\epsilon_r}}\right) \\ \theta_{r2} &= \theta_{r1} + \Delta\theta_r \end{aligned} \tag{E.8}$$

and relate the vertical depths z_1 and z_2 with their vertical offset:

$$z_2 = z_1 + \zeta \tag{E.9}$$

and we can approximate linear variations in the dielectric permittivity as:

$$\sqrt{\epsilon_2} \approx \sqrt{\epsilon_1} + \frac{\Delta\epsilon}{2\sqrt{\epsilon_1}} \tag{E.10}$$

where $\Delta\epsilon$ is the incremental change in the real component of the complex dielectric permittivity. Inserting Equations E.8-E.10 into Equation E.7 yields:

$$e^{-\frac{i4\pi}{\lambda}(z_1\sqrt{\epsilon_1}\cos\theta_{r1} - (z_1+\zeta)(\sqrt{\epsilon_1}+\frac{\Delta\epsilon}{2\sqrt{\epsilon_1}})\cos(\theta_{r1}+\Delta\theta_r))} \tag{E.11}$$

which can be rearranged as:

$$e^{-\frac{i4\pi}{\lambda}(\sqrt{\epsilon_1}-\sqrt{\epsilon_2})z_1\cos\theta_{r1}} e^{-\frac{i4\pi}{\lambda}\sqrt{\epsilon_2}\zeta\cos\theta_{r1}} e^{-\frac{i4\pi}{\lambda}\sqrt{\epsilon_2}z_2\Delta\theta_r\sin\theta_{r1}} \tag{E.12}$$

We can see that, similar the horizontal phasor, the vertical phasor is composed of: 1) a term proportional to the dielectric contrast between acquisitions, 2) a term proportional to the vertical offset (which is zero-mean for most stationary stochastic processes), and 3) a term proportional to the incremental change in the incidence angle associated with a nonzero spatial baseline. For small baseline magnitudes relative to the range from the sensor to the target, Equation E.12 is approximately:

$$e^{-\frac{i4\pi}{\lambda}(\sqrt{\epsilon_1}-\sqrt{\epsilon_2})z_1\cos\theta_{r1}} e^{-\frac{i4\pi}{\lambda}\sqrt{\epsilon_2}\zeta\cos\theta_{r1}} e^{-\frac{i4\pi}{\lambda}\frac{\sqrt{\epsilon_2}z_2|B|\cos\theta_{01}\sin\theta_{r1}}{r}} \tag{E.13}$$

For modern spaceborne SAR platforms with tight orbital control (such as the Sentinel constellation and the upcoming NISAR mission), the ratio of the spatial baseline to the range is small enough that the phasor terms proportional to the baseline in E.6 and E.13 are negligible compared to the other phasor terms.

Bibliography

[Agram, 2010] Agram, P. (2010). Persistent scatterer interferometry in natural terrain. *PhD thesis, Stanford University, Stanford, California*.

[Agram and Simons, 2015] Agram, P. S. and Simons, M. (2015). A noise model for insar time series. *Journal of Geophysical Research: Solid Earth*, 120(4):2752–2771.

[Al-Yaari et al., 2019] Al-Yaari, A., Wigneron, J.-P., Dorigo, W., Colliander, A., Pellarin, T., Hahn, S., Mialon, A., Richaume, P., Fernandez-Moran, R., Fan, L., Kerr, Y., and Lannoy, G. D. (2019). Assessment and inter-comparison of recently developed/reprocessed microwave satellite soil moisture products using ismn ground-based measurements. *Remote Sensing of Environment*, 224:289 – 303.

[Al-Yaari et al., 2017] Al-Yaari, A., Wigneron, J.-P., Kerr, Y., Rodriguez-Fernandez, N., O'Neill, P., Jackson, T., Lannoy, G. D., Bitar, A. A., Mialon, A., Richaume, P., Walker, J., Mahmoodi, A., and Yueh, S. (2017). Evaluating soil moisture retrievals from esa's smos and nasa's smap brightness temperature datasets. *Remote Sensing of Environment*, 193:257 – 273.

[Barrett et al., 2013] Barrett, B., Whelan, P., and Dwyer, E. (2013). Detecting changes in surface soil moisture content using differential sar interferometry. *International Journal of Remote Sensing*, 34(20):7091–7112.

[Bekaert et al., 2015] Bekaert, D. P. S., Hooper, A., and Wright, T. J. (2015). A spatially variable power law tropospheric correction technique for insar data. *Journal of Geophysical Research: Solid Earth*, 120(2):1345–1356.

[Berardino et al., 2002] Berardino, P., Fornaro, G., Lanari, R., and Sansosti, E. (2002). A new algorithm for surface deformation monitoring based on small baseline differential sar interferograms. *IEEE Transactions on Geoscience and Remote Sensing*, 40(11):2375–2383.

[Bindlish and Barros, 2000] Bindlish, R. and Barros, A. P. (2000). Multifrequency soil moisture inversion from sar measurements with the use of iem. *Remote Sensing of Environment*, 71(1):67 – 88.

[Blackburn et al., 2019] Blackburn, L., Pesce, D. W., Johnson, M. D., Wielgus, M., Chael, A. A., Christian, P., and Doeleman, S. S. (2019). Closure statistics in radio interferometric data.

[Bockheim and Hinke, 2007] Bockheim, J. G. and Hinke, K. M. (2007). The importance of "deep" organic carbon in permafrost-affected soils of arctic alaska. *Soil Science Society of America Journal*.

[Bras, 1990] Bras, R. L. (1990). *Hydrology : an introduction to hydrologic science*. Addison-Wesley.

[Bret-Harte et al., 2013] Bret-Harte, M. S., Mack, M. C., Shaver, G. R., Huebner, D. C., Johnston, M., Mojica, C. A., and Reiskind, J. A. (2013). The response of arctic vegetation and soils following an unusually severe tundra fire. *Philosophical Transactions of the Royal Society B: Biological Sciences*, 368(1624).

[Brown et al., 2015] Brown, D. R. N., Jorgenson, M. T., Douglas, T. A., Romanovsky, V. E., Kielland, K., Hiemstra, C., Euskirchen, E. S., and Ruess, R. W. (2015). Interactive effects of wildfire and climate on permafrost degradation in alaskan lowland forests. *Journal of Geophysical Research: Biogeosciences*, 120(8):1619–1637. 2015JG003033.

[Brutsaert, 1982] Brutsaert, W. (1982). *Evaporation Into the Atmosphere*. Springer, Netherlands.

[Burns, 1964] Burns, J. J. (1964). Pingos in the yukon-kuskokwim delta, alaska: Their plant succession and use by mink. *Arctic*, 17(3):203–210.

[Callaghan et al., 2010] Callaghan, T. V., Bergholm, F., Christensen, T. R., Jonasson, C., Kokfelt, U., and Johansson, M. (2010). A new climate era in the sub-arctic: Accelerating climate changes and multiple impacts. *Geophysical Research Letters*, 37(14).

[Chael et al., 2018] Chael, A. A., Johnson, M. D., Bouman, K. L., Blackburn, L. L., Akiyama, K., and Narayan, R. (2018). Interferometric imaging directly with closure phases and closure amplitudes. *The Astrophysical Journal*, 857(1):23.

[Chen et al., 2016] Chen, A., Parsekian, A. D., Schaefer, K., Jafarov, E., Panda, S., Liu, L., Zhang, T., and Zebker, H. (2016). Ground-penetrating radar-derived measurements of active-layer thickness on the landscape scale with sparse calibration at Toolik and Happy Valley, Alaska. *Geophysics*, 81(2):H9–H19.

[Chen and Zebker, 2001] Chen, C. W. and Zebker, H. A. (2001). Two-dimensional phase unwrapping with use of statistical models for cost functions in nonlinear optimization. *J. Opt. Soc. Am. A*, 18(2):338–351.

[Chen and Zebker, 2002] Chen, C. W. and Zebker, H. A. (2002). Phase unwrapping for large sar interferograms: statistical segmentation and generalized network models. *IEEE Transactions on Geoscience and Remote Sensing*, 40(8):1709–1719.

[Chen et al., 2017a] Chen, J., Knight, R., and Zebker, H. A. (2017a). The temporal and spatial variability of the confined aquifer head and storage properties in the san luis valley, colorado inferred from multiple insar missions. *Water Resources Research*, 53(11):9708–9720.

[Chen et al., 2017b] Chen, J., Knight, R., and Zebker, H. A. (2017b). The temporal and spatial variability of the confined aquifer head and storage properties in the san luis valley, colorado inferred from multiple insar missions. *Water Resources Research*, 53(11):9708–9720.

[Chen et al., 2020] Chen, J., Wu, Y., O'Connor, M., Cardenas, M., Schaefer, K., Michaelides, R., and Kling, G. (2020). Mapping active layer freeze-thaw and water storage dynamics in permafrost environments using insar (in review). *Remote Sensing of the Environment*.

[Chen et al., 2014] Chen, J., Zebker, H. A., Segall, P., and Miklius, A. (2014). The 2010 slow slip event and secular motion at kilauea, hawaii, inferred from terrasar-x insar data. *Journal of Geophysical Research: Solid Earth*, 119(8):6667–6683.

[Cihlar and Ulaby, 1974] Cihlar, J. and Ulaby, F. (1974). Dielectric properties of soils as a function of moisture content.

[Colliander et al., 2017] Colliander, A., Jackson, T., Bindlish, R., Chan, S., Das, N., Kim, S., Cosh, M., Dunbar, R., Dang, L., Pashaian, L., Asanuma, J., Aida, K., Berg, A., Rowlandson, T., Bosch, D., Caldwell, T., Caylor, K., Goodrich, D., al Jassar, H., Lopez-Baeza, E., Martínez-Fernández, J., González-Zamora, A., Livingston, S., McNairn, H., Pacheco, A., Moghaddam, M., Montzka, C., Notarnicola, C., Niedrist, G., Pellarin, T., Prueger, J., Pulliainen, J., Rautiainen, K., Ramos, J., Seyfried, M., Starks, P., Su, Z., Zeng, Y., van der Velde, R., Thibeault, M., Dorigo, W., Vreugdenhil, M., Walker, J., Wu, X., Monerris, A., O'Neill, P., Entekhabi, D., Njoku, E., and Yueh, S. (2017). Validation of smap surface soil moisture products with core validation sites. *Remote Sensing of Environment*, 191:215 – 231.

[De Zan and Gomba, 2018] De Zan, F. and Gomba, G. (2018). Vegetation and soil moisture inversion from sar closure phases: First experiments and results. *Remote Sensing of Environment*, 217:562 – 572.

[De Zan et al., 2014] De Zan, F., Parizzi, A., Prats-Iraola, P., and López-Dekker, P. (2014). A sar interferometric model for soil moisture. *IEEE Transactions on Geoscience and Remote Sensing*, 52(1):418–425.

[De Zan et al., 2015] De Zan, F., Zonno, M., and López-Dekker, P. (2015). Phase inconsistencies and multiple scattering in sar interferometry. *IEEE Transactions on Geoscience and Remote Sensing*, 53(12):6608–6616.

[Dobson and Ulaby, 1986] Dobson, M. C. and Ulaby, F. T. (1986). Preliminaly evaluation of the sir-b response to soil moisture, surface roughness, and crop canopy cover. *IEEE Transactions on Geoscience and Remote Sensing*, GE-24(4):517–526.

[Dubois et al., 1995] Dubois, P. C., van Zyl, J., and Engman, T. (1995). Measuring soil moisture with imaging radars. *IEEE Transactions on Geoscience and Remote Sensing*, 33(4):915–926.

[Entekhabi et al., 1994] Entekhabi, D., Nakamura, H., and Njoku, E. G. (1994). Solving the inverse problem for soil moisture and temperature profiles by sequential assimilation of multifrequency remotely sensed observations. *IEEE Transactions on Geoscience and Remote Sensing*, 32(2):438–448.

[Entekhabi et al., 2010] Entekhabi, D., Njoku, E. G., O'Neill, P. E., Kellogg, K. H., Crow, W. T., Edelstein, W. N., Entin, J. K., Goodman, S. D., Jackson, T. J., Johnson, J., Kimball, J., Piepmeier, J. R., Koster, R. D., Martin, N., McDonald, K. C., Moghaddam, M., Moran, S., Reichle, R., Shi, J. C., Spencer, M. W., Thurman, S. W., Tsang, L., and Van Zyl, J. (2010). The soil moisture active passive (smap) mission. *Proceedings of the IEEE*, 98(5):704–716.

[Famiglietti et al., 2008] Famiglietti, J. S., Ryu, D., Berg, A. A., Rodell, M., and Jackson, T. J. (2008). Field observations of soil moisture variability across scales. *Water Resources Research*, 44(1).

[Fattahi and Amelung, 2015] Fattahi, H. and Amelung, F. (2015). Insar bias and uncertainty due to the systematic and stochastic tropospheric delay. *Journal of Geophysical Research: Solid Earth*, 120(12):8758–8773. 2015JB012419.

[Ferretti et al., 1999] Ferretti, A., Prati, C., and Rocca, F. (1999). Permanent scatterers in sar interferometry. In *IEEE 1999 International Geoscience and Remote Sensing Symposium. IGARSS'99 (Cat. No.99CH36293)*, volume 3, pages 1528–1530 vol.3.

[French, 2007] French, H. M. (2007). The periglacial environment. *John Wiley & Sons Ltd,*.

[Gangodagamage et al., 2014] Gangodagamage, C., Rowland, J. C., Hubbard, S. S., Brumby, S. P., Liljedahl, A. K., Wainwright, H., Wilson, C. J., Altmann, G. L., Dafflon, B., Peterson, J., Ulrich, C., Tweedie, C. E., and Wullschleger, S. D. (2014). Extrapolating active layer thickness measurements across arctic polygonal terrain using lidar and ndvi data sets. *Water Resources Research*, 50(8):6339–6357.

[Gatelli et al., 1994] Gatelli, F., Monti Guamieri, A., Parizzi, F., Pasquali, P., Prati, C., and Rocca, F. (1994). The wavenumber shift in sar interferometry. *IEEE Transactions on Geoscience and Remote Sensing*, 32(4):855–865.

[Genet et al., 2013] Genet, H., McGuire, A. D., Barrett, K., Breen, A., Euskirchen, E. S., Johnstone, J. F., Kasischke, E. S., Melvin, A. M., Bennett, A., Mack, M. C., Rupp, T. S., Schuur, A. E. G., Turetsky, M. R., and Yuan, F. (2013). Modeling the effects of fire severity and climate warming on active layer thickness and soil carbon storage of black spruce forests across the landscape in interior alaska. *Environmental Research Letters*, 8(4):045016.

[Goldstein and Zebker, 1987] Goldstein, R. and Zebker, H. (1987). Interferometric radar measurement of ocean surface currents. *Nature 328, 707-709*.

[Goldstein and Werner, 1998] Goldstein, R. M. and Werner, C. L. (1998). Radar interferogram filtering for geophysical applications. *Geophysical Research Letters*, 25(21):4035–4038.

[Goldstein et al., 1988] Goldstein, R. M., Zebker, H. A., and Werner, C. L. (1988). Satellite radar interferometry: Two-dimensional phase unwrapping. *Radio Science*, 23(4):713–720.

[Goodman, 1985] Goodman, J. (1985). *Statistical Optics*. New York: Wiley.

[Grassotti et al., 2003] Grassotti, C., Hoffman, R. N., Vivoni, E. R., and Entekhabi, D. (2003). Multiple-timescale intercomparison of two radar products and rain gauge observations over the arkansas–red river basin. *Weather and Forecasting*, 18(6):1207–1229.

[Grosse et al., 2011] Grosse, G., Harden, J., Turetsky, M., McGuire, A. D., Camill, P., Tarnocai, C., Frolking, S., Schuur, E. A. G., Jorgenson, T., Marchenko, S., Romanovsky, V., Wickland, K. P., French, N., Waldrop, M., Bourgeau-Chavez, L., and Striegl, R. G. (2011). Vulnerability of high-latitude soil organic carbon in north america to disturbance. *Journal of Geophysical Research: Biogeosciences*, 116(G4):n/a–n/a. G00K06.

[Guarnieri and Tebaldini, 2007] Guarnieri, A. M. and Tebaldini, S. (2007). Hybrid cramÉr–rao bounds for crustal displacement field estimators in sar interferometry. *IEEE Signal Processing Letters*, 14(12):1012–1015.

[Hallikainen et al., 1985] Hallikainen, M. T., Ulaby, F. T., Dobson, M. C., El-rayes, M. A., and Wu, L. (1985). Microwave dielectric behavior of wet soil-part 1: Empirical models and experimental observations. *IEEE Transactions on Geoscience and Remote Sensing*, GE-23(1):25–34.

[Hanssen, 2001] Hanssen, R. (2001). *Radar Interferometry: Data Interpretation and Error Analysis*. Kluwer Academic, Dordrecht, Boston.

[Harlan and Nixon, 1978] Harlan, R. and Nixon, J. (1978). Ground thermal regime. *Geotechnical Engineering for Cold Regions*, pages 103–163.

[Hensley et al., 2011] Hensley, S., Michel, T., Van Zyl, J., Muellerschoen, R., Chapman, B., Oveisgharan, S., Haddad, Z. S., Jackson, T., and Mladenova, I. (2011). Effect of soil moisture on

polarimetric-interferometric repeat pass observations by uavsar during 2010 canadian soil moisture campaign. In *2011 IEEE International Geoscience and Remote Sensing Symposium*, pages 1063–1066.

[Hinzman et al., 2005] Hinzman, L. D., Bettez, N. D., Bolton, W. R., Chapin, F. S., Dyurgerov, M. B., Fastie, C. L., Griffith, B., Hollister, R. D., Hope, A., Huntington, H. P., Jensen, A. M., Jia, G. J., Jorgenson, T., Kane, D. L., Klein, D. R., Kofinas, G., Lynch, A. H., Lloyd, A. H., McGuire, A. D., Nelson, F. E., Oechel, W. C., Osterkamp, T. E., Racine, C. H., Romanovsky, V. E., Stone, R. S., Stow, D. A., Sturm, M., Tweedie, C. E., Vourlitis, G. L., Walker, M. D., Walker, D. A., Webber, P. J., Welker, J. M., Winker, K. S., and Yoshikawa, K. (2005). Evidence and implications of recent climate change in northern alaska and other arctic regions. *Climatic Change*, 72(3):251–298.

[Hoen and Zebker, 2000] Hoen, E. W. and Zebker, H. A. (2000). Penetration depths inferred from interferometric volume decorrelation observed over the greenland ice sheet. *IEEE Transactions on Geoscience and Remote Sensing*, 38(6):2571–2583.

[Hooper, 2008] Hooper, A. (2008). A multi-temporal insar method incorporating both persistent scatterer and small baseline approaches. *Geophysical Research Letters*, 35(16).

[Hooper et al., 2004] Hooper, A., Zebker, H., Segall, P., and Kampes, B. (2004). A new method for measuring deformation on volcanoes and other natural terrains using InSAR persistent scatterers. *Geophysical Research Letters*, 31(23):1–5.

[Hugelius et al., 2014] Hugelius, G., Strauss, J., Zubrzycki, S., Harden, J. W., Schuur, E. A. G., Ping, C.-L., Schirrmeister, L., Grosse, G., Michaelson, G. J., Koven, C. D., O'Donnell, J. A., Elberling, B., Mishra, U., Camill, P., Yu, Z., Palmtag, J., and Kuhry, P. (2014). Estimated stocks of circumpolar permafrost carbon with quantified uncertainty ranges and identified data gaps. *Biogeosciences*, 11(23):6573–6593.

[Jafarov et al., 2013] Jafarov, E. E., Romanovsky, V. E., Genet, H., McGuire, A. D., and Marchenko, S. S. (2013). The effects of fire on the thermal stability of permafrost in lowland and upland black spruce forests of interior alaska in a changing climate. *Environmental Research Letters*, 8(3):035030.

[Jennison, 1958] Jennison, R. C. (1958). A phase sensitive interferometer technique for the measurement of the fourier transforms of spatial brightness distributions of small angular extent. *Monthly Notices of the Royal Astronomical Society, Vol. 118, p.276.*

[Jolivet et al., 2014] Jolivet, R., Agram, P. S., Lin, N. Y., Simons, M., Doin, M.-P., Peltzer, G., and Li, Z. (2014). Improving insar geodesy using global atmospheric models. *Journal of Geophysical Research: Solid Earth*, 119(3):2324–2341.

[Jorgenson and Osterkamp, 2005] Jorgenson, M. T. and Osterkamp, T. E. (2005). Response of boreal ecosystems to varying modes of permafrost degradation. *Canadian Journal of Forest Research*, 35(9):2100–2111.

[Jorgenson et al., 2001] Jorgenson, M. T., Racine, C. H., Walters, J. C., and Osterkamp, T. E. (2001). Permafrost degradation and ecological changes associated with a warming climate in central Alaska. *Climatic Change*, 48(4):551–579.

[Jorgenson et al., 2010] Jorgenson, M. T., Romanovsky, V., Harden, J., Shur, Y., O'Donnell, J., Schuur, E. A. G., Kanevskiy, M., and Marchenko, S. (2010). Resilience and vulnerability of permafrost to climate changethis article is one of a selection of papers from the dynamics of change in alaska's boreal forests: Resilience and vulnerability in response to climate warming. *Canadian Journal of Forest Research*, 40(7):1219–1236.

[Jorgenson and Ely, 2001] Jorgenson, T. and Ely, C. (2001). Topography and flooding of coastal ecosystems on the yukon-kuskokwim delta, alaska: Implications for sea-level rise. *Journal of Coastal Research*, 17(1):124–136.

[Joughin et al., 1994] Joughin, I. R., Winebrenner, D. P., and Percival, D. B. (1994). Probability density functions for multilook polarimetric signatures. *IEEE Transactions on Geoscience and Remote Sensing*, 32(3):562–574.

[Just and Bamler, 1994] Just, D. and Bamler, R. (1994). Phase statistics of interferograms with applications to synthetic aperture radar. *Appl. Opt.*, 33(20):4361–4368.

[Konings, 2015] Konings, A. G. (2015). Microwave remote sensing of water in the soil - plant system. *Department of Civil and Environmental Engineering, Massachusetts Institute of Technology, Cambridge, MA, USA.*

[Konings et al., 2016] Konings, A. G., Piles, M., Rötzer, K., McColl, K. A., Chan, S. K., and Entekhabi, D. (2016). Vegetation optical depth and scattering albedo retrieval using time series of dual-polarized l-band radiometer observations. *Remote Sensing of Environment*, 172:178 – 189.

[Lauknes et al., 2010] Lauknes, T., Shanker, A. P., Dehls, J., Zebker, H., Henderson, I., and Larsen, Y. (2010). Detailed rockslide mapping in northern norway with small baseline and persistent scatterer interferometric sar time series methods. *Remote Sensing of Environment*, 114(9):2097 – 2109.

[Lauknes et al., 2011] Lauknes, T. R., Zebker, H. A., and Larsen, Y. (2011). Insar deformation time series using anl_1-norm small-baseline approach. *IEEE Transactions on Geoscience and Remote Sensing*, 49(1):536–546.

[Lawrence et al., 2015] Lawrence, D. M., Koven, C. D., Swenson, S. C., Riley, W. J., and Slater, A. G. (2015). Permafrost thaw and resulting soil moisture changes regulate projected high-latitude CO 2 and CH 4 emissions. *Environmental Research Letters*, 10(9):094011.

[Lee et al., 1994] Lee, J.-S., Miller, A. R., and Hoppel, K. W. (1994). Statistics of phase difference and product magnitude of multi-look processed gaussian signals. *Waves in Random Media*, 4(3):307–319.

[Liu et al., 2014] Liu, L., Jafarov, E. E., Schaefer, K. M., Jones, B. M., Zebker, H. A., Williams, C. A., Rogan, J., and Zhang, T. (2014). Insar detects increase in surface subsidence caused by an arctic tundra fire. *Geophysical Research Letters*, 41(11):3906–3913. 2014GL060533.

[Liu et al., 2012] Liu, L., Schaefer, K., Zhang, T., and Wahr, J. (2012). Estimating 1992–2000 average active layer thickness on the alaskan north slope from remotely sensed surface subsidence. *Journal of Geophysical Research: Earth Surface*, 117(F1).

[Liu et al., 2015] Liu, L., Schaefer, K. M., Chen, A. C., Gusmeroli, A., Zebker, H. A., and Zhang, T. (2015). Remote sensing measurements of thermokarst subsidence using insar. *Journal of Geophysical Research: Earth Surface*, 120(9):1935–1948. 2015JF003599.

[Liu et al., 2010] Liu, L., Zhang, T., and Wahr, J. (2010). InSAR measurements of surface deformation over permafrost on the North Slope of Alaska. *Journal of Geophysical Research: Earth Surface*, 115(3):1–14.

[Lohman and Simons, 2005] Lohman, R. B. and Simons, M. (2005). Some thoughts on the use of insar data to constrain models of surface deformation: Noise structure and data downsampling. *Geochemistry, Geophysics, Geosystems*, 6(1).

[Loranty et al., 2016] Loranty, M. M., Lieberman-Cribbin, W., Berner, L. T., Natali, S. M., Goetz, S. J., Alexander, H. D., and Kholodov, A. L. (2016). Spatial variation in vegetation productivity trends, fire disturbance, and soil carbon across arctic-boreal permafrost ecosystems. *Environmental Research Letters*, 11(9):095008.

[Ludwig et al., 2018] Ludwig, S., Holmes, R. M., Natali, S., Schade, J., and Mann, P. (2018). Yukon-kuskokwim delta fire: Soil and permafrost: bulk density, ph, soil organic matter, ice content, cryostratigraphy, and nutrient profiles, yukon-kuskokwim delta alaska, 2018. *Arctic Data Center.*

[Luo et al., 2000] Luo, X., Askne, J., Smith, G., and Dammert, P. (2000). Coherence characteristics of radar signals from rough soil - abstract. *Journal of Electromagnetic Waves and Applications*, 14(11):1555–1557.

[Mackay, 1995] Mackay, J. R. (1995). Active layer changes (1968 to 1993) following the forest-tundra fire near inuvik, n.w.t., canada. *Arctic and Alpine Research*, 27(4):323–336.

[Massonnet et al., 1993] Massonnet, D., Rossi, M., and Carmona, C. e. a. (1993). The displacement field of the landers earthquake mapped by radar interferometry. *Nature*, 364:138–142.

[McCabe and Wood, 2006] McCabe, M. F. and Wood, E. F. (2006). Scale influences on the remote estimation of evapotranspiration using multiple satellite sensors. *Remote Sensing of Environment*, 105(4):271 – 285.

[McColl et al., 2019] McColl, K. A., He, Q., Lu, H., and Entekhabi, D. (2019). Short-term and long-term surface soil moisture memory time scales are spatially anticorrelated at global scales. *Journal of Hydrometeorology*, 20(6):1165–1182.

[McColl et al., 2014] McColl, K. A., Vogelzang, J., Konings, A. G., Entekhabi, D., Piles, M., and Stoffelen, A. (2014). Extended triple collocation: Estimating errors and correlation coefficients with respect to an unknown target. *Geophysical Research Letters*, 41(17):6229–6236.

[McColl et al., 2017] McColl, K. A., Wang, W., Peng, B., Akbar, R., Short Gianotti, D. J., Lu, H., Pan, M., and Entekhabi, D. (2017). Global characterization of surface soil moisture drydowns. *Geophysical Research Letters*, 44(8):3682–3690.

[Michaelides et al., 2019a] Michaelides, R. J., Schaefer, K., Zebker, H. A., Parsekian, A., Liu, L., Chen, J., Natali, S. M., Ludwig, S., and Schaefer, S. R. (2019a). Inference of the impact of wildfire on permafrost and active layer thickness in a discontinuous permafrost region using the remotely sensed active layer thickness (ReSALT) algorithm. *Environmental Research Letters*, 14(3):035007.

[Michaelides et al., 2019b] Michaelides, R. J., Zebker, H. A., and Zheng, Y. (2019b). An algorithm for estimating and correcting decorrelation phase from insar data using closure phase triplets. *IEEE Transactions on Geoscience and Remote Sensing*, pages 1–8.

[Minsley et al., 2012] Minsley, B. J., Abraham, J. D., Smith, B. D., Cannia, J. C., Voss, C. I., Jorgenson, M. T., Walvoord, M. A., Wylie, B. K., Anderson, L., Ball, L. B., Deszcz-Pan, M., Wellman, T. P., and Ager, T. A. (2012). Airborne electromagnetic imaging of discontinuous permafrost. *Geophysical Research Letters*, 39(2).

[Muller, 1943] Muller, S. W. (1943). Permafrost or permanently frozen ground and related engineering problems. *Special Report, Strategic Engineering Study, Intelligence Branch, Office, Chief of Engineers, no. 62,,*.

[Narvekar et al., 2013] Narvekar, P. S., Entekhabi, D., Kim, S., and Njoku, E. (2013). A robust algorithm for soil moisture retrieval from the soil moisture active passive mission radar observations. In *2013 IEEE International Geoscience and Remote Sensing Symposium - IGARSS*, pages 45–48.

[Natali et al., 2015] Natali, S. M., Schuur, E. A. G., Mauritz, M., Schade, J. D., Celis, G., Crummer, K. G., Johnston, C., Krapek, J., Pegoraro, E., Salmon, V. G., and Webb, E. E. (2015). Permafrost thaw and soil moisture driving co2 and ch4 release from upland tundra. *Journal of Geophysical Research: Biogeosciences*, 120(3):525–537.

[Natali et al., 2014] Natali, S. M., Schuur, E. A. G., Webb, E. E., Pries, C. E. H., and Crummer, K. G. (2014). Permafrost degradation stimulates carbon loss from experimentally warmed tundra. *Ecology*, 95(3):602–608.

[Natali et al., 2019] Natali, S. M., Watts, J., and Rogers, B. (2019). Large loss of co2 in winter observed across the northern permafrost region. *Nature Climate Change*, 9:852–857.

[Nesti et al., 1995] Nesti, G., Tarchi, D., and Rudant, J. . (1995). Decorrelation of backscattered signal due to soil moisture changes. In *1995 International Geoscience and Remote Sensing Symposium, IGARSS '95. Quantitative Remote Sensing for Science and Applications*, volume 3, pages 2026–2028 vol.3.

[Njoku et al., 2003] Njoku, E. G., Jackson, T. J., Lakshmi, V., Chan, T. K., and Nghiem, S. V. (2003). Soil moisture retrieval from amsr-e. *IEEE Transactions on Geoscience and Remote Sensing*, 41(2):215–229.

[Nolan and Fatland, 2003] Nolan, M. and Fatland, D. R. (2003). Penetration depth as a dinsar observable and proxy for soil moisture. *IEEE Transactions on Geoscience and Remote Sensing*, 41(3):532–537.

[Nolan and Fatland, 2003] Nolan, M. and Fatland, D. R. (2003). Penetration depth as a dinsar observable and proxy for soil moisture. *IEEE Transactions on Geoscience and Remote Sensing*, 41(3):532–537.

[Nolan et al., 2003] Nolan, M., Fatland, D. R., and Hinzman, L. (2003). Dinsar measurement of soil moisture. *IEEE Transactions on Geoscience and Remote Sensing*, 41(12):2802–2813.

[Ochsner et al., 2013] Ochsner, T. E., Cosh, M. H., Cuenca, R. H., Dorigo, W. A., Draper, C. S., Hagimoto, Y., Kerr, Y. H., Njoku, E. G., Small, E. E., Zreda, M., and Larson, K. M. (2013). State of the art in large-scale soil moisture monitoring. *Soil Sci. Soc. Am. J.*, 77:1888–1919.

[Oh et al., 1992] Oh, Y., Sarabandi, K., and Ulaby, F. T. (1992). An empirical model and an inversion technique for radar scattering from bare soil surfaces. *IEEE Transactions on Geoscience and Remote Sensing*, 30(2):370–381.

[Osterkamp et al., 2009] Osterkamp, T. E., Jorgenson, M. T., Schuur, E. A. G., Shur, Y. L., Kanevskiy, M. Z., and Vogel, J. G. (2009). Physical and Ecological Changes Associated with

Warming Permafrost and Thermokarst in Interior Alaska. *Permafrost and periglacial processes*, 256(November 2008):235–256.

[Parsekian et al., 2012] Parsekian, A. D., Slater, L., and Giménez, D. (2012). Application of ground-penetrating radar to measure near-saturation soil water content in peat soils. *Water Resources Research*, 48(2):n/a–n/a. W02533.

[Pewe, 1963] Pewe, T. L. (1963). Ice-wedges in alaska-classification, distribution, and climatic significance. *Proceedings Permafrost International Conference*, pages 76–81.

[Pilon et al., 1985] Pilon, J. A., Annan, A. P., and Davis, J. L. (1985). *Monitoring permafrost ground conditions with ground probing radar (G.P.R.)*, pages 71–73.

[Rabus et al., 2010] Rabus, B., Wehn, H., and Nolan, M. (2010). The importance of soil moisture and soil structure for insar phase and backscatter, as determined by fdtd modeling. *IEEE Transactions on Geoscience and Remote Sensing*, 48(5):2421–2429.

[Reeves et al., 2011] Reeves, J. A., Knight, R., Zebker, H. A., Schreüder, W. A., Shanker Agram, P., and Lauknes, T. R. (2011). High quality insar data linked to seasonal change in hydraulic head for an agricultural area in the san luis valley, colorado. *Water Resources Research*, 47(12).

[Rocha et al., 2012] Rocha, A. V., Loranty, M. M., Higuera, P. E., Mack, M. C., Hu, F. S., Jones, B. M., Breen, A. L., Rastetter, E. B., Goetz, S. J., and Shaver, G. R. (2012). The footprint of alaskan tundra fires during the past half-century: implications for surface properties and radiative forcing. *Environmental Research Letters*, 7(4):044039.

[Rodriguez and Martin, 1992] Rodriguez, E. and Martin, J. M. (1992). Theory and design of interferometric synthetic aperture radars. *IEE Proceedings F - Radar and Signal Processing*, 139(2):147–159.

[Rosen et al., 2000] Rosen, P. A., Hensley, S., Joughin, I. R., Li, F. K., Madsen, S. N., Member, S., Rodríguez, E., and Goldstein, R. M. (2000). Synthetic Aperture Radar Interferometry. *Proceedings of the IEEE*, 88(3).

[Samiei-Esfahany et al., 2016] Samiei-Esfahany, S., Martins, J. E., van Leijen, F., and Hanssen, R. F. (2016). Phase estimation for distributed scatterers in insar stacks using integer least squares estimation. *IEEE Transactions on Geoscience and Remote Sensing*, 54(10):5671–5687.

[Schaefer et al., 2015] Schaefer, K., Liu, L., Parsekian, A., Jafarov, E., Chen, A., Zhang, T., Gusmeroli, A., Panda, S., Zebker, H. A., and Schaefer, T. (2015). Remotely Sensed Active Layer Thickness (ReSALT) at Barrow, Alaska Using Interferometric Synthetic Aperture Radar. *Remote Sens*, 7:3735–3759.

[Schaefer et al., 2009] Schaefer, K., Zhang, T., Slater, A. G., Lu, L., Etringer, A., and Baker, I. (2009). Improving simulated soil temperatures and soil freeze/thaw at high-latitude regions in the simple biosphere/carnegie-ames-stanford approach model. *Journal of Geophysical Research: Earth Surface*, 114(F2).

[Schmidt and Burgmann, 2003] Schmidt, D. A. and Burgmann, R. (2003). Time-dependent land uplift and subsidence in the santa clara valley, california, from a large interferometric synthetic aperture radar data set. *Journal of Geophysical Research: Solid Earth*, 108(B9).

[Schmugge and Jackson, 1992] Schmugge, T. J. and Jackson, T. J. (1992). A dielectric model of the vegetation effects on the microwave emission from soils. *IEEE Transactions on Geoscience and Remote Sensing*, 30(4):757–760.

[Schneider and Oppelt, 1998] Schneider, K. and Oppelt, N. (1998). The determination of mesoscale soil moisture patterns with ers data. In *IGARSS '98. Sensing and Managing the Environment. 1998 IEEE International Geoscience and Remote Sensing. Symposium Proceedings. (Cat. No.98CH36174)*, volume 4, pages 1831–1833 vol.4.

[Schuur et al., 2008] Schuur, E. A. G., Bockheim, J., Canadell, J., Euskirchen, E., Field, C., Goryachkin, S., Hagemann, S., Kuhry, P., Lafleur, P., Lee, H., Mazhitova, G., Nelson, F., Rinke, A., Romanovsky, V., Shiklomanov, N., Tarnocai, C., Venevsky, S., Vogel, J., and Zimov, S. (2008). Vulnerability of permafrost carbon to climate change: Implications for the global carbon cycle. *BioScience*, 58(September):701–714.

[Seymour and Cumming, 1994] Seymour, M. S. and Cumming, I. G. (1994). Maximum likelihood estimation for sar interferometry. In *Proceedings of IGARSS '94 - 1994 IEEE International Geoscience and Remote Sensing Symposium*, volume 4, pages 2272–2275 vol.4.

[Shanker et al., 2011] Shanker, P., Casu, F., Zebker, H. A., and Lanari, R. (2011). Comparison of persistent scatterers and small baseline time-series insar results: A case study of the san francisco bay area. *IEEE Geoscience and Remote Sensing Letters*, 8(4):592–596.

[Shanker and Zebker, 2007] Shanker, P. and Zebker, H. (2007). Persistent scatterer selection using maximum likelihood estimation. *Geophysical Research Letters*, 34(22).

[Shepherd, 2016] Shepherd, T. G. (2016). Effects of a warming arctic. *Science*, 353(6303):989–990.

[Shi et al., 1997] Shi, J., Wang, J., Hsu, A. Y., O'Neill, P. E., and Engman, E. T. (1997). Estimation of bare surface soil moisture and surface roughness parameter using l-band sar image data. *IEEE Transactions on Geoscience and Remote Sensing*, 35(5):1254–1266.

[Shur and Jorgenson, 2007] Shur, Y. L. and Jorgenson, M. T. (2007). Patterns of permafrost formation and degradation in relation to climate and ecosystems. *Permafrost and Periglacial Processes*, 18(1):7–19.

[Stiles and Ulaby, 1981] Stiles, W. and Ulaby, F. (1981). Dielectric properties of snow. *EARTH RESOURCES AND REMOTE SENSING*.

[Swanson, 1981] Swanson, F. (1981). Fire and geomorphic processes. *in: Mooney, H.A., Bonnicksen, T.M., Christiansen, N.L., Lotan, J.E., Reiners, W.A. (Eds.), Fire Regime and Ecosystem Properties, United States Department of Agriculture, Forest Service, General Technical Report WO vol. 26. United States Government Planning Office, Washington, DC*, pages 401–421.

[Tabatabaeenejad et al., 2015] Tabatabaeenejad, A., Member, S., and Burgin, M. (2015). P-Band Radar Retrieval of Subsurface Soil Moisture Profile as a Second-Order Polynomial : First AirMOSS Results. *IEEE Transactions on Geoscience and Remote Sensing*, 53(2):645–658.

[Taylor and Peltzer, 2006] Taylor, M. and Peltzer, G. (2006). Current slip rates on conjugate strike-slip faults in central tibet using synthetic aperture radar interferometry. *Journal of Geophysical Research: Solid Earth*, 111(B12).

[*Decadal Survey*, 2018] *Decadal Survey* (2018). Thriving on our changing planet: A decadal strategy for earth observation from space. *National Academies of Sciences, Engineering, and Medicine. Washington, DC: The National Academies Press*.

[*National Research Council*, 2004] *National Research Council* (2004). *Groundwater Fluxes Across Interfaces*. The National Academies Press, Washington, DC.

[Tomasanis, 1990] Tomasanis, D. (1990). Effective dielectric constants of foliage media.

[Tough et al., 1995] Tough, J. A., Blacknell, D., and Quegan, S. (1995). A statistical description of polarimetric and interferometric synthetic aperture radar data. *Proceedings of the Royal Society of London. Series A: Mathematical and Physical Sciences*, 449(1937):567–589.

[Touzi et al., 1999] Touzi, R., Lopes, A., Bruniquel, J., and Vachon, P. W. (1999). Coherence estimation for sar imagery. *IEEE Transactions on Geoscience and Remote Sensing*, 37(1):135–149.

[Treuhaft et al., 1996] Treuhaft, R. N., Madsen, S. N., Moghaddam, M., and van Zyl, J. J. (1996). Vegetation characteristics and underlying topography from interferometric radar. *Radio Science*, 31(6):1449–1485.

[Treuhaft and Siqueira, 2000] Treuhaft, R. N. and Siqueira, P. R. (2000). Vertical structure of vegetated land surfaces from interferometric and polarimetric radar. *Radio Science*, 35(1):141–177.

[Turetsky et al., 2019a] Turetsky, M. R., Abbott, B. W., Jones, M. C., Anthony, K. W., Olefeldt, D., Schuur, E. A. G., Grosse, G., Kuhry, P., Hugelius, G., Koven, C., Lawrence, D. M., Gibson,

C., Sannel, A. B. K., and McGuire, A. D. (2019a). Carbon release through abrupt permafrost thaw. *Nature Geoscience*, 13:138–143.

[Turetsky et al., 2019b] Turetsky, M. R., Abbott, B. W., Jones, M. C., Anthony, K. W., Olefeldt, D., Schuur, E. A. G., Koven, C., D., M. A., Grosse, G., Kuhry, P., Hugelius, G., Lawrence, D. M., Gibson, C., and Sannel, A. B. K. (2019b). Permafrost collapse is accelerating carbon release. *Nature*, 569:32–35.

[Turetsky et al., 2007] Turetsky, M. R., Wieder, R. K., Vitt, D. H., Evans, R. J., and Scott, K. D. (2007). The disappearance of relict permafrost in boreal north america: Effects on peatland carbon storage and fluxes. *Global Change Biology*, 13(9):1922–1934.

[Ulaby, 1985] Ulaby, F. (1985). Microwave dielectric and propagation properties of vegetation canopies. *EARTH RESOURCES AND REMOTE SENSING*.

[Ulaby and Long, 2014] Ulaby, F. T. and Long, D. G. (2014). *Microwave radar and radiometric remote sensing*. ARTECH HOUSE.

[Van Zyl and Kim, 2011] Van Zyl, J. and Kim, Y. (2011). *Applications: Measurement of Surface Soil Moisture*, chapter 5, pages 182–261. John Wiley & Sons, Ltd.

[Viereck and Schandelmeier, 1980] Viereck, L. A. and Schandelmeier, L. A. (1980). Effects of fire in alaska and adjacent canada: a literature review. *U.S. Departement of the Interior*.

[Waechter et al., 2004] Waechter, M., Riess, F., Schimmel, T., Wendt, U., and Peinke, J. (2004). Stochastic analysis of different rough surfaces. *The European Physical Journal B - Condensed Matter and Complex Systems*, 41(2):259–277.

[Walvoord and Kurylyk, 2016] Walvoord, M. A. and Kurylyk, B. L. (2016). Hydrologic Impacts of Thawing Permafrost—A Review. *Vadose Zone Journal*, 15(6). vzj2016.01.0010.

[Widhalm et al., 2017] Widhalm, B., Bartsch, A., Leibman, M., and Khomutov, A. (2017). Active-layer thickness estimation from x-band sar backscatter intensity. *The Cryosphere*, 11(1):483–496.

[Woo, 1990] Woo, M. (1990). Consequences of climatic change for hydrology in permafrost zones. *Journal of Cold Regions Engineering*, 4(1):15–20.

[Yufeng et al., 2018] Yufeng, H., Lin, L., Larson, K. M., Schaefer, K. M., Zhang, J., and Yao, Y. (2018). Gps interferometric reflectometry reveals cyclic elevation changes in thaw and freezing seasons in a permafrost area (barrow, alaska). *Geophysical Research Letters*, 45(11):5581–5589.

[Zebker, 2020] Zebker, H. (2020). Private Communication.

[Zebker et al., 2010] Zebker, H. A., Hensley, S., Shanker, P., and Wortham, C. (2010). Geodetically accurate insar data processor. *IEEE Transactions on Geoscience and Remote Sensing*, 48(12):4309–4321.

[Zebker and Villasenor, 1992] Zebker, H. A. and Villasenor, J. (1992). Decorrelation in interferometric radar echoes. *IEEE Transactions on Geoscience and Remote Sensing*, 30(5):950–959.

[Zhang et al., 2018] Zhang, Y., Fattahi, H., and Amelung, F. (2018). Two unwrapping error correction methods based on bridging and phase closure for the interferogram stack. *AGU Fall Meeting 2018*.

[Zwieback et al., 2015a] Zwieback, S., Hensley, S., and Hajnsek, I. (2015a). Assessment of soil moisture effects on l-band radar interferometry. *Remote Sensing of Environment*, 164:77 – 89.

[Zwieback et al., 2015b] Zwieback, S., Hensley, S., and Hajnsek, I. (2015b). A polarimetric first-order model of soil moisture effects on the dinsar coherence. *Remote Sensing*, 7(6):7571–7596.

[Zwieback et al., 2017] Zwieback, S., Hensley, S., and Hajnsek, I. (2017). Soil moisture estimation using differential radar interferometry: Toward separating soil moisture and displacements. *IEEE Transactions on Geoscience and Remote Sensing*, 55(9):5069–5083.

[Zwieback et al., 2016] Zwieback, S., Liu, X., Antonova, S., Heim, B., Bartsch, A., Boike, J., and Hajnsek, I. (2016). A statistical test of phase closure to detect influences on dinsar deformation estimates besides displacements and decorrelation noise: Two case studies in high-latitude regions. *IEEE Transactions on Geoscience and Remote Sensing*, 54(9):5588–5601.